Title

Optimization and Validation of Ferumoxytol-Enhanced Myocardial T1 Reactivity and Myocardial Blood Volume Mapping for Detection of Myocardial Ischemia

Permalink

https://escholarship.org/uc/item/3w33w79c

Author

Colbert, Caroline Mary

Publication Date

2022

Peer reviewed|Thesis/dissertation

UNIVERSITY OF CALIFORNIA

Los Angeles

Optimization and Validation of Ferumoxytol-Enhanced Myocardial T1 Reactivity and Myocardial Blood Volume Mapping for Detection of Myocardial Ischemia

A dissertation submitted in partial satisfaction of the
requirements for the degree Doctor of Philosophy
in Physics & Biology in Medicine
by

Caroline Mary Colbert

2022

ABSTRACT OF THE DISSERTATION

Optimization and Validation of Ferumoxytol-Enhanced Myocardial T1 Reactivity and Myocardial Blood Volume Mapping for Detection of Myocardial Ischemia

by

Caroline Mary Colbert
Doctor of Philosophy in Physics and Biology in Medicine
University of California, Los Angeles, 2022
Professor Kim-Lien Nguyen, Co-Chair
Professor Holden H. Wu, Co-Chair

Cardiovascular disease remains the global leading cause of death. Noninvasive imaging techniques to detect and quantify myocardial ischemia continue to have wide-ranging impact in clinical cardiovascular care. This body of research aims to develop several novel noninvasive quantitative cardiac magnetic resonance imaging (MRI) techniques for the detection of ischemic heart disease. 3D printed implants were designed, manufactured, and percutaneously deployed in the left anterior descending (LAD) artery of 13 swine to investigate the feasibility and efficacy of the implants to cause hypoperfusion and ischemia on MRI. This novel animal model offers a success rate comparable to that of highly invasive methods, allowing for more rapid and cost-effective translational imaging studies. In a cohort of these swine models, this work found that ferumoxytol improves the diagnostic performance of T1 reactivity as a measure of myocardial ischemia. Next, FE-MRI was used to capture a hemodynamic response to myocardial hypoperfusion at rest. A two-compartment water exchange model was derived and tested in order to quantify fractional myocardial blood volume (fMBV) before developing an integrated image registration and compartmental modelling platform. This method was used to demonstrate the feasibility of a two-compartment model for estimation of fMBV using steady-state Modified Look-Locker Inversion recovery (MOLLI) T1 mapping over multiple ferumoxytol doses. The technical developments to this image processing pipeline advance the current state of pixelwise fMBV mapping toward a more integrated in-line approach. This work ultimately demonstrates that this fMBV mapping approach can be used to distinguish between ischemic and remote myocardium in a broader study in 19 ischemic swine models. Finally, a further investigation of the in-vitro and in-vivo MRI properties of three comparable iron-based contrast agents may help to expand the adoption of this unique class of contrast agents. In addition to these contributions to the development of two novel imaging biomarkers of heart disease, this body of research enables a broad range of new research in quantitative cardiovascular MRI.

The dissertation of Caroline Mary Colbert is approved.

Rohan Dharmakumar

Peng Hu

John Paul Finn

Kyung-Hyun Sung

Holden H. Wu, Committee Co-Chair

Kim-Lien Nguyen, Committee Co-Chair

University of California, Los Angeles

2022

TABLE OF CONTENTS

LIST OF ABBREVIATIONS

2D/3D - two/three dimensional

ANOVA - Analysis Of Variance

ANCOVA - Analysis Of Covariance

AUC - Area Under the Curve (receiver operating characteristic curve)

bSSFP - Balanced Steady-State Free Precession

CoV - Coefficient of Variation

CNR - Contrast to Noise Ratio

ECG - Electrocardiogram

EPI - Echo-Planar Imaging

FE - Ferumoxytol-Enhanced

FFR - Fractional Flow Reserve

FLASH - Fast Low-Angle Shot Imaging

fMBV - Fractional Myocardial Blood Volume

FOV - Field Of View

GBCA - Gadolinium-Based Contrast Agent

HASTE - Half-Fourier-Acquired Single-shot Turbo-spin Echo

IHD - Ischemic Heart Disease

InSiL - Instantaneous Signal Loss simulation algorithm

IQR - Inter-Quartile Range

LAD - Left Anterior Descending coronary artery

LCX - Left Circumflex coronary artery

LV - Left Ventricle or Left Ventricular

mm - millimeter

mM - millimolar

MOLLI - Modified Look-Locker Inversion Recovery

MRI - Magnetic Resonance Imaging

ms - millisecond

MUSIC - Multiphase Steady-state Imaging with Contrast

PCA - Principal Component Analysis

PS - Permeability-Surface area product

RCA - Right Coronary Artery

ROI - Region Of Interest

RWMA - Regional Wall Motion Abnormality

s - second

SD - Standard Deviation

SNR - Signal to Noise Ratio

SI - Signal Intensity

T - Tesla

T1w - T1-weighted

T2w - T2-weighted

TE - Echo Time

TI - Inversion Time

TR - Repetition Time

TS - Saturation Time

TSE - Turbo Spin Echo

TTC - Triphenyltetrazolium chloride

USPIO – Ultrasmall Superparamagnetic Iron Oxide

VIBE - Volumetric Interpolated Breath-Hold Exam

LIST OF FIGURES

LIST OF TABLES

ACKNOWLEDGEMENTS

I would like to express my sincere gratitude to my advisor Dr. Kim-Lien Nguyen for her thoughtful and caring mentorship throughout my time at UCLA. Dr. Nguyen's patient and persistent efforts to guide, teach, and train me have been instrumental to my growth as a scientist and a person. I also warmly thank Peng Hu for his co-mentorship throughout the term of my studies, and Holden Wu for his generous contribution to my mentorship in my final year. I thank all my committee members, Kim-Lien Nguyen, Holden Wu, J. Paul Finn, Kyung-Hyun Sung, Peng Hu and Rohan Dharmakumar, for their thoughtful critique of my work throughout my progress toward my final defense. Their insights have strengthened my scientific work and informed my growth as a critical thinker.

Many collaborators have played instrumental roles in my research work. Among these are Aleksandra Radjenovic, Grace Kim, Dan Ruan, Jesse Currier, John Hollowed, Sandra Duarte-Vogel, Gregory Fishbein, Olujimi Ajijola, Dylan Nguyen, and Magnus Dahlbom. For their contributions to my clinical and translational research, I thank Anthony Smithson, Arvin Roque-Verdoflor, Tyrone Wong, Shawn McGill, and Mary Susselman, in addition to Glen Nyborg, Sergio Godinez, Kelly O'Connor, Leo Rubia, and Merkebu Gebremariam. In addition to my mentors and collaborators, I would like to thank my friends and colleagues in the UCLA Magnetic Resonance Research Labs including Summer (Yu), Chang, Jiaxin, Fadil, Vahid, Mark, Tyler, Nyasha, Xinran, Ran, Sevgi, Zhengyang, Harry, and Mimi. My broader PBM community has been a great source of joy for me during my time at UCLA. I thank Dr. Mike McNitt-Gray, Reth Im, and Alondra Correa Bautista for their commitment to PBM's students and faculty.

Finally, my family and friends have been instrumental to my success in graduate school, providing practical and moral support during the term of my PhD. I thank my brothers Matthew

and Daniel, my parents Matt and Rose, and my fiancé Cosmos for their support and interest in my graduate research.

Chapter 3 is a version of: Colbert CM, Shao J, Hollowed JJ, Currier JW, Ajijola OA, Fishbein GA, Duarte-Vogel SM, Dharmakumar R, Hu P, Nguyen KL. 3D-Printed Coronary Implants Are Effective for Percutaneous Creation of Swine Models with Focal Coronary Stenosis. J Cardiovasc Transl Res. 2020;13(6):1033-1043. https://doi.org/10.1007/s12265-020-10018-3 © Springer Science+Business Media, LLC, part of Springer Nature 2020, distributed under the terms of the Creative Commons Attribution License (CC BY-NC 4.0). This work is reproduced with minor changes.

Chapter 4 is a version of: Colbert CM, Le AH, Shao J, Currier JW, Ajijola OA, Hu P, Nguyen KL. Ferumoxytol-Enhanced Magnetic Resonance T1 Reactivity For Depiction Of Myocardial Hypoperfusion. NMR Biomed. 2021;34(7). https://doi.org/10.1002/nbm.4518 © 2021 John Wiley & Sons, Ltd. This work is reproduced with minor changes in compliance with the terms of the Contributors' Copyright Transfer Agreement.

Chapter 5 is a version of: Colbert CM, Thomas MA, Yan R, Radjenovic A, Finn JP, Hu P, Nguyen KL. Estimation Of Fractional Myocardial Blood Volume And Water Exchange Using Ferumoxytol-Enhanced Magnetic Resonance Imaging. J Magn Reson Imaging. 2021;53(6):1699-1709. https://doi.org/10.1002/jmri.27494 © 2020 International Society for Magnetic Resonance in Medicine. This work is reproduced with minor changes in compliance with the terms of the Contributors' Copyright Transfer Agreement.

Chapter 6 is a version of: Colbert CM, Nguyen D, Hu P, Nguyen KL. Implementation Of An Integrated Nonrigid Magnetic Resonance Image Registration And Fractional Myocardial Blood Volume Mapping Framework. *J Cardiovasc Magn Reson.* 2022. In preparation.

Chapter 7 is a version of: Colbert CM, Hollowed JJ, Nguyen D, Hu P, Nguyen KL. Estimation Of Ischemic Burden By Magnetic Resonance Image-Derived Fractional Myocardial Blood Volume. *J Magn Reson Imaging.* 2021. Under review.

Chapter 8 is a version of: Colbert CM, Ming Z, Pogosyan A, Hu P, Finn JP, Nguyen KL. Magnetic Resonance Relaxometry And In-Vivo Imaging Performance Of Molday ION: A Novel Ultrasmall Superparamagnetic Iron-Based Contrast Agent. *Invest Radiol*. 2021. Under review.

VITA

Education:

- Ph.D. candidate, Physics and Biology in Medicine, University of California, Los Angeles, CA, 2017 – 2022
- BS, Nuclear Science and Engineering, Massachusetts Institute of Technology, Cambridge, MA, 2013 – 2017

Awards:

- UCLA PBM Graduate Program Moses A. Greenfield Award Nominee, 2021
- ISMRM W.S. Moore Young Investigator Award Finalist, 2020
- UCLA Graduate Dean's Scholar Award, 2017

First Author Publications and Manuscripts:

1. **Colbert CM,** Shao J, Hollowed JJ, Currier JW, Ajijola OA, Fishbein GA, Duarte-Vogel SM, Dharmakumar R, Hu P, Nguyen KL. 3D-Printed Coronary Implants Are Effective for Percutaneous Creation of Swine Models with Focal Coronary Stenosis. J Cardiovasc Transl Res. 2020;13(6):1033-1043.
2. **Colbert CM,** Le AH, Shao J, Currier JW, Ajijola OA, Hu P, Nguyen KL. Ferumoxytol-Enhanced Magnetic Resonance T1 Reactivity For Depiction Of Myocardial Hypoperfusion. NMR Biomed. 2021;34(7).
3. **Colbert CM**, Thomas MA, Yan R, Radjenovic A, Finn JP, Hu P, Nguyen KL. Estimation Of Fractional Myocardial Blood Volume And Water Exchange Using Ferumoxytol-Enhanced Magnetic Resonance Imaging. J Magn Reson Imaging. 2021;53(6):1699-1709. ISMRM W.S. Moore Award Finalist.

4. **Colbert CM**, Hollowed JJ, Nguyen D, Hu P, Nguyen KL. Estimation Of Ischemic Burden By Magnetic Resonance Image-Derived Fractional Myocardial Blood Volume. *J Magn Reson Imaging.* 2021. Under review.
5. **Colbert CM**, Ming Z, Pogosyan A, Hu P, Finn JP, Nguyen KL. Comparison of Three Ultrasmall, Superparamagnetic Iron Oxide Nanoparticles for Magnetic Resonance Imaging at 3.0. *JACC Cardiovasc Imaging*. 2022. Under review.
6. **Colbert CM**, Nguyen D, Ruan D, Nguyen KL. Implementation Of An Integrated Nonrigid Magnetic Resonance Image Registration And Fractional Myocardial Blood Volume Mapping Framework. 2022. In preparation.

Co-Author Peer-Reviewed Publications:

1. Young MR, Craft DL, **Colbert CM**, Remillard K, Vanbenthuysen L, Wang Y. Volumetric-Modulated Arc Therapy Using Multicriteria Optimization For Body And Extremity Sarcoma. J Appl Clin Med Phys. 2016;17(6):283-291.
2. Hollowed JJ, **Colbert CM**, Currier JW, Nguyen K-L. Novel Percutaneous Approach for Deployment of 3D Printed Coronary Stenosis Implants in Swine Models of Ischemic Heart Disease. J Vis Exp. Published online 2020: e60729.
3. Ming Z, **Colbert CM**, Ruan D, Wu HH, Christodoulou AG, Finn JP, Hu P, Nguyen K-L. Cluster-Based 2D Cardiac Cine Imaging. In preparation

Chapter 1 Introduction

1.1 Thesis motivation

Cardiovascular disease is the leading cause of death worldwide.[1] Although modern medical imaging techniques have facilitated advances in the diagnosis and treatment of ischemic heart disease (IHD), the development of noninvasive imaging techniques to detect and quantify tissue perfusion remains an area of intense research interest. Highly sensitive noninvasive imaging techniques have the potential to benefit patients by promoting early detection and treatment of cardiovascular disease with medical management and lifestyle changes while many effects of cardiovascular disease remain reversible. Likewise, highly specific diagnostic imaging biomarkers employed at the initial screening stage have the potential to divert patients from unnecessary invasive catheterization, improving patient quality of life. The availability of superior noninvasive imaging techniques to detect and quantify myocardial ischemia has the potential to have wide-ranging impact in clinical cardiovascular care.

Relative to other cardiovascular diagnostic imaging techniques, cardiac magnetic resonance (CMR) imaging provides superior soft tissue contrast with no ionizing radiation dose. MR signal can be manipulated to improve the visualization of cardiac anatomy, morphology, and function, with and without using MRI contrast agents. Most contrast-enhanced CMR techniques rely on gadolinium-based contrast agents (GBCAs). Often described as an extravascular contrast agent, GBCAs' extravasation into the myocardial extravascular space is exploited to quantify myocardial tissue perfusion and visualize regions of scar.[2] Conversely, intravascular contrast agents, which remain in the blood pool and do not extravasate into the extravascular space except in the setting of vessel wall perforation, have unique CMR applications of their own. While the clinical implications of gadolinium retention in biologic tissues are unclear, concerns about gadolinium deposition in tissues of patients with and without impaired renal function have contributed to rising interest in gadolinium-free methods.[3–5]

Ultrasmall superparamagnetic iron oxide (USPIO) nanoparticles are a class of MRI contrast agents that represent a potential alternative to GBCAs for certain imaging applications. Ferumoxytol is one such USPIO agent. The ferumoxytol molecule has a mean diameter of 30 nm,[6] an intravascular half-life of 10-14 hours, and an R1 relaxivity of 9.5 s^{-1} mM^{-1} at 3.0T in human plasma at 37°C.[7,8] Ferumoxytol has shown strong biosafety profile in vitro and in vivo.[9] Ferumoxytol is approved for the intravenous treatment of iron deficiency anemia, and is the only intravascular agent clinically available for off-label use as an MRI contrast agent.[10–15] Its unique biodistribution makes it well-suited to CMR techniques that attempt to directly image the major vessels, as well as the myocardial vascular compartment, including magnetic resonance angiography (MRA) and tissue compartmental modelling applications. When combined with an MRI stress testing approach, ferumoxytol has shown early potential to sensitize myocardial MRI signal to myocardial ischemia.[16] Additionally, its long intravascular half-life and high r1/r2 ratio[8] make ferumoxytol ideal for novel physiologic modelling approaches. Ferumoxytol is central to ongoing research to measure and map intramyocardial blood volume in the heart muscle, a technique that has the potential to both identify myocardial ischemia and quantify its extent within the myocardium as well as its severity.

Although the development of reliable CMR imaging biomarkers of ischemic heart disease has the potential to reshape clinical cardiovascular care for patients with IHD, several significant challenges continue to impair broad adoption of these techniques. Animal models of myocardial ischemia are time- and resource-intensive to create, presenting a significant barrier to preclinical imaging research.[17,18] Myocardial ischemia can vary in intensity from very mild to very severe, necessitating the development of imaging biomarkers that are sufficiently sensitive and specific to outperform other diagnostic imaging techniques. Stress testing[19],while a powerful diagnostic technique, results in significant patient discomfort and occasional serious side effects[20], and development of diagnostic imaging methods for ischemia at rest is desirable. Fractional myocardial blood volume (fMBV) estimated using steady state MRI acquisitions over multiple intravascular contrast doses has the potential to capture a hemodynamic response to myocardial hypoperfusion at rest, without reliance on gadolinium. However, these acquisitions can entail long scan times, limiting the feasibility of this technique in the clinical setting. Image registration and technical challenges related to the combination of multiple parametric mapping approaches make compartmental modelling a highly specialized technique. Finally, the limited availability and high cost of intravascular agents severely limits the adoption of USPIO-based imaging techniques, a strong motivating factor for the development of viable alternative contrast agents. The technical developments and investigations detailed in this thesis undertake to address some aspect of each of these challenges and reflect a systematic approach to improve rigor and reproducibility in imaging biomarker development, helping to improve the availability of high-quality, patient-specific, noninvasive CMR imaging for patients with IHD.

1.2 Specific aims

The overall goal of this research work is to contribute to the development of noninvasive imaging techniques to detect and quantify myocardial ischemia in order to improve the reliability of diagnostic cardiac MRI and make a positive impact on patients' clinical cardiovascular care. We aim to help improve the availability of high-quality, patient-specific, noninvasive CMR imaging for patients with IHD. The research work presented here can be divided into three aims. These are: Aim 1 - develop a reliable and efficient preclinical swine model of inducible ischemia, Aim 2 – provide early validation of two complementary noninvasive imaging biomarkers of ischemia, Aim 3 – perform a further proof-of-concept of fMBV as an imaging biomarker of ischemia, and its consistency with novel contrast agents.

1.3 Organization of the thesis

Chapter 2 will introduce technical background concepts that bear direct relevance to the subsequent chapters. The remaining thesis chapters (Figure 1.1) will address the investigations and technical developments made to develop noninvasive imaging biomarkers of IHD. Figure 1.1 describes the structure of the thesis body, outlining how preliminary developments in chapters 3 through 5 facilitate further technical developments reported in chapters 6 through 8.

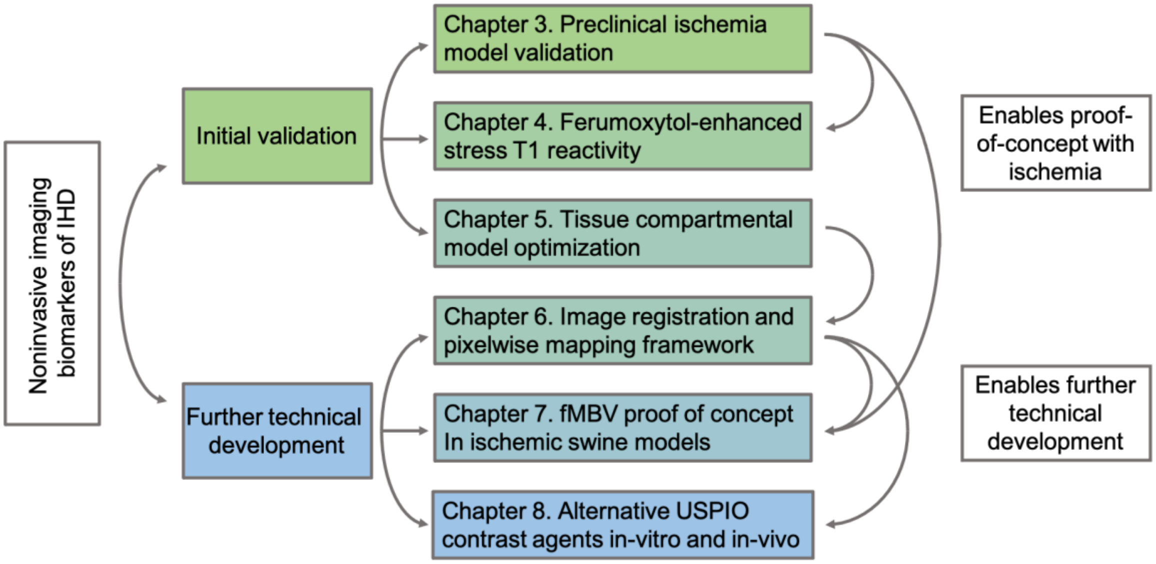

Figure 1.1. Outline of the major technical developments described in this work.

To enhance rigor and reproducibility in biomarker development and reduce the number of confounders that sometimes contribute to variability in imaging biomarkers, preclinical validation is typically necessary prior to its translation into a study in humans. However, reliable closed-chest methods for creating large animal models of acute myocardial hypoperfusion are limited.[18] Such minimally invasive techniques are desirable, as they minimize the requirement of time, specialized equipment and facilities required. In chapter 3, the feasibility and efficacy of using MR-compatible 3D printed coronary implants for establishing swine models of myocardial hypoperfusion is demonstrated. Intracoronary implants were designed, manufactured, and percutaneously deployed in 13 swine to selectively create focal coronary stenosis. To test the efficacy of the implants to cause hypoperfusion or ischemia in the perfused territory, invasive coronary pressure measurements were taken using pressure catheters, and regional wall motion, myocardial perfusion, and infarction were evaluated using MRI. In chapter 4, the diagnostic performance of ferumoxytol-enhanced (FE) myocardial T1 reactivity are assessed in these novel swine models of myocardial hypoperfusion. Myocardial T1 reactivity, defined as the relative change in T1 between rest and vasodilator-induced stress, has been proposed as an MRI biomarker of tissue perfusion.[16] This work hypothesizes that the superparamagnetic iron-oxide nanoparticle ferumoxytol increases the magnitude of T1 stress reactivity, improving the sensitivity and specificity of T1 reactivity as an imaging biomarker of tissue perfusion. Native and ferumoxytol-enhanced adenosine stress testing was performed using two MRI T1 mapping sequences on a clinical 3.0 T magnet and compared native (non-contrast) and ferumoxytol-enhanced T1 reactivity in ischemic and remote myocardial territories.

MRI stress testing can be used to directly measure myocardial perfusion reserve. However, the development of imaging biomarkers of ischemia that do not rely on pharmacologic stress has the potential to dramatically improve patient quality of life. Fractional myocardial blood volume (fMBV) estimated using ferumoxytol-enhanced MRI (FE-MRI) has the potential to capture a hemodynamic response to myocardial hypoperfusion at rest, without reliance on gadolinium. Chapter 5 describes the development of a two-compartment water exchange model for fMBV quantification. An optimal sampling scheme is also investigated, and preliminary evidence that fMBV differentiates between hypoperfused and perfused myocardium is shown in a swine model with coronary stenosis. This work is further developed in chapter 6, which describes the development of an integrated image registration and compartmental modelling platform to generate pixelwise maps of fMBV in ischemic swine models and healthy human volunteers. This work evaluates a principal component analysis (PCA)-based image registration method and investigates the physiologic boundary conditions which minimize image noise in fMBV maps. These studies both culminate in the study described in Chapter 7. Model-fitted pixelwise fMBV maps are used to measure myocardial tissue hypoperfusion at rest in 19 ischemic swine models with a 3D-printed coronary implant in the left anterior descending (LAD) artery. This work tests the ability of model-fitted fMBV and water exchange to distinguish between ischemic and remote myocardial regions in the same subject and examines sex-specific differences in ischemic and remote fMBV between male and female swine subjects. Receiver operating characteristic (ROC) curves are also reported to further evaluate the diagnostic performance of fMBV as a marker for myocardial hypoperfusion.

Finally, despite the unique off-label MRI applications of ferumoxytol (Feraheme, Covis pharma), its adoption is limited by availability and cost. Recently, generic ferumoxytol was approved in the U.S. for human therapeutic use while Molday ION (BioPal), an alternative USPIO with similar properties, is available for pre-clinical use. In chapter 8, the in-vitro and in-vivo MRI properties of Feraheme, generic ferumoxytol, and Molday ION are compared. This study quantifies the r1 and r2 relaxivities of Feraheme, generic ferumoxytol, and Molday ION in MRI phantoms containing saline, plasma, and blood. It also compares in-vivo contrast effects on T1- weighted 4D-MUSIC, 3D-VIBE, and 2D-MOLLI-T1 images, as well as T2-weighted 2D-HASTE images in sixteen swine. Chapter 8 concludes the dissertation with a summary of these technical developments and provides a brief outlook on future research.

1.4 A note on experimental animal care and use

The swine studies described in this work were all performed with the approval of our Institutional Animal Care and Use Committee, the UCLA Chancellor's Animal Research Committee (ARC). The experiments were conducted in accordance with the recommendations of the Guide for the Care and use of Laboratory Animals, the Animal Welfare Act, the National Institutes of Health, and the American Heart Association on Research Animal Use (adopted November 11, 1984). Animals were housed on site for two weeks prior to experiments with no more than one pen mate in a dedicated vivarium staffed by certified veterinary technicians.

Prior to all procedures, swine were sedated with intramuscular ketamine (10mg/kg) and midazolam (1mg/kg) and intubated. Inhaled 1-2% isoflurane and intravenous rocuronium (2.5mg/kg/hr) were used to achieve anesthesia and diaphragmatic muscle immobilization, a requirement for optimal cardiac image acquisition. Swine were ventilated with an oxygen-isoflurane (1-2%) mixture and maintained at a surgical plane of anesthesia throughout the procedures. Continuous vital signs, pCO2 levels, and single lead ECG were monitored. Unless otherwise noted, swine were humanely euthanized by a certified veterinary technician using sodium pentobarbital (100 mg/kg).

Chapter 2 **Background**

2.1 Myocardial perfusion and fMBV

At the heart of ischemic cardiovascular disease is the inability to maintain adequate perfusion, and therapeutic interventions currently rely on diagnostic estimation of ischemic burden. Three physiological parameters contribute tissue perfusion: vascular blood flow, blood volume, and oxygen extraction fraction (OEF).[21] As indicators of tissue perfusion, these parameters lend insight into the local exchange of gases, nutrients, and metabolites. Fundamentally, adequate perfusion is necessary for tissue integrity and organ function. In the setting of coronary stenosis, the effects of vasodilation and capillary recruitment combine to increase the baseline fractional myocardial blood volume (fMBV) distribution in the intramyocardial vascular space via capillary recruitment.[22] These compensatory changes result in decreased myocardial perfusion reserve.[23] The presence of elevated fMBV has been proposed as a compensatory response to myocardial hypoperfusion downstream from a significant coronary stenosis,[24] whereas decreased or low fMBV reflect capillary pruning or diseased microvasculature.[25]

2.2 MRI T1 mapping pulse sequences for multicompartment analysis

Along with proton density, the longitudinal and transverse relaxation time constants T1 and T2 represent the most fundamental determinants of the nuclear magnetic resonance (NMR) properties of a biochemical medium. The longitudinal relaxation of a water proton, often described as “spin-lattice” relaxation, results from its interaction with its local chemical environment, composed of a lattice of lipids, proteins, and other macromolecules. In contrast, the transverse (or “spin-spin”) relaxation of a water spin results from its interactions with other water protons. The relative T1- or T2-weighting of the signal generated by an MRI pulse sequence is among the central governing sources of contrast in MR images. As the T1 and T2 behavior of a given water spin are both affected by its local biochemical environment, the macro-scale T1 and T2 characteristics of biological tissues are also determined by their biochemistry. In general, long T1 times are associated with biochemical environments characterized by small, loosely bound molecules, whereas short T1 times are associated with large or tightly bound molecules. T1 changes within a given tissue type are often used as a proxy for a change in the water content or local blood volume fraction of that tissue, as free water demonstrates a very long T1.

In addition to T1 time [ms], the longitudinal relaxation behavior of a medium can also be expressed in terms of its inverse, the longitudinal relaxation rate R1 [s^{-1}]. The T1- or T2-modulation of an MRI contrast agent is typically described by its r1- or r2-relaxivity, often denoted as “r1” or “r2”. Expressed in $s^{-1}mM^{-1}$, these relaxivity constants describe the change in measured R1 or R2 as a result of an increase in contrast concentration of 1.0 mM.

Within the last decade, MRI pulse sequences designed to map T1 in the myocardium have gained ground within CMR, as a means of quantitative assessment of myocardial tissue properties. Several such myocardial T1 mapping pulse sequences are available.[26–29] The Modified Look-Locker Inversion recovery (MOLLI) sequence is the most commonly used magnetic resonance imaging (MRI) pulse sequence for clinical T1 mapping.[26] Two-dimensional MOLLI T1 mapping applies a 180° inversion pulse followed by multiple single-shot acquisitions acquired at varying echo times (TE times or TEs) over several heartbeats, followed by a recovery period of several heartbeats.[26] Different variants of the MOLLI framework exist which acquire data over varying numbers of heartbeats, and are described based on these acquisition schemes. For example, the 5(3)3(3)3 MOLLI acquisition used in this body of work spans 17 heartbeats, acquiring data during the first five beats, followed by a three-beat recovery period, acquiring data for another three beats, permitting a second three-beat recovery period, and acquiring data for a final three beats.[30]

As these T1 measurement schemes rely on a set number of heartbeats to acquire data and allow for signal relaxation, variations in heart rate can affect the apparent T1 under otherwise identical conditions. To address the heart rate-dependency of MOLLI T1, sampling schemes such as the 5(3)3(3)3 or 4(1)3(1)2 schemes, which acquire most of the total data following a single inversion, have been evaluated for accuracy and precision.[31,32] New T1 fitting algorithms have also been developed to address this limitation. In this work, we fit MOLLI T1 using the Instantaneous Signal Loss (InSiL) algorithm minimize T1 error at high heart rates (>80 bpm).[33]

Novel T1 mapping pulse sequences have also been developed which rely on a similar ECG-gated multi-heartbeat framework as the MOLLI sequence, but with variations in the signal perturbation or readout strategy. The FLASH-MOLLI sequence, which uses a spoiled gradient echo readout, and its accompanying BLESSPC T1 fitting algorithm were developed to limit off-resonance artifacts at 3T.[34] Likewise, the saturation-recovery single-shot acquisition (SASHA) sequence was developed to improve the accuracy of cardiac T1 mapping by replacing the inversion pulse in MOLLI with a saturation pulse.[27] Overall, the MOLLI, FLASH-MOLLI, and SASHA sequences differ in accuracy and precision for quantification of T1 relaxation time.[30,35] Because of its broad availability and relatively greater precision,[30] the 5(3)3(3)3 MOLLI sequence is the primary T1 mapping method used in this work.

2.3 T1 reactivity

Myocardial T1 relaxometry is affected by both tissue water and extracellular matrix content. Because coronary vasodilation and capillary recruitment increases the MBV distribution in the intramyocardial vascular space, one expects native (non-contrast) tissue T1 to lengthen in healthy myocardium in response to vasodilator stress, while the response of T1 in ischemic myocardium is severely blunted.[36] As a result, the relative difference in native T1 between rest and peak vasodilator stress states, or T1 reactivity, has been used as an alternative method to quantify myocardial perfusion reserve.[37] Recent findings suggest that native T1 reactivity can be used to distinguish between remote and ischemic myocardium,[36,37] and has spurred interest in using T1 reactivity as a biomarker for tissue perfusion. However, native T1 reactivity has a narrow dynamic range.[36,37] As an off-label intravascular MR contrast agent, ferumoxytol (Feraheme, AMAG Pharmaceuticals, Waltham, MA), is an ultrasmall superparamagnetic iron-oxide nanoparticle that is clinically approved for intravenous treatment of iron deficiency anemia and is not metabolized by the kidneys.[10–15] Early hypothesis-generating data suggest that ferumoxytol, with its long intravascular fidelity and high r1, increases the apparent T1 reactivity of myocardium by sensitizing myocardial T1 to vasodilation.[19]

2.4 Fractional myocardial blood volume (fMBV)

Direct estimation of fractional tissue blood volume using MRI remains an area of intense research because it allows for a comprehensive evaluation of tissue or organ perfusion when combined with assessment of tissue blood flow and oxygen extraction fraction. Current quantitative clinical MRI approaches to identify perfusion surrogates rely on dynamic gadolinium-enhanced MRI.[38,39] Several clinically-relevant models exist,[40] but all are limited by the lack of a true intravascular agent that is available in the clinic. The use of fractional blood volume as an indicator of overall tissue perfusion has broad applications for vital organs such as the heart, brain, kidney, and liver, but is most actively used in tumor imaging and staging. We focus on the fractional myocardial blood volume (fMBV). In the setting of elevated myocardial oxygen consumption, MBV and myocardial blood flow (MBF) demonstrate a non-linear relationship.[41,42] As a result, fMBV provides a more specific association with oxygen demand, and thus provides additional insight into myocardial perfusion beyond what is provided by MBF alone.[43] Multi-compartmental modelling can be used to quantify fMBV from contrast-enhanced cardiac MRI.[44,45] One major challenge for the measurement of fMBV is the biodistribution of the contrast agent. Contrast agents with true intravascular properties for fMBV studies are an obvious choice because they eliminate the need to model contrast leakage into the extravascular space.[38,39] One such agent is ferumoxytol. Its long intravascular half-life (10-14 hours) and high r1 (9.5 s^{-1} mM^{-1} at 3.0T in human plasma at 37°C)[7,8] make ferumoxytol an ideal intravascular contrast agent for estimating fMBV.[46]

2.5 Tissue compartmental modelling: theory and limiting cases

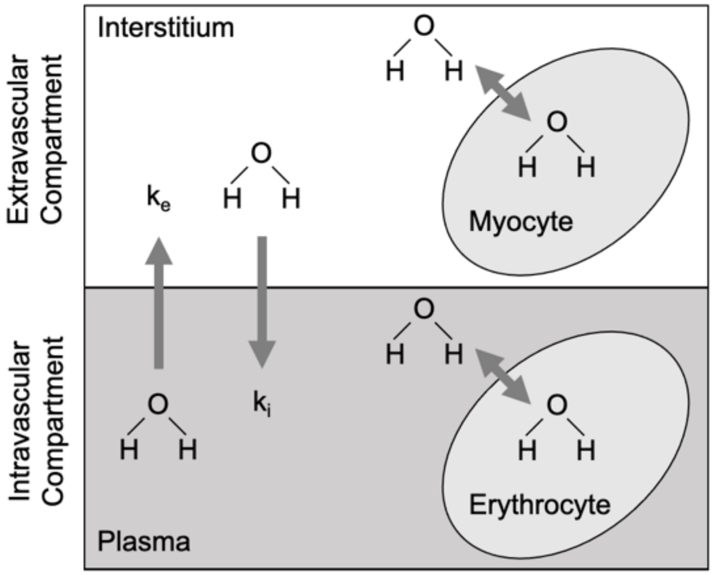

Figure 2.1. Illustration of spin relaxation environments included in multi-compartmental models of myocardial tissue.

Estimation of fMBV requires consideration of both contrast agent distribution volume and water exchange. Both the transvascular water exchange and transcytolemmal water exchange may affect MRI contrast and the apparent concentration of the contrast agent in the imaging voxel of interest. Although ferumoxytol functions as an intravascular contrast agent,[47] the iron core has superparamagnetic properties and interacts with water protons that diffuse freely between the intravascular and extravascular spaces. Therefore, the post-contrast MRI signal intensity within any imaging voxel depends on both fMBV and the rate of exchange of water protons between the intravascular and extravascular spaces. Figure 2.1 illustrates a 2-compartmental model of myocardial tissue and spin interactions along with respective representative rate constants.

Prior work in human and animal studies has demonstrated that water exchange is both subject- and tissue-specific.[47–49] The dependence of signal intensity on the rate of water exchange can be illustrated by the limiting cases of slow-exchange and fast-exchange (Figure 2.2). In the slow-exchange limit, water protons cannot diffuse across the vessel wall, and the signal intensity change in the myocardium is attributable entirely to the intravascular T1 shortening. In this limit, the Hazlewood model[44] simplifies to:

$$fMBV_{slow} = \frac{\Delta S_{myo}}{\Delta S_{blood}}$$

where ΔS is the difference in MR signal between a native (non-contrast) and a post-contrast image.[45] In the fast exchange limit, water protons diffuse so rapidly across the vessel wall that they can be assumed to experience a uniform degree of T1 shortening due to interaction with ferumoxytol. In the latter limit, the Hazlewood model simplifies to:

$$fMBV_{fast} = \frac{\Delta R1_{myo}}{\Delta R1_{blood}}$$

where R1 is the longitudinal relaxation rate and represents the reciprocal of the longitudinal relaxation time T1.

At either the slow- or fast-exchange limit, fMBV could be computed from a single native and a single post-ferumoxytol T1-weighted image. However, neither exchange limit accurately represents myocardial physiology. Oversimplification of a parameterized model can result in increased bias and variance, and either exchange limit model can significantly over- or underestimate fMBV, dependent on contrast agent concentration. To accurately quantify fMBV, water exchange must be simultaneously determined using a multi-compartmental model.

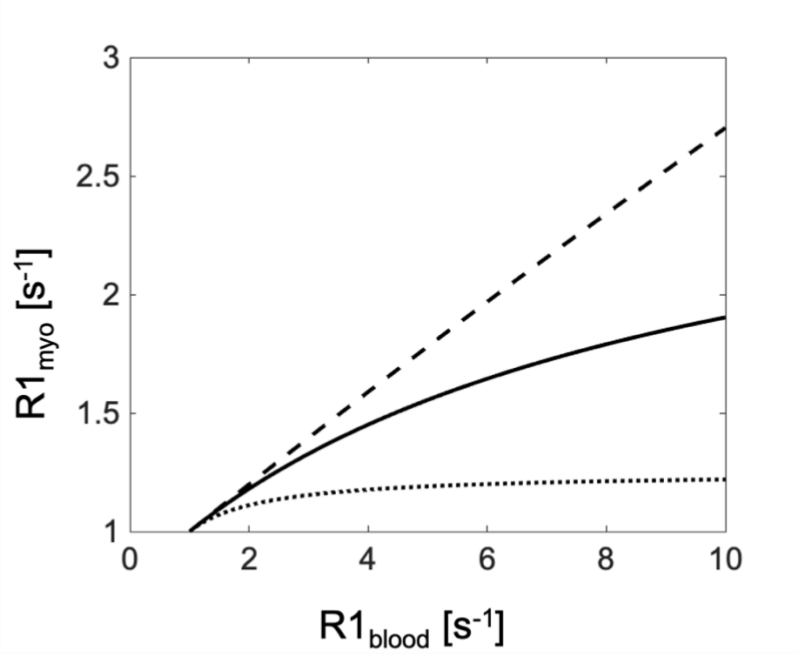

Figure 2.2. Dependence of myocardial longitudinal relaxation rate $R1_{myo}$ on blood pool relaxation rate $R1_{blood}$ under varying water exchange conditions. In all cases, fMBV = 15%, $\lambda = 0.75$, and $R1_{ev} = 1.0\ s^{-1}$. In the intermediate exchange case (solid line), $k_i = 5.0\ s^{-1}$. In the limiting cases of fast exchange, ki = 100 s^{-1} (dashed line) and in the setting of highly restricted water exchange, $k_i = 10^{-7}\ s^{-1}$ (dotted line).

Hazlewood et al. provided the initial mathematical formulation used to quantify the varying relaxation rates R1 or R2 of water across N different relaxation environments, as well as the relative volume of tissue water in each compartment.[44] Donahue et al. expanded upon Hazlewood's work by examining the accuracy and precision of simple slow and fast-exchange models for tissue blood volume estimates with intravascular T1 contrast agents.[45] Schwarzbauer et al. demonstrated the feasibility of simultaneously quantifying fractional blood volume and water exchange using a multi-dose contrast enhanced imaging scheme.[48] Bjornerud et al. modified Schwarzbauer's blood volume model to account for biexponential relaxation, mitigating overestimation of water exchange rates in the setting of greater fMBV.[49] We adapted the latter formulation of the two-compartment water exchange model in this study. The two-compartment water exchange model[48,49] can be described by the following equation:

$$R1_{myo}{}' = \frac{2}{\frac{-c_1}{u_1} - \frac{c_2}{u_2}}$$

where

$$fMBV = \lambda \frac{k_e}{k_e + k_i}$$

$$PS = \ k_i \ \times \ fMBV$$

$$a = R1_i + \frac{PS}{fMBV} + R1_e + \frac{PS}{\lambda - fMBV}$$

$$b = \sqrt{\left(R1_i + \frac{PS}{fMBV} - R1_e - \frac{PS}{\lambda - fMBV}\right)^2 + \frac{4PS^2}{fMBV(\lambda - fMBV)}}$$

$$u_1 = \frac{a + b}{2}$$

$$u_2 = \frac{a - b}{2}$$

$$c_1 = \frac{2}{u_1 - u_2} \times \left(u_2 - R1_e\left(1 - \frac{fMBV}{\lambda}\right) - R1_i\left(\frac{fMBV}{\lambda}\right)\right)$$

$$c_2 = \frac{-2}{u_1 - u_2} \times \left(u_1 - R1_e\left(1 - \frac{fMBV}{\lambda}\right) - R1_i\left(\frac{fMBV}{\lambda}\right)\right)$$

$R1_{myo}$' [s-1],, calculated myocardial longitudinal relaxation rate

fMBV [%, or unitless], fractional myocardial blood volume

λ [unitless], tissue-blood partition coefficient

k_e [s^{-1}], extravascular water exchange rate

k_i [s^{-1}], intravascular water exchange rate

PS [s^{-1}], permeability-surface area product

$R1_i$ [s^{-1}], left ventricular blood pool longitudinal relaxation rate

$R1_e$ [s^{-1}], extravascular longitudinal relaxation rate

2.6 Development of a two-compartment model for estimation of fMBV

Using a two-compartment model of the myocardium, which divides a unit of tissue into an intravascular compartment (composed of plasma and red blood cells) and an extravascular compartment (composed of the interstitium, myocytes, and other cells),[44] the fMBV can be estimated. In the 2-compartmental model, the intravascular and extravascular compartments represent separate relaxation environments, in which the longitudinal relaxation rate R1 of unbound water protons differs due to exposure to the intravascular contrast agent. In this formulation, an excited water proton spin will spend some fraction τ_i of time in the intravascular compartment, and some fraction τ_e in the extravascular compartment. These residence times (τ_i and τ_e) are inversely related to the intercompartmental exchange rates k_i and k_e, the rates at which water enters the respective compartments. A single excited spin is exposed to a relaxation environment with $R1_i$ during the time it spends in the intravascular compartment and $R1_e$ during its time in the extravascular compartment. As a result, the overall relaxation rate of the myocardial tissue is influenced by the water relaxation rate of each compartment. On the scale of a population of spins in a two-compartment system, the longitudinal relaxation of the bulk magnetization following an excitation pulse can be described by a biexponential function, as formulated by Bjornerud et al.[49] While water also diffuses into and out of cells in both compartments, transcytolemmal water exchange has been shown to be sufficiently fast relative to vascular exchange to justify a two-compartment, single-exchange model.[45,50–52]

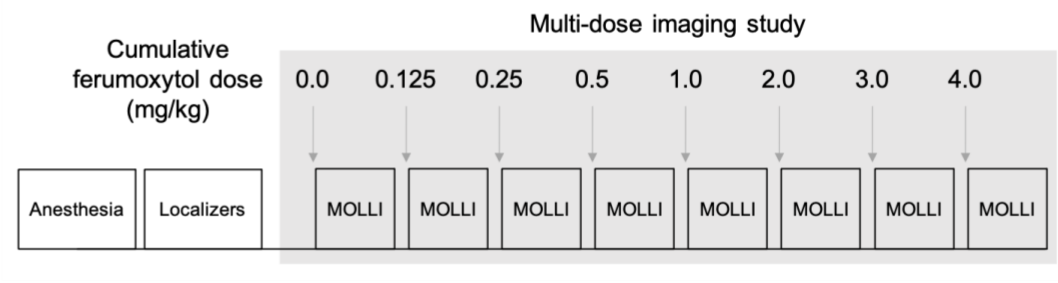

Figure 2.3. Ferumoxytol multi-dose T1 mapping study protocol.

Applying Bjornerud et al. and Schwarzbauer's blood volume model[48,49] to our current approximations of fMBV using ferumoxytol as an intravascular contrast agent, the observed longitudinal relaxation rate of myocardial tissue ($R1_{myo}$) is modeled as a function of five parameters: 1) the intravascular longitudinal relaxation rate ($R1_i$), 2) the myocardial extravascular longitudinal relaxation rate ($R1_e$), 3) the fMBV, 4) the intravascular water exchange rate k_i, and 5) the tissue-blood partition coefficient ($\lambda = \rho/\rho_i$, the ratio of the proton spin densities of tissue and blood). fMBV is related to k_i and the extravascular water exchange rate k_e by the expression

$$fMBV = \lambda \frac{k_e}{k_e + k_i}.$$

$R1_{myo}$ and $R1_i$ can be obtained from myocardial T1 maps acquired at steady state over a range of cumulative ferumoxytol doses. These repeated measurements of $R1_{myo}$ and $R1_i$ can be plotted and describe the ferumoxytol dose response of the myocardium and LV blood pool. After constructing these dose-response curves (whole myocardium or segmental), a constrained nonlinear multivariable optimization solver can be used to find the point (fMBV, $R1_e$, k_i, λ) that minimizes the sum of squared error between the calculated $R1_{myo}$' and the measured $R1_{myo}$.[53–55]

Two-compartment models of fMBV typically fit four parameters (fMBV, $R1_e$, k_i, λ) to a measured dose response curve ($R1_{myo,}$ $R1_i$). Consistent with the principle of parsimony whereby the least number of parameters that adequately describe the phenomena is recommended,[56] we developed a method to estimate $R1_e$ directly from the ($R1_{myo,}$ $R1_i$) curve in order to use a three- rather than four-parameter fit. We assumed that the intravascular compartment of the myocardial tissue (the volume of blood in the capillary bed) and the LV blood pool had equal r1 at contrast steady state; the time to steady-state duration was determined in a pilot study and is outlined in the section on image acquisition. As the cumulative ferumoxytol dose was increased such that the $R1_i$ matched $R1_e$, the contrast between the myocardium and LV blood pool was nulled ($R1_e = R1_{myo} = R1_i$). As the cumulative ferumoxytol dose was further increased, the blood pool-myocardium contrast was inverted. We estimated $R1_e$ by performing a simple linear interpolation to find the intersection of the blood and myocardial segmental ferumoxytol dose-response curves. This treatment assumed that $R1_e$ was uniform throughout the myocardium and independent of ferumoxytol dose. While this method ignored the effect of water exchange on $T1_e$ as the ferumoxytol dose was increased, the crossover of blood and myocardial T1 occurs in the low dose range where the fast-exchange assumption is more applicable. This method allowed us to fit three parameters rather than four, thus simplifying the two-compartment model.

2.7 **Image processing in tissue compartmental modelling**

This method can be implemented on a pixel-wise basis to map fMBV. Following T1 fitting and image registration T1 is converted to a volume of measured R1 with dimensions (*L, M, D*). (*L, M*) describes the dimensions of the region covering the whole myocardium, while *D* represents the number of ferumoxytol doses (including 0.0 mg/kg) in the multi-dose imaging study. Each pixel (*l, m*) in the masked registration region corresponds to a one-dimensional vector with dimension (1, 1, *D*). This vector $\overrightarrow{R1_t}$ contains the R1 measured in voxel (*l, m*) at each dose *d*. Together, $(\overrightarrow{R1_v}, \overrightarrow{R1_t})$ defines the discrete signal input curve in voxel (*l, m*). The tissue compartmental model takes the signal input curve $(\overrightarrow{R1_v},\ \overrightarrow{R1_t})$ in each voxel, as well as $R1_e$ in each voxel, as inputs. Subject to a set of pre-defined upper and lower bounds on the physiologic parameters fMBV, k_i, and λ, an optimization engine (fmincon, MATLAB)is used to identify the solution (*fMBV*, k_i, λ) which produces a predicted $R1_t$' with a minimal sum-squared error relative to the measured $R1_t$. This optimization is repeated for each pixel (*l, m*) over the masked registration region. The model-fitted matrices of estimated fMBV and water exchange rate can be exported spatial maps in DICOM file format for further data analysis.

Although compartmental modelling approaches have shown early promise for identification of myocardial ischemia in large animal models,[57] pixelwise mapping of fMBV is complicated by the need for a robust and reliable image processing pipeline. The combination of multiple parametric mapping approaches used to estimate fMBV compounds common technical challenges of parametric mapping. A reliable, accurate image registration approach is essential. Prior studies have developed[58] and adapted[59] image registration models designed for physiologic parametric mapping applications with MRI. Additionally, appropriate boundary conditions are necessary to ensure that a nonlinear optimizer can consistently converge on a solution when fitting for fMBV and other physiologic parameters.

Chapter 3 A novel swine model of myocardial ischemia using 3D printed intracoronary flow-limiting implants

3.1 Introduction

Animal models of acute and chronic coronary stenosis have been developed for preclinical research using both open- and closed-chest techniques. The most popular open-chest method relies on ameroid constrictors,[60–62] which are small, rounded clamps that can be fixed around an exposed coronary artery, restricting its diameter.[61] Deploying ameroid constrictors can be logistically difficult, requiring aseptic surgery to expose the coronary artery, placement of the constrictor on a beating heart, and closure of the pericardium and chest.[60] A minimum recovery period of 10 days is recommended and a recovery period of seven weeks is typically observed.[60,63–65] While ameroid constrictors have the benefit of not introducing any foreign object into the vasculature, open-chest surgery may confound the results of acute investigations.

In recent years, 3D printing technology has found increased adoption in cardiovascular research and clinical practice as a tool for education and intervention planning.[66–68] 3D printing shows promise for the development of vascular grafts, heart valves and cardiac muscle tissues in surgical interventions.[69,70] Because 3D printing can use a variety of MR compatible resins and bio-inks, researchers recently pioneered a percutaneous approach for delivery of rapid prototypes such as 3D printed implants into vascular lumen.[17] Despite increasing research and clinical applications, 3D printing has not been used to facilitate creation of large animal models with coronary stenosis.

In the setting of coronary stenosis, myocardial hypoperfusion results. With further blood flow obstruction, myocardial ischemia in the segment subtended by the obstructed coronary vessel will ensue.[71] To diagnose obstructive coronary disease, exercise or pharmacologic stress perfusion MRI can be performed to document inducible ischemia.[72] The availability of an MRI-compatible, minimally invasive, relatively inexpensive, closed-chest acute swine model would facilitate more rapid, cost-effective, translational research in IHD. In this work, we sought to develop a closed-chest swine model of IHD using high-resolution 3D printed epicardial coronary implants to create focal, artificial coronary stenoses. Based on quantitative coronary angiography, in-vivo cardiac MRI, and gross pathology, we aim to demonstrate the feasibility and efficacy of our new minimally invasive, rapid prototyping technique.

3.2 **Methods**

Design and manufacturing of heparin-coated epicardial coronary implant

Our intracoronary stenosis implants were designed to fit securely in the mid to distal left anterior descending artery (LAD), causing an acute coronary narrowing after percutaneous deployment. The 3D printed implant design reflected the shape, contour, and caliber of coronary vessels and had rounded edges to minimize potential for vessel injury (Figure 3.1 a-d). A library of implant sizes with a range of inner diameter, outer diameter, and length was available for use in the catheterization lab. An appropriately sized implant was selected in the cath lab based on swine coronary size, coronary guide catheter diameter, and degree of desired stenosis. We designed intracoronary implants using Autodesk Tinkercad (Autodesk Inc., San Rafael, California). Our in-house fabrication lab (LuxLab, UCLA) printed the implants from Formlabs grey resin (RS-F2-GPGR-04, Formlabs Inc., Somerville, MA) using a Formlabs Form 2 3D printer with a minimum XY feature size of 150 µm. Formlabs grey resin was chosen over more flexible commercial 3D printing resins to minimize compressibility, preventing collapse of the implant following deployment. After printing, we removed support materials that were created as part of the 3D printed proofs. To prevent thrombus formation, implants were dip-coated in a 25% heparin solution (Surface Solutions Laboratories, Inc., Carlisle, MA) with an aziridine crosslinker and allowed to air-dry for 24 hours. For quality control of the implants and to ensure minimal change in the dimensions of the implants, we visually inspected each implant for surface imperfections using a magnifying glass and measured the length, inner diameter and outer diameter of the implants following the application of the heparin coating using digital calipers (Clockwise Tools, Valencia, CA). A limited set of pin gages (Deltronic, Santa Ana, CA) were used to confirm the nominal accuracy of the digital caliper measurements.

Deployment of implant into swine models and fluoroscopic evaluation of implant location and extent of coronary narrowing

In thirteen 25-40 kg male swine (S&S Farms, Ramona, CA) we achieved anticoagulation with intravenous heparin (5000-10000 units to achieve a target activated clotting time >350 s). We gained femoral arterial access and engaged the left main coronary artery using a guide catheter under fluoroscopic guidance. We assembled the implant deployment apparatus by 1) nesting a deflated, over-the-wire, coronary balloon angioplasty catheter (NC Trek, Abbott Laboratories, Abbott Park, Illinois, USA) within a mother-and-child catheter (GuideLiner, Teleflex, Minneapolis, MN, USA), 2) mounting the implant onto the angioplasty balloon, and 3) inflating the balloon to 2-3 atmospheres to stabilize the implant's position between radiographic markers on the angioplasty balloon.[17] Under fluoroscopic guidance, we advanced the assembled implant-balloon-loaded-mother-and-child catheter to the vessel of interest, positioned the implant in the targeted segment, and acquired angiograms to assess the stability of the implant position. We then deflated and retracted the balloon through the mother-and-child catheter, leaving the implant in place. We performed angiograms in orthogonal views to document the new artificial stenosis within the vessel and to estimate the severity of stenosis. We deployed implants in either the mid to distal LAD (left anterior descending coronary artery) or mid LCX (left circumflex coronary artery).

MRI for evaluation of implant-induced regional wall motion abnormalities, myocardial perfusion, and infarction.

Regional wall motion abnormalities, such as myocardial hypokinesis and akinesis, indicate hypoperfusion and ischemia in the territory targeted by the implanted coronary stenosis. To assess for these surrogates of myocardial perfusion, we initiated MR imaging within one hour of femoral arterial access. We used a whole body, 3.0 Tesla clinical magnet (Prisma, Siemens, Germany) equipped with phased-array coils. The image acquisition protocol is shown in Figure 3.1e. After initial localizers, we acquired short- and long-axis cine images using a gradient-echo sequence to evaluate regional wall motion of the left ventricle (n=13). [FOV = 292 x 360 mm, matrix size = 102 x 126, TR = 5.22 ms, TE = 2.48 ms, slice thickness = 6 mm, pixel bandwidth = 450 Hz, flip angle = 12˚].

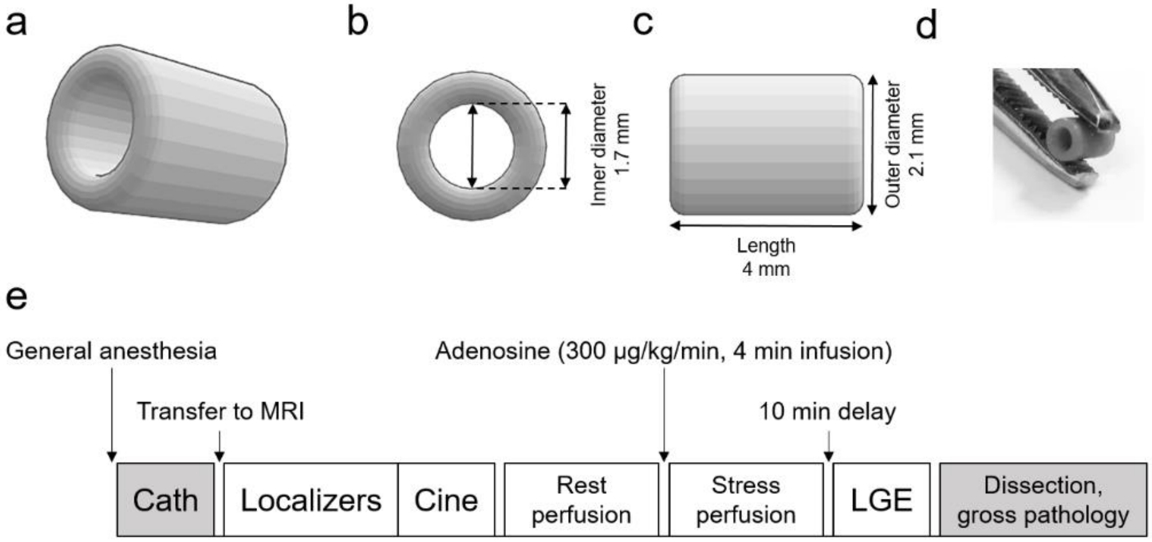

Figure 3.1. Design of 3D-printed coronary implant and MR imaging protocol. Oblique view (a), short-axis cross-sectional view (b) and long-axis side view (c) of an implant. The printed 3D implant is shown in (d). Following catheterization, subjects were transferred to MRI suite for imaging (e).

To visualize myocardial perfusion defects caused by the implanted stenosis, we performed gadolinium-enhanced first pass perfusion imaging (n=6; gadobutrol, Gadavist, Bayer, Whippany, NJ, USA; 0.1 mmol/kg, 5 ml/sec at rest and at peak stress) under conditions of rest and at peak pharmacologic stress (n=6; adenosine, 300 µg/kg/min, 4 min infusion).[73] Inducible myocardial ischemia is indicated by the presence of a visible perfusion defect at stress and the absence of a perfusion defect at rest or by a rest perfusion defect that increases in extent at peak stress. We used a spoiled-gradient-echo perfusion sequence with representative parameters: FOV = 320 x 320 mm, slice thickness = 10 mm, matrix size = 130 x 130, TR = 2.5 ms, TE = 1.1 ms, pixel bandwidth = 650 Hz, flip angle = 12˚. To exclude the presence of acute myocardial infarction in the segment subtended by the artificial coronary stenosis, we performed late gadolinium enhancement (LGE) imaging (n=6) using an ECG-gated, segmented, spoiled gradient-echo phase-sensitive-inversion-recovery sequence [FOV = 225 x 340 mm, slice thickness = 8 mm, matrix size = 131 x 175 mm, TR = 5.2 ms, TE = 1.96 ms, inversion time (TI) =optimized to null the myocardium, pixel bandwidth = 465 Hz, flip angle = 20˚] at 10 minutes after the second bolus of gadolinium infusion.

Stenosis implant retrieval and post-mortem tissue histopathology examination

After MR image acquisition and euthanasia, we performed a lateral thoracotomy, excised the heart, and exposed the coronary arterial vasculature. After careful dissection of the coronary vessel, we located the epicardial coronary implant by visual inspection. We removed and inspected the implants for intraluminal thrombus formation. We evaluated the exposed coronary vessel for abrasions by gross inspection. We rinsed explanted hearts from three subjects in saline, sliced the ventricles parallel to the atrioventricular sulcus from apex to base (~1cm thickness), digitally photographed the fresh tissue, and then incubated the slices in 1% solution triphenyltetrazolium chloride (TTC) buffered in 0.2 M Tris buffer (pH 7.8) at 37ºC for 5-7 minutes as previously described.[74] TTC staining causes regions of viable myocardium to appear deep or dark red, and infarcted /necrotic regions bright white. Previous work has shown that the spatial extent of enhancement on LGE images correlates closely (r > 0.95) with the spatial extent of infarction on TTC staining.[75]

Image analysis and statistics

To compare the dimensions of the implanted stenosis with the degree of coronary narrowing visible on angiograms, vessel diameter and minimum lumen diameter were quantified in orthogonal fluoroscopic images using the Osirix DICOM viewer (Pixmeo, Bernex, Switzerland), with the guide catheter as a size reference (n=12). Percent diameter stenosis was evaluated relative to a reference vessel diameter immediately proximal to the implant, as previously described.[76] A reader (>8 years’ experience in cardiovascular MRI and perfusion imaging and who had no identifying information about the location of coronary implant placement) visually inspected the first-pass perfusion images for perfusion defects (ischemia) and evaluated the LGE images for the presence or absence of myocardial infarction using a commercially available software (Argus, Siemens, Erhlangen, Germany). We visually assessed the cine images for regional wall motion abnormalities and performed quantitative feature-tracking strain analysis (n=8 swine subjects, TomTec, 2D CPA MR). Data are summarized as mean ± standard deviation (SD). Data ranges are included where appropriate. For group comparisons of segmental circumferential strain, we used a two-tailed paired Student's t-test (MedCalc v19.1, Belgium). A p value of <0.05 was considered significant.

3.3 **Results**

Intracoronary Stenosis Implant Sizing

We created a library of coronary implants with a range of dimensions to facilitate ease of intra-operative sizing. Based on the range of swine size and the diameter of an 8F coronary guide catheter used during the experiments, the outer diameter of the implants was limited to 2.1 mm. The minimum wall thickness of the implant was 0.3 mm and their length ranged from 2.6 to 4.0 mm. Digital caliper measurements found a mean deviation from nominal implant dimensions of -0.03±0.07 mm in length, 0.00±0.06 mm in outer diameter and -0.39±0.06 mm in inner diameter following application of the heparin coating. Application of the heparin coating caused a decrease in implant inner diameter of 0.09±0.11 mm on average.

Swine survival outcomes and quantitative analysis of coronary stenosis

We deployed 13 implants in 13 swine subjects. Following implant deployment, subjects showed a median baseline heart rate of 80 bpm (beats per minute, IQR 76 – 84), systolic blood pressure (SBP) of 98 mmHg (IQR 88 – 104) and diastolic blood pressure (DBP) of 56 mmHg (IQR 51 – 62). A summary of swine subject outcomes is presented in Table 3.1. The overall animal survival rate was 85% (11 of 13). One subject developed ventricular fibrillation; one became profoundly hypotensive and died. The swine models were hemodynamically stable post-implant, completed all imaging study procedures, and survived for at least 6 hours (from implant deployment to euthanasia). We were able confirm successful deployment by retrieving the implant in 12 of 13 subjects (92%). Subject outcomes improved over the course of the study. Of the first six cases, three were fully successful (deployment, retrieval, and subject survival until completion of imaging). The latter seven cases were fully successful. During the first six cases, each implant deployment took approximately one hour to complete. During the latter seven, improvements in our deployment technique allowed us to complete implant deployment in less than 30 minutes.

Table 3.1. Summary of implant deployment procedures and results.

Subject	Location of implant	Size of implant* (OD, ID, L [mm])	Implant retrieved	Animal survived	Implant retrieved and animal survived
1	LAD	2.1, 1.5, 4	--	✓	--
2	LAD	1.5, 1.1, 4	✓	✓	✓
3	LCX	2.1, 1.5, 2.6	✓	--	--
4	LAD	2.1, 1.5, 4	✓	✓	✓
5	LAD	2.1, 1.5, 4	✓	--	--
6	LAD	2.1, 1.5, 4	✓	✓	✓
7	LAD	2.1, 1.5, 4	✓	✓	✓
8	LAD	2.1, 1.5, 4	✓	✓	✓
9	LCX	2.1, 1.5, 4	✓	✓	✓
10	LAD	2.1, 1.5, 4	✓	✓	✓
11	LAD	2.1, 1.5, 4	✓	✓	✓
12	LAD	2.1, 1.5, 4	✓	✓	✓
13	LAD	2.1, 1.5, 4	✓	✓	✓

*Mean deviation from nominal implant dimensions of -0.03±0.07 mm in length, 0.00±0.06 mm in outer diameter and -0.39±0.06 mm in inner diameter following application of the heparin coating. On average, heparin coating caused a decrease in implant inner diameter of 0.09±0.11 mm.

ID, inner diameter; LAD, left anterior descending artery; LCX, left circumflex artery; L, length; mm, millimeter; OD, outer diameter

Quantitative analysis of post-deployment fluoroscopic angiograms showed focal coronary stenosis severity ranging from 40.6% to 62.7% (mean stenosis 56.8±7.0%, n=12 swine subjects). The mean minimum luminal diameter was 0.75±0.13 mm (range: 0.63-1.04 mm) and mean vessel diameter proximal to the implant was 1.75±0.27 mm. Figure 3.2 shows an illustrative angiogram from subject 11.

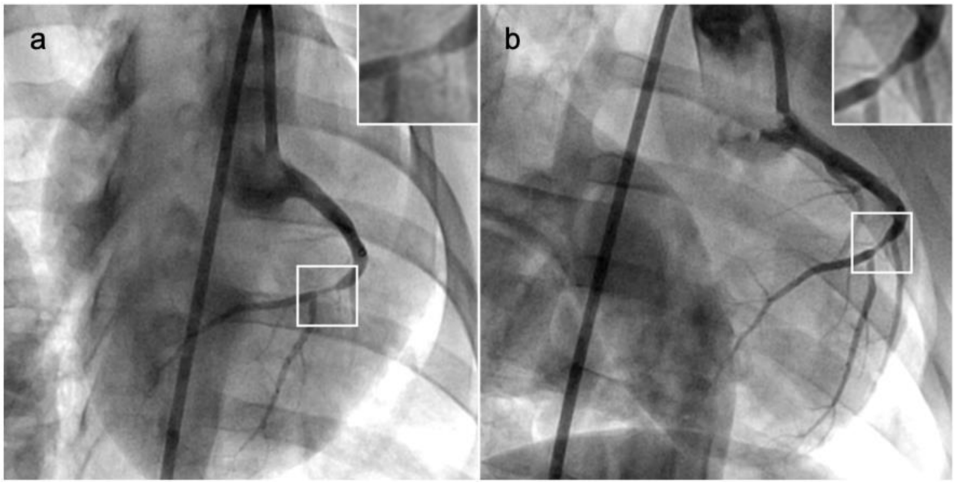

Figure 3.2. Orthogonal fluoroscopic images. Posteroanterior (PA, a) and left anterior oblique (LAO 40°, b) views from subject 11 show visible arterial narrowing (inserts) following deployment of the implant into the left anterior descending artery. Minimum lumen diameter 0.85 mm, percent diameter stenosis 59%.

MRI validation of efficacy

All thirteen subjects demonstrated visible hypokinesis in the target myocardial segment on MR cine imaging within two hours of implant deployment. Figure 3.3 shows sample MR cine images acquired in subject 2 following implant deployment, analyzed for longitudinal and circumferential strain by semi-automated endocardial border feature tracking. New regions of hypokinesis indicate a reduction in blood supply to the myocardial segment subtended by the implant, as well as the onset of myocardial stunning.[77] Subjects showed significantly decreased circumferential strain in ischemic regions compared to remote regions on Student's paired t-test (-9.1±5.8% vs -18.3±6.6%, p=0.014).

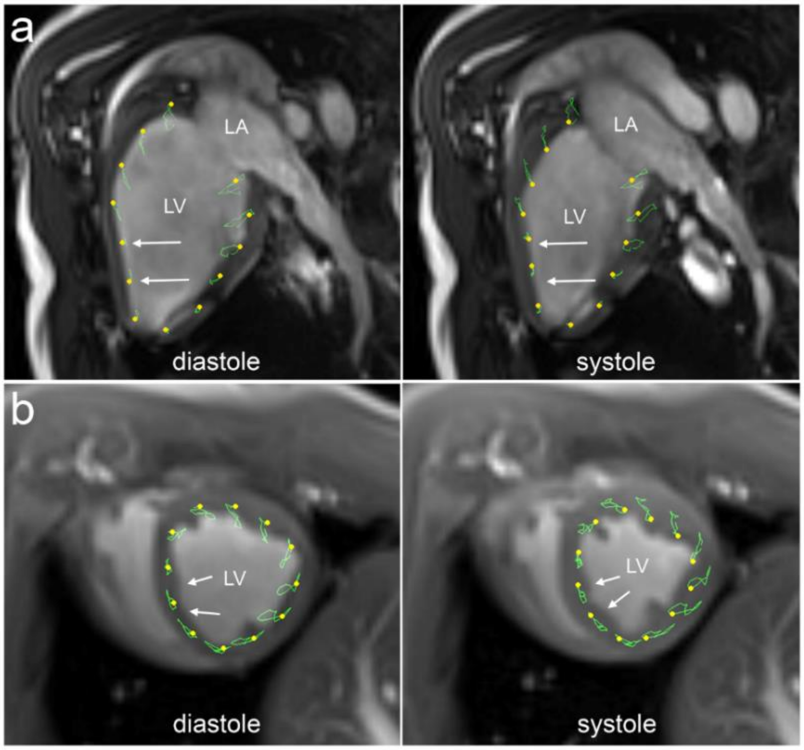

Figure 3.3. Illustrative cine MR images of a swine with a 3D-printed coronary stenosis implant in the left anterior descending artery. Two-chamber **(a)** and short-axis **(b)** left ventricular cine MR images from subject 2 show mid to distal left ventricular anterior and septal hypokinesis (white arrows).

Subjects that underwent stress perfusion imaging showed a median baseline heart rate of 81 bpm (IQR 80 – 88), SBP of 96 mmHg (IQR 94 – 102), DBP of 55 mmHg (IQR 52 – 59). At peak adenosine stress, subjects showed a median heart rate of 84 bpm (IQR 81 – 89), SBP of 76 mmHg (IQR 74 – 78), DBP of 38 mmHg (IQR 34 – 42) and rate pressure product of 6090 (IQR 5550 – 6500). There were no adenosine stress-induced adverse events. Subjects that underwent adenosine stress first-pass perfusion and LGE MRI each showed perfusion defects in the target myocardial segments without evidence of myocardial infarction. Infarcted myocardium appears hyper-enhanced on LGE images.[78] The absence of myocardial enhancement in target regions with perfusion defects indicates the presence of myocardial ischemia without infarction.

Figure 3.4a shows an illustrative example from subject 7. A rest perfusion defect is present in the basal to mid anteroseptal wall after deployment of an implant into the proximal LAD. Corresponding LGE images showed no visible myocardial signal enhancement in regions corresponding to the perfusion defect (Figure 3.5a). These findings indicate the presence of myocardial ischemia without infarction.

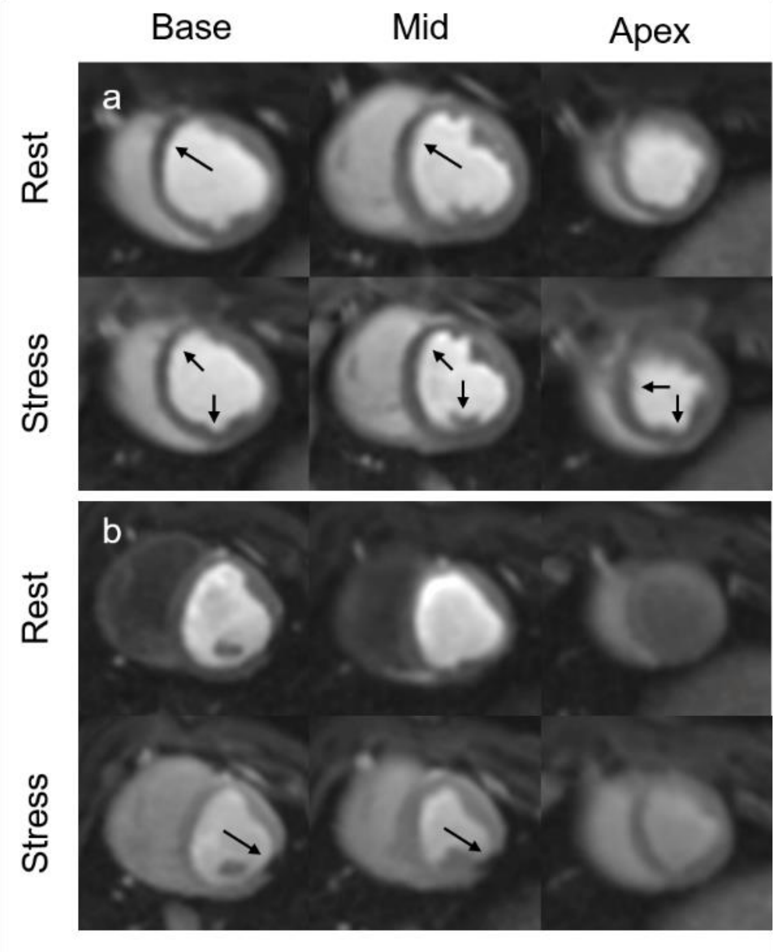

Figure 3.4. Gadolinium-enhanced rest and stress first pass perfusion images. Perfusion defect (arrows) is present in the basal to mid anteroseptal to inferior wall in subject 7 (LAD, a). Perfusion defect (arrows) is present in the basal to mid inferolateral wall in subject 9 (LCX, b).

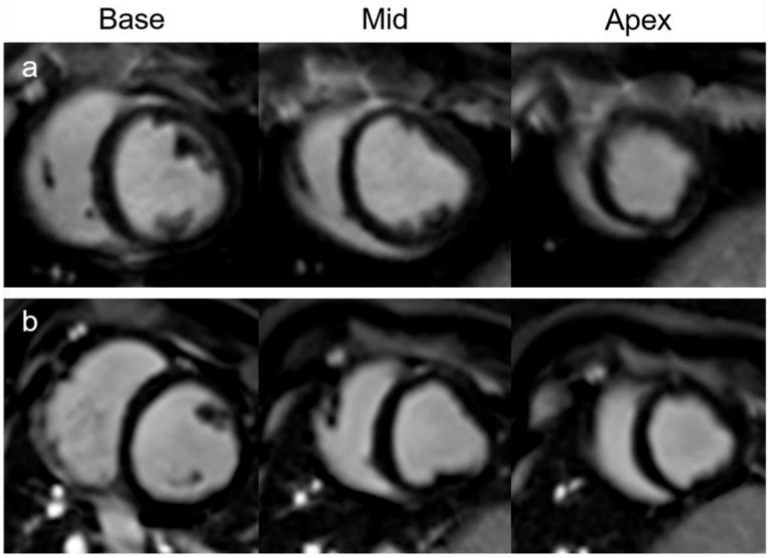

Figure 3.5. Late gadolinium-enhanced images (base, mid, apex) using a phase-sensitive inversion recovery gradient echo sequence. No evidence of myocardial infarction is visible in myocardial segments subtended by the left anterior descending coronary artery (subject 7, (a)) or the left circumflex artery (subject 9 (b)).

Post-mortem evaluation and gross pathology

Implants were retrieved from the target coronary segment in all subjects except subject 1. This indicates that our method allows investigators to control the implant location within the coronary artery with less concern about distal migration or proximal retraction during balloon removal. Only one of the early subjects showed gross abrasions in the coronary vessel upon visual inspection. Figure 3.6 provides an example from subject 9; no gross denudation of the endothelium (Figure 3.6b), and no evidence of intraluminal thrombus formation in the implant (Figure 3.6c) were observed. Explanted heart tissues from subjects 9 and 13 confirmed the absence of myocardial infarction by TTC staining (Figure 3.6d-g).

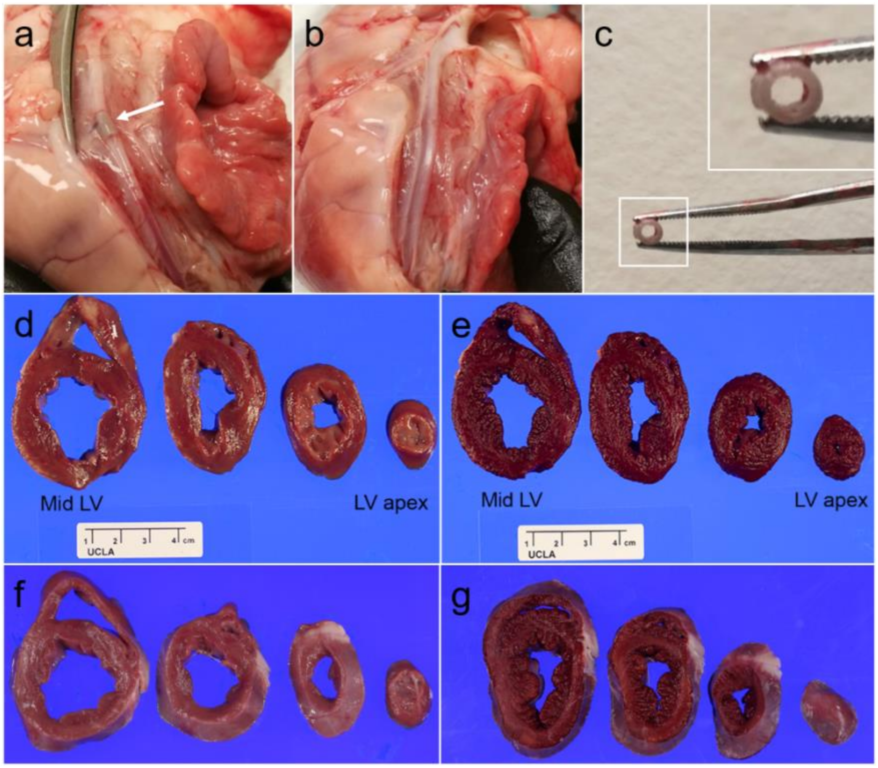

Figure 3.6. Retrieval of epicardial coronary implants from subjects 9 and 13. The implant in subject 9 is seen in the left circumflex artery (white arrow, a). There is no evidence of gross denudation of the endothelium (b). Inspection of the implant showed lack of thrombus formation (c, cross-sectional view with magnified insert). Gross specimen (d) and triphenyltetrazolium chloride staining (e) from subject 9 showed no evidence of myocardial tissue infarction in the left ventricle (LV). Gross (f) and stained (g) specimen from subject 13 likewise showed no evidence of infarction.

3.4 Discussion

Our proof-of-concept study demonstrates the feasibility and efficacy of a new minimally invasive and cost-effective percutaneous technique for creating large animal models of acute focal coronary stenosis using 3D printed epicardial coronary implants. Our method enables selective delivery into the arterial segment of interest. The resultant degree of coronary narrowing can be tailored to produce baseline hypoperfusion or vasodilator-induced ischemia without infarction or intraluminal thrombus formation. Our technique has promising applications for validation of new diagnostic MR imaging methods in IHD.

Closed-chest methods for inducing or mimicking atherosclerosis include atherogenic diets,[79,80] partially inflated angioplasty balloons,[19,81] endothelial injury models,[82] modified covered stents,[76,83] and intracoronary implanted flow reducers.[84] These methods each have distinct advantages and disadvantages. Atherogenic diets are logistically simple to implement but can take as long as six months to take effect, and results are unpredictable. Balloon angioplasty techniques are advantageous for modelling acute myocardial ischemia and reperfusion but pose challenges for models of non-occlusive coronary stenosis. Failure rates due to ventricular fibrillation can be high when complete occlusions are created in ischemia-reperfusion experiments.[81] Endothelial injury models require a waiting period to allow stenosis to develop and do not reliably induce significant stenoses in all subjects. Covered stents may prove prohibitively expensive, and stents that are not fully expanded pose a risk of collapse, triggering acute thrombosis. Stainless steel stents create MR image artifacts that can completely obscure the vessel of interest and significantly distort the surrounding image.[85] The epicardial coronary flow reducers described by Kraitchman et al. are relatively simple to deploy, but are more challenging to manufacture and are machined individually by hand.[84] They also demonstrate a relatively low success rate of 57% in two studies.[84,86]

Open-chest methods include extracoronary ameroid constrictors, and perfused explanted beating heart models.[60,87] The most popular method of inducing focal coronary stenosis in swine models remains the ameroid constrictor – a steel or plastic outer sleeve with an inner layer of casein material that swells when positioned around an artery.[61,62,88] Ameroid constrictors are difficult to implant: aseptic technique is required, as imaging studies typically follow a recovery period of seven weeks.[63] Placement of ameroid constrictors requires significant surgical expertise and may be operator-dependent with a steep learning curve. Ameroid constrictors reliably induce coronary stenosis, but variability in the rate of casein swelling leads to an inability to precisely control the degree of coronary occlusion.[89] However, the gradual development of the stenosis may be an advantage for chronic studies. The purpose of our technique is not to model the natural history of atherosclerotic disease, but to produce swine models of acute myocardial hypoperfusion for MR imaging studies.

Our new method using 3D printed implants compares favorably with existing methods on logistical simplicity, efficacy, precision, and reliability. The outer diameter of the implants was limited to 2.1 mm but could be varied if needed for larger vessels. The inner diameter was designed to accommodate a deflated, clinically available coronary angioplasty balloon. We manufactured implants with a range of lengths, allowing investigators to choose a longer implant when more severe stenosis was desired. In the cath lab, we further refined the outer diameter size selection based on the subject’s body weight and coronary size estimates at the time of catheterization. Compared to hand-machined nylon flow reducers, these 3D printed implants are simple to manufacture. Stereolithographic 3D printing produces smooth, high quality prints that can be heparin-coated for improved biocompatibility. Our implants are printed on a commercial 3D printer using a standard resin and can be made in-house or made to order by commercial printing services. 3D printing can be used to produce implants at scale from low-cost materials. This allows investigators to prepare implants with a range of dimensions and select one to fit coronary segment of interest based on intracoronary sizing in the cath lab. If a more precise, subject-specific implant is desired, a coronary CT may be performed, and coronary images can be imported into commercially available software for implant design.

Our results are comparable to those reported by Foin et al. using modified covered stents. Our implants induced a mean diameter stenosis of 56.7±7.0%. Foin et al. report a mean diameter stenosis of 54.1±5.9%.[76] Wu et al. report a mean percent diameter stenosis of 91±4% using an endothelial injury model.[82] We achieved a success rate of 75%, which is comparable to other published methods. The method most similar to our technique consists of intracoronary nylon flow reducers, which has a success rate of 57%.[84,86] Studies using ameroid constrictors typically show a success rate of 80% to 90%.[63,64,90] Our overall lower success rate compared to ameroid constrictors may be related to the initial optimization period. Our success rate was 100% after the first five cases. Relative to ameroid constrictors, intracoronary methods may have a higher rate of complications due to the introduction of a foreign body into the coronary vasculature.[91] It is known that swine coronary endothelium is sensitive to vasospasm, and as swine lack collateral vessels, they are more sensitive to sudden severe coronary occlusion.[62] Our study demonstrates that this risk can be managed with an appropriate anticoagulation strategy and use of anti-arrhythmics and nitroglycerin.

Limitations

Our study has several limitations. The measured minimum lumen diameter of the implant-induced coronary narrowing on fluoroscopic images was smaller than the measured inner diameter of the implants following heparin coating. Possible reasons include use of image viewing software rather than quantitative coronary angiography (QCA) software and streaming of contrast or out-of-plane motion. Although the 3D printed implants used in this study can be manufactured in arbitrary dimensions, we ultimately tested a small range of sizes. Likewise, while we used coronary angiography to confirm new coronary stenosis following implant placement, this method can only be used to quantify the geometry of a stenosis. The reference standard for physiologic assessment of stenosis is fractional flow reserve (FFR), measured using coronary pressure wires.[92,93] Our method can be adapted to include measurement of FFR following implant deployment. Future studies can investigate the correlation of implant size with FFR, which may better characterize the relative severity of stenosis and ischemic burden imposed by implants of varying sizes. While we used multimodal MRI to confirm the location of new perfusion defects in the targeted myocardial segment, we did not distinguish between mild, moderate, and severe perfusion defects or correlate this severity with the implant size or percent diameter stenosis. Future studies may investigate the correlation of post-implant FFR with the extent of myocardial perfusion defects.

3.5 Conclusion

Our new method for creating large animal models of focal coronary stenosis opens new avenues for translational MR imaging studies of myocardial ischemia. This swine model may be used to evaluate novel diagnostic MR imaging methods for IHD or investigations involving the physiological effect of multiple sequential stenoses or stenoses in multiple arterial branches. Future work to test a wider range of implant sizes, materials, and resulting physiological measurements are needed. Overall, our rapid prototyping method offers a success rate comparable to that of open-chest delivery of ameroid constrictors, while using percutaneously delivered intracoronary implants.

Chapter 4 Ferumoxytol-enhanced magnetic resonance T1 reactivity for depiction of myocardial hypoperfusion

4.1 Introduction

In the setting of coronary stenosis, autoregulation increases MBV resulting in decreased myocardial perfusion reserve.[23] Native tissue T1 lengthens in healthy myocardium in response to vasodilator stress. The response of T1 in ischemic myocardium is severely blunted.[36] Recent findings suggest that T1 reactivity, the relative difference in T1 between rest and peak vasodilator stress states, can be used to distinguish between remote and ischemic myocardium,[36,37] spurring interest in using T1 reactivity as a biomarker for tissue perfusion. However, native T1 reactivity has a narrow dynamic range.[36,37] In routine clinical practice, myocardial blood flow (MBF) reserve is assessed using first-pass stress gadolinium-enhanced perfusion MRI to diagnose clinically significant coronary stenosis.[94] Prior work using contrast-enhanced echocardiography[41] and electron beam computed tomography,[42] however, suggests a nonlinear relationship between MBV and MBF; at high oxygen consumption, changes in MBV may outstrip changes in MBF.[43] By taking oxygen consumption and compensatory changes in the microcirculation into account, T1 reactivity, as a proxy for MBV change, may serve as a comprehensive estimate of tissue perfusion.[43]

Early data suggest that ferumoxytol, with its long intravascular fidelity and high r1, increases the apparent T1 reactivity of myocardium by sensitizing myocardial T1 to vasodilation.[19] We hypothesize the increase in dynamic range of T1 reactivity with ferumoxytol may also increase the sensitivity and specificity of T1 reactivity as a measure of myocardial ischemia. In this study, we sought to determine the diagnostic performance of ferumoxytol-enhanced (FE) relative to native T1 reactivity as proxies for myocardial tissue hypoperfusion.

We aim to address the following questions: 1) (Primary objective) Relative to native T1 reactivity, can FE T1 reactivity differentiate between ischemic and remote myocardium? 2) (Secondary objective) To what extent does ferumoxytol contrast affect the magnitude of MOLLI- and SASHA-derived T1 reactivity? 3) (Secondary objective) What are sensitivity and specificity thresholds and effect sizes for using FE and native T1 reactivity to predict regional wall motion abnormalities (RWMAs) as proxies for tissue hypoperfusion?

4.2 **Methods**

Swine models of acute myocardial hypoperfusion

We induced a focal single coronary vessel stenosis in the mid left anterior descending (LAD) artery in thirteen healthy juvenile male Yorkshire swine (20-40 kg, S&S Farms, Ramona, CA) using a heparin-coated, 3D printed intracoronary stenosis implant as previously described.[18] Briefly, following femoral arterial access and under fluoroscopic guidance, we percutaneously deployed the implants using a transcatheter delivery technique to induce myocardial hypoperfusion.[17] We used orthogonal angiograms to estimate the stenosis location. To determine the severity of stenosis, we used the Thrombolysis in Myocardial Infarction (TIMI) flow grading system to visually assess coronary perfusion on angiographic images (0 = no perfusion or no antegrade flow beyond the point of occlusion; 1 = penetration without perfusion, or faint antegrade flow beyond the occlusion with incomplete filling of the distal coronary bed; 2 = partial perfusion, or delayed antegrade flow with complete filling of the distal territory; 3 = complete perfusion, or normal flow with complete filling of the distal territory).[95] We measured percent diameter stenosis on angiographic images using a reference vessel diameter immediately proximal to the implant. In all swine, we maintained an activated clotting time (ACT) above 300 seconds with intravenous heparin throughout the procedure to prevent thrombus formation. This technique has been shown to reliably induce myocardial ischemia without infarction.[18]

Image Acquisition

Immediately following the intervention, the swine underwent cardiac MRI (whole body clinical 3.0 T scanner equipped with phased-array coils, Prisma®, Siemens, Germany). Following localizers, we acquired short- and long-axis cine images using a cine gradient-echo sequence to assess the location of ischemic defects, based on RWMAs. Representative scanning parameters were: FOV = 292 x 360 mm, matrix size = 102 x 126, TR = 5.2 ms, TE = 2.5 ms, slice thickness = 6 mm, pixel bandwidth = 450 Hz, flip angle = 12˚. We then performed native and FE adenosine stress testing (Figure 4.1). A left ventricular short-axis stack of T1 maps (base, mid, apex) was acquired at rest and at peak pharmacologic stress (adenosine, 300 µg/kg/min, 4 min infusion)[96] using the 5(3)3(3)3 MOLLI sequence[26] with a balanced steady-state free precession (bSSFP) readout and ECG triggering in all swine (n=13) [FOV = 240 x 300 mm, TR = 2.6 ms, TE = 1.1 ms, TI = 100 – 180 ms, slice thickness = 8 mm, pixel bandwidth = 1085 Hz, flip angle = 35˚]. Because SASHA was borne out of efforts to reduce systematic T1 measurement errors related to off-resonance, flip angle, T2 dependence, heart rate fluctuations, and magnetization transfer, we also, in 8 swine, performed ECG-triggered rest and stress native T1 mapping using the SASHA[27] (Siemens WIP 1041B) sequence (n=8) [FOV = 240 x 300 mm, TR = 2.8 ms, TE = 1.2 ms, fixed saturation time (TS) = 600 ms,[97] slice thickness = 8 mm, pixel bandwidth = 1085 Hz, flip angle = 70˚]. After native stress testing, we administered ferumoxytol (4mg/kg) over a 12-minute infusion and repeated the stress testing protocol. Following ferumoxytol infusion, we used a SASHA sequence with variable TS (81 – 634 ms). Two additional swine subjects underwent two FE MOLLI T1 stress testing cycles immediately following implant deployment in order to assess the potential interaction between hypoperfusion and time since implant deployment. Veterinary technologists used sodium pentobarbital (100 mg/kg) at the end of the study to humanely euthanize the swine subjects.

Image Processing and Analysis

In addition to the commercially available MOLLI T1 fitting algorithm, we used the Instantaneous Signal Loss simulation (InSiL) algorithm for T1 fitting of MOLLI images in order to minimize T1 error at high heart rates (>80 bpm) (MATLAB R2019b, MathWorks, Natick, MA).[33] Although inline motion-correction was available, in our hands, the algorithm did not work well for swine imaging with ferumoxytol. Thus, for images with visible motion, we co-registered raw images using a groupwise image registration method based on principal component analysis (Elastix, 5.0.0) prior to InSiL fitting.[58,98] We fit SASHA images using the inline T1 fitting algorithm (WIP 1041B MyoMap, Siemens).

Two readers independently assessed native and FE T1 maps acquired at rest and stress for image artifacts. Artifacts were graded using a 5-point Likert scale (0 = no artifacts, 1 = mild artifacts, 2 = moderate artifacts, 3 = substantial artifacts, 4 = severe artifacts) for each segment of the AHA model.[99] Segments containing artifacts graded three or greater were rejected. One reader assessed the MR cine images for RWMAs using a 3-point Likert scale (1 = normal, 2 = hypokinetic, 3 = akinetic). We categorized myocardial segments within the LAD territory with RWMA scores of two or greater as ischemic because myocardial contractile dysfunction is an indicator of hypoperfusion and the onset of myocardial stunning.[77] We chose RWMAs as the reference because both dobutamine and exercise stress echocardiography rely on RWMAs for the diagnosis of clinically relevant obstructive epicardial coronary disease and data support higher specificity with RWMAs relative to nuclear perfusion imaging.[100] We categorized segments perfused by the LAD, right coronary artery (RCA), and left circumflex (LCX) artery, that have normal wall motion as remote myocardium.

To compute pixelwise myocardial T1 reactivity maps, we co-registered rest and stress T1 maps using a nonrigid B-spline transform and an adaptive stochastic gradient descent optimization method in Elastix.[101,102] Following registration, we computed pixelwise T1 reactivity and generated T1 reactivity maps (MATLAB R2019b, MathWorks, Natick, MA). Using RWMAs present on the cine images as reference, we drew regions of interest (ROIs) (approximately 50 mm^2) within ischemic myocardial segments on T1-reactivity maps (Osirix, Pixmeo, Bernex, Switzerland). Care was taken to avoid blood pool contamination near the left ventricular endocardial border. We placed corresponding ROIs in the contralateral remote segment. Segments with artifact scores of three or greater were excluded from analysis.

Statistical Analysis

Data were tested for normality using the Kolmogorov-Smirnov test. Data are reported as mean ± standard deviation or median (IQR) according to normality. To determine whether native and FE T1 reactivity can distinguish between ischemic and remote myocardial regions in the same subject, we used paired, two-sided Student's t-tests and paired Wilcoxon signed rank tests for group comparisons. We used a two-sided Wilcoxon signed rank test to compare the blood-tissue partition coefficient λ_{fe} of ferumoxytol in ischemic and remote regions. To further evaluate the diagnostic performance of InSiL-MOLLI- and SASHA-derived FE T1 reactivity relative to native T1 reactivity as predictors of tissue perfusion, we computed the receiver operating characteristic (ROC) curves with binary variable responses based on RWMAs. The presence of RWMAs was used as an indicator of ischemia/hypoperfusion and coded as 1; normal wall motion was coded as zero. We compared the areas under the ROC curves (AUC). We report the sensitivity, specificity and threshold values associated with Youden's J statistic, max {sensitivity + specificity – 1}. The effect sizes of using native and FE InSiL-MOLLI- and SASHA-derived T1 reactivity to differentiate ischemia and remote myocardium were calculated using Glass's Δ.[103] In two additional swine subjects that received repeated cycles of adenosine stress, we used paired t-tests to evaluate the relationship between T1 reactivity in ischemic and remote myocardium relative to time. A p-value <0.05 was considered statistically significant. Statistical analysis was performed using MedCalc 19.0.5 (MedCalc Software, Ostend, Belgium).

4.3 **Results**

All 13 swine had single vessel LAD coronary stenoses of at least moderate severity. Stenosis implant length averaged 5.2 ± 1.5 mm (range = 4.0 to 8.0 mm). Angiograms showed a mean percent diameter stenosis of 54.8 ± 7.4% and a TIMI score of one (penetration without perfusion, n=4) to two (partial perfusion, n=9). No ferumoxytol-related adverse events occurred. All animals tolerated the adenosine stress testing cycles without stress testing-related complications. Native MOLLI images in one subject (n=16 segments) were rejected due to severe in-plane and through-plane motion. Seven of 448 (1.56%) remaining myocardial segments on MOLLI images were rejected while 10 of 392 segments (2.55%) on SASHA images were rejected due to image artifacts. Using a 5-point Likert scale with zero reflecting no artifacts and four reflecting severe artifacts, the mean artifact score was 0.146 ± 0.097 for InSiL-MOLLI and 0.189 ± 0.111 for SASHA. Of 180 myocardial segments scored for RWMAs, we identified 147 as normal (remote myocardium), 26 as hypokinetic and 7 as akinetic (hypoperfused, ischemic, or stunned myocardium). The segments with hypokinesis and akinesis corresponded to the LAD perfusion territories.

Pharmacologic stress

At baseline, swine showed an average heart rate of 89 ± 15 bpm (beats per minute), average systolic blood pressure of 100 ± 9 mmHg and diastolic blood pressure of 60 ± 9 mmHg, and average rate pressure product (RPP=SBPxHR, SBP=systolic blood pressure, HR=heart rate) of 8897 ± 1521. At peak adenosine infusion, the swine subjects showed an average heart rate of 89 ± 15 bpm, average systolic blood pressure of 74 ± 10 mmHg, average diastolic blood pressure of 37 ± 6 mmHg, and average RPP of 6598 ± 1337.

Native and ferumoxytol-enhanced myocardial T1

We computed the blood-tissue partition coefficient λ_{fe} of ferumoxytol using InSiL-MOLLI T1 with the expression $\lambda_{fe} = \Delta R1_{myo}/\Delta R1_{blood}$.[104] We found a median λ_{fe} of 7.5% (5.4, 10.1%) in ischemic and 6.4% (5.8, 7.4%) in remote regions, with no significant difference between remote and ischemic regions (p=0.34).

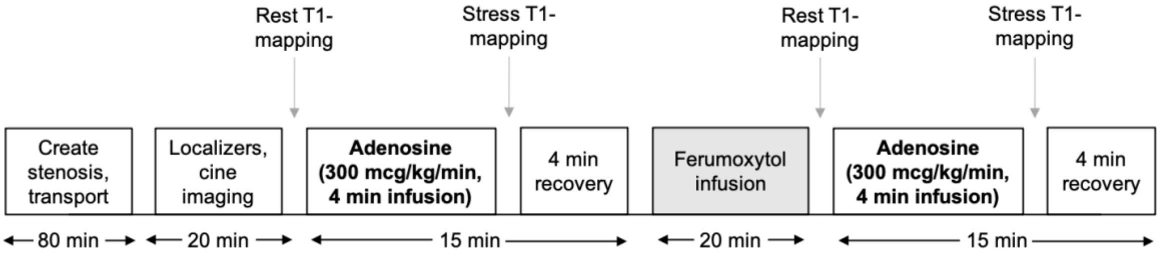

Figure 4.1. Stress testing protocol with T1 mapping at 3.0T.

Native and ferumoxytol-enhanced T1 reactivity

Both native and FE T1 reactivity were significantly different between remote and ischemic myocardial regions. Pixelwise T1 reactivity maps demonstrate dynamic differences in perfusion gradient from base to apex and visibly depict regions of blunted reactivity perfused by the mid to distal LAD territory (Figure 4.2). Because adenosine stress shortens myocardial T1 in the setting of increased ferumoxytol biostribution in the intravascular space, FE T1 reactivity is typically negative (red). Native T1 lengthens with vasodilation and thus native T1 reactivity is typically positive (blue). On both sets of maps, blunted T1 reactivity in ischemic regions (white arrows) appears pale or white. NativeT1 reactivity in remote regions was 1.9-fold higher than in ischemic regions across all subjects (T1 reactivity: 1.65±0.72% in the ischemic and 3.08±1.70% in the remote regions). Absolute FE T1 reactivity in remote regions was 3.3-fold greater than ischemic regions (FE T1 reactivity: -3.18 [-7.24, -2.53]% in ischemic and -10.43±3.69% in remote regions).

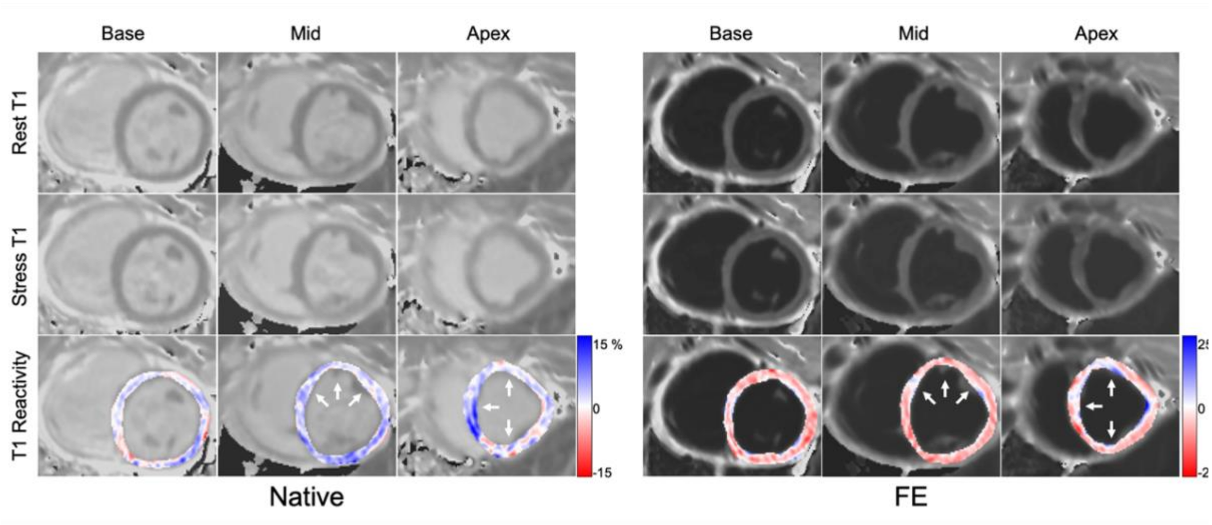

Figure 4.2. Illustrative example of native and ferumoxytol-enhanced (FE) T1 reactivity maps at 3.0T. Native (left panel; base, mid, apex) and FE (right panel; base, mid, apex) rest and stress T1 and T1 reactivity maps acquired at 3.0T using 5(3)3(3)3 bSSFP-MOLLI with InSiL fitting in a swine subject with a 3D printed intracoronary stenosis implant in the mid left anterior descending coronary artery.

The dynamic range of FE T1 reactivity was wider relative to native T1 reactivity (Figure 4.3). Ferumoxytol increased the average remote T1 reactivity by 3.4-fold with both InSiL-MOLLI ($p<0.001$) and SASHA ($p<0.001$). Ferumoxytol increased average T1 reactivity in ischemic regions by 2.5-fold with InSiL-MOLLI ($p=0.001$) and 2.9-fold with SASHA ($p=0.002$).

We found a significant difference between remote and ischemic myocardial native T1 reactivity using both InSiL-MOLLI (remote 3.08 ± 1.70%, ischemic 1.65 ± 0.72%, p<0.001) and SASHA (remote 2.76 ± 1.43%, ischemic 1.63 ± 0.54%, p=0.023). Similarly, there was a significant difference between FE T1 reactivity in remote and ischemic regions using InSiL-MOLLI (remote -10.43 ± 3.69%, ischemic -3.18 [-7.24, -2.53], p<0.001) and SASHA (remote -9.25 ± 2.71%, ischemic -4.68 ± 2.6%, p<0.001).

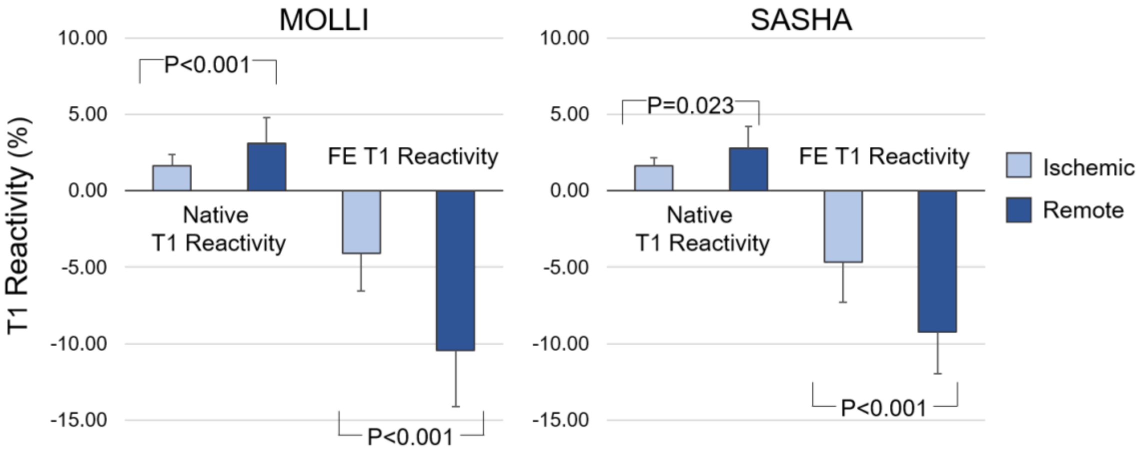

Figure 4.3. Native and ferumoxytol-enhanced (FE) T1 reactivity in remote and ischemic myocardium at 3.0T.

Table 4.1 summarizes the mean native and FE T1 reactivity for remote and ischemic myocardial regions. In swine subjects that underwent repeated cycles of FE T1 stress testing immediately following implant deployment, we found no significant relationship between FE T1 reactivity and time from implant deployment in both ischemic (p=0.397) and remote (p=0.581) myocardium.

Table 4.1. Native and ferumoxytol-enhanced (FE) myocardial T1 reactivity at 3.0T. * Denotes remote T1 reactivity values that are significantly different from ischemic T1 reactivity ($p<0.05$ on paired t-test or Wilcoxon rank-sum test). Mean ± standard deviation; median (IQR).

T1 reactivity (%)

Native	InSiL-MOLLI	MOLLI-MOLLI	SASHA
Ischemic	1.65 ± 0.72	1.64 ± 2.06	1.63 ± 0.54
Remote	3.08 ± 1.70*	2.80 (1.73, 6.20)*	2.76 ± 1.43*
FE			
Ischemic	-3.18 (-7.24, -2.53)	-4.41 ± 2.61	-4.68 ± 2.64
Remote	-10.43 ± 3.69*	-9.15 ± 5.36*	-9.25 ± 2.71*

Receiver operating characteristics of native and ferumoxytol-enhanced T1 reactivity

Figure 4.4 shows the ROCs for native and FE InSiL-MOLLI-derived T1 reactivity of 12 swine subjects with at least moderate acute focal coronary stenosis in the LAD territory. The AUC for FE MOLLI T1 reactivity is higher relative to native MOLLI T1 reactivity (native AUC: 0.717, 95% CI 0.555-0.846; FE AUC: 0.915, 95% CI 0.786-0.979; P=0.036). Relative to native MOLLI-derived T1 reactivity, FE MOLLI-derived T1 reactivity had a two-fold larger effect size for prediction of RWMAs (native T1 reactivity effect size 0.84, 95% CI 0.18-1.30; FE T1 reactivity effect size 1.71, 95% CI 1.08-2.36). A native MOLLI-derived T1 reactivity threshold of 1.69% had 73.3% sensitivity and 76.9% specificity for prediction of RWMAs. A FE MOLLI-derived T1 reactivity threshold of -4.65% had 73.3% sensitivity and 96.2% specificity.

In the set of 8 subjects that underwent both MOLLI and SASHA imaging, native and FE SASHA T1 reactivity did not show significantly different AUC (native AUC: 0.788, 95%CI 0.611-0.910; FE AUC: 0.905, 95% CI 0.751-0.979; P=0.209). However, the effect sizes for

SASHA-derived T1 reactivity were comparable to those of native and FE MOLLI T1 reactivity. The finding that effect size is larger with ferumoxytol-enhancement relative to native T1 reactivity remains consistent regardless of pulse sequence choice (native SASHA-derived T1 reactivity effect size 0.79, 95% CI 0.22-1.26; FE SASHA-derived T1 reactivity effect size 1.69, 95% CI 0.80-2.61). A native SASHA-derived T1 reactivity threshold of 2.19% showed a sensitivity of 91.75% and specificity of 66.7% for prediction of RWMAs. A FE SASHA-derived T1 reactivity threshold of -5.25% had a 75.0% sensitivity and 95.2% specificity for prediction of RWMAs.

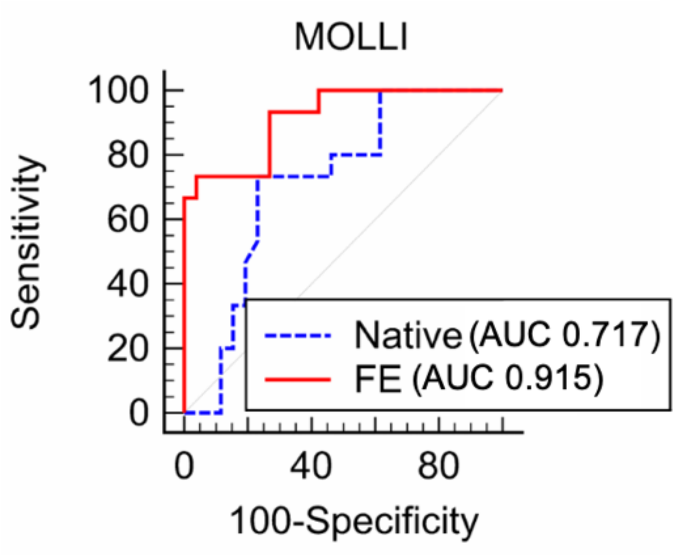

Figure 4.4. Receiver operating characteristic (ROC) curves of native and ferumoxytol-enhanced (FE) T1 reactivity for prediction of regional wall motion abnormalities as a proxy for tissue hypoperfusion.

4.4 Discussion

Our results indicate that vasodilator stress FE T1 mapping has favorable diagnostic performance relative to native T1 mapping for quantitative differentiation between regions of ischemic and remote myocardium using pixelwise T1 reactivity maps. Relative to SASHA T1 mapping, InSiL-MOLLI yielded images with a lower average artifact score and fewer rejected segments.

A prior study using adenosine (140 μg/kg/min) stress testing study at 1.5 T in humans found an average MOLLI T1 reactivity of 4.3 ± 2.8% in normal controls, 2.6 ± 3.4% in remote myocardium and 0.2 ± 0.7% in ischemic myocardium using gadolinium first pass perfusion imaging as reference.[105] A subsequent study found a median MOLLI T1 reactivity of 4.15% (3.20–7.03%) in normal controls, 3.54% (1.48–5.78%) in remote and 0.00% (− 0.18 to 0.16%) in ischemic myocardium.[36] A study at 3.0T in humans found T1 reactivity values of 6.2 ± 0.5% in normal controls, 3.9 ± 0.6% in remote, and 0.2 ± 0.8% in ischemic myocardium (ShMOLLI; adenosine: 140-210 μg/kg/min, 3-6 min).[106] Our native InSiL-MOLLI studies at 3.0T in swine found a T1 reactivity of 3.08 ± 1.70% in remote and 1.65 ± 0.72% in ischemic myocardial regions. The mean native T1 reactivity in ischemic regions of our swine models is greater than values typically reported in humans. This may reflect differences in the severity of coronary stenosis induced by our implants relative to the severity of coronary stenosis in human patients for published studies, as well as our use of an acute, rather than chronic, model of myocardial hypoperfusion. This difference in ischemic T1 reactivity may also stem from differences in the method used to identify and contour regions of ischemic myocardium. While RWMAs on cine imaging show high specificity for myocardial hypoperfusion, this technique is not used for direct quantification of myocardial perfusion on a pixelwise basis.

Recent publications investigating T1 reactivity as a biomarker for myocardial ischemia or infarction have used gadolinium-enhanced first pass perfusion and late gadolinium enhancement (LGE) to contour and classify myocardium as remote, ischemic or infarcted.[36,105,107] We identified ischemic myocardial regions based on assessment of RWMAs, which is highly specific for stunned and hypoperfused myocardium (e.g. dobutamine stress echocardiography relies on the detection of RWMAs as surrogate for dobutamine-induced ischemia). A recent study at 3.0T in patients on hemodialysis reported a mean native T1 reactivity of 3.01% in regions with normal wall motion and 1.6% in hypokinetic regions (MOLLI; adenosine: 140-210 µg/kg/min, 3 mins).[108] The results in the latter study are descriptive, and the presence of advanced kidney disease in this patient population limits direct comparison of the native T1 reactivity, which may be affected by underlying microvascular dysfunction. However, the results support the use of wall motion to distinguish between normal and pathologic myocardial tissue and demonstrate applicability at a comparable magnet strength used in our study.

Previously published feasibility data on FE T1 reactivity using MOLLI in swine models found a mean FE T1 reactivity of -7.2 ± 0.7% in ischemic myocardium and -15.7 ± 1.7% in remote myocardium at 3.0T.[19] The present study found a mean FE T1 reactivity of -3.18 (-7.24, -2.53)% in ischemic myocardial regions and -10.43 ± 3.69% in remote regions. The greater variability of T1 reactivity in the present study may be due to a greater variation in the degree of ischemia in our swine models, adenosine infusion dosage, and the technique employed to create focal coronary stenosis. Our 3D printed implants had a range of stenosis severity on angiographic images. Another recent study in patients with coronary disease found that native T1 reactivity can distinguish between remote, ischemic, and infarcted myocardium.[36] The ROC curves of native and FE MOLLI T1 reactivity for prediction of RWMAs indicate that ferumoxytol increases the dynamic range of T1 reactivity as a measure of myocardial vasodilator response (native AUC: 0.717, 95% CI 0.555-0.846; FE AUC: 0.915, 95% CI 0.786-0.979; P=0.036). While the 95% CIs of these results indicate that further confirmation is needed prior to clinical adoption, the increased dynamic range of FE T1 reactivity may be helpful in clinical practice where additional confounding factors may be present.

The results of this study do not demonstrate a significant advantage to using InSiL-fitted bSSFP-MOLLI over SASHA for the assessment of myocardial ischemia. However, in the absence of such results it is still necessary for researchers to choose the most appropriate pulse sequence for the clinical application. The bSSFP-MOLLI T1 mapping sequence used in this study has several well-documented advantages over other sequences, most notable is its precision and reproducibility. MOLLI typically demonstrates less absolute accuracy than saturation recovery sequences like SASHA and SAPPHIRE.[35] However, T1 reactivity is a measure of relative change in T1 between baseline and vasodilator stress states, and absolute accuracy of raw T1 measurements in the setting of stress testing does not necessarily translate to meaningful improvement in clinical utility. As a result, greater precision should likely be valued over absolute accuracy in measured T1 for stress testing applications. Overall, our data support a favorable diagnostic profile for FE T1 reactivity relative to native T1 reactivity when using 5(3)3(3)3 MOLLI with InSiL T1 fitting.

This study has several limitations. Our swine model reflects artificially induced acute tissue hypoperfusion rather than a model of chronic stable coronary stenosis. Confirmation in patient studies with chronic stable ischemic coronary disease will be needed. Second, visual assessment of coronary stenoses using X-ray angiography showed some heterogeneity in the degree of coronary narrowing. As a result, our ischemic T1 reactivity data likely encompasses a range of ischemic severity. RWMAs are known to indicate myocardial hypoperfusion and the onset of myocardial stunning, RWMAs do not directly reflect the state of tissue perfusion, but have been shown to have high specificity as a proxy for clinically relevant obstructive coronary disease.[100] As a result, our analyses of T1 reactivity maps have direct relationship with RWMAs and indirect relationship with tissue hypoperfusion. Additionally, known sources of measurement variation in T1 mapping will affect the results of T1 reactivity measurements. In addition to the heart rate dependence of myocardial T1, which we mitigate with the use of InSiL T1 fitting, T1 reactivity measurements can also be impacted by noise in T1 maps and test-retest variability in myocardial T1. By sensitizing the myocardial T1 to adenosine stress and increasing the dynamic range of myocardial T1 reactivity, ferumoxytol enhancement may help to minimize the impact of these sources of inherent measurement variability in T1 stress testing, improving the sensitivity and specificity of the technique. Last, although our technique demonstrates favorable quantitative diagnostic performance for FE T1 reactivity as an imaging biomarker, our FE T1 reactivity maps do not show qualitative conspicuity of ischemic segments on visual inspection. The use of ferumoxytol is not without risks and has several well-documented disadvantages. First, ferumoxytol, as an intravenous iron medication, can in rare cases induce serious hypersensitivity reactions. However, a multi-center safety study of 3215 patients found off-label diagnostic use of ferumoxytol to be associated with no serious adverse events.[10] Although ferumoxytol's long intravascular half-life is advantageous for steady-state imaging exams and delayed imaging in some cases of inflammatory disease, its long half-life can alter the MR signal for weeks to months following administration. Radiologists should be informed of its recent use when interpreting subsequent images.

4.5 Conclusion

Future investigations on FE T1 mapping to depict regions of myocardial hypoperfusion and ischemia should address whether the diagnostic benefits of stress testing can be obtained solely with peak stress T1 mapping alone and without baseline imaging. Likewise, future work should address whether changes in MBV due to hypoperfusion can be identified with baseline native and FE T1 mapping, which could potentially eliminate the need for pharmacologic stress. Ferumoxytol contrast increases the dynamic range of T1 reactivity as a biomarker for myocardial hypoperfusion in adenosine stress T1 mapping studies. Our results indicate that ferumoxytol may also increase the AUC and effect size of T1 reactivity as a measure of myocardial ischemia (defined by RWMAs), improving its diagnostic performance relative to native T1 reactivity.

Additional confirmation is needed to determine whether an advantage exists to using MOLLI or SASHA for T1 reactivity quantification. Pixel-wise T1 reactivity maps computed from FE rest and stress T1 maps show early promise as a means of distinguishing ischemic from remote myocardial tissues in large animal models of acute myocardial hypoperfusion.

Chapter 5 A tissue compartmental model of intramyocardial blood volume and water exchange in healthy swine models

5.1 Introduction

Fractional myocardial blood volume (fMBV) provides insight into myocardial ischemia severity beyond that provided by myocardial blood flow (MBF) alone.[22,43] Multi-compartmental modelling can be used to quantify fMBV from contrast-enhanced cardiac MRI.[44,45] Of these models, two-compartment strategies have been used to describe the effect of contrast agents and vascular water exchange on MR signal intensity in the myocardium.[44] One major challenge for measurement of fMBV in 2-compartment models however, is the intravascular fidelity and corresponding kinetics of the contrast agent. Thus, exploiting contrast agents with true intravascular properties for fMBV studies is an obvious choice because they eliminate the need to model contrast leakage into the extravascular space.[38,39] Ferumoxytol's long intravascular half-life (10-14 hours) and high R1 relaxivity (9.5 s^{-1} mM^{-1} at 3.0T in human plasma at 37°C)[7,8] make it an ideal intravascular contrast agent for estimating fMBV. However, it is only marketed in the United State and is its diagnostic use is off label.

We hypothesized that ferumoxytol-enhanced (FE) T1 MRI using a multi-dose sampling scheme could be combined with a two-compartment model to quantify fMBV as a proxy for myocardial perfusion. Consequently, the aim of this study was to derive and test a two-compartment, water exchange model based on FE-MRI for fMBV quantification and to compare it to other proposed T1 MRI proxies of blood volume estimation. We also aimed to define an optimal ferumoxytol dosing and sampling scheme needed to quantify fMBV, and to show in a swine model with coronary stenosis that fMBV differentiates hypoperfused and perfused myocardium.

5.2 Methods

Image Acquisition

To determine the time to steady-state distribution of ferumoxytol in vivo, in a preliminary study in two separate healthy, normal swine subjects, we sequentially measured mid-ventricular myocardial and LV blood pool T1 once per minute following ferumoxytol infusion (4mg/kg). T1 maps using the 5(3)3(3)3 MOLLI sequence[109] with a balanced steady-state free precession (bSSFP) readout were acquired: [FOV = 240 x 300 mm, matrix size = 384 x 308, TR = 2.6 ms, TE = 1.08 ms, slice thickness = 8 mm, pixel bandwidth = 1085 Hz, flip angle = 35˚, TI = 100 – 180 ms].

Ten 22-46 kg, adult male Yorkshire swine (S&S Farms, Ramona, CA) were included in the main study. For the core experiments in this paper, after anesthesia alone (N=9) or anesthesia and coronary implant deployment[17,18] (N=1), we transferred the swine subjects to a whole body clinical 3.0 T magnet (Prisma®, Siemens Medical Solutions USA, Malvern, PA) equipped with phased-array coils. Following localizers, we performed a ferumoxytol multi-dose T1 mapping study (Figure 1.2). We acquired non-contrast short-axis T1 maps using the 5(3)3(3)3 Modified Look-Locker Inversion (MOLLI) recovery sequence[109] with a balanced steady-state free precession (bSSFP) readout in the mid left ventricle in all healthy, normal swine (N=9), and in the left ventricular apex in the single instrumented swine model (N=1) [FOV = 240 x 300 mm, matrix size = 384 x 308, TR = 2.6 ms, TE = 1.08 ms, slice thickness = 8 mm, pixel bandwidth = 1085 Hz, flip angle = 35˚, TI = 100 – 180 ms]. After native imaging, we administered a cumulative ferumoxytol dose of 4.0 mg/kg over multiple infusions (cumulative dose 0.25, 0.5, 1.0, 2.0, 3.0 and 4.0 mg/kg, 20-fold dilution) at a rate of 0.33 mg/kg/min. Informed by results from our preliminary work on time to steady-state distribution of ferumoxytol in vivo, we observed a five-minute delay following each incremental ferumoxytol dose prior to T1 MRI to ensure contrast steady state. The MOLLI T1 mapping pulse sequence was repeated in the same short-axis slice after a five-minute delay following each dose of ferumoxytol (FOV = 240 x 300 mm, matrix size = 384 x 308, TR = 2.6 ms, TE = 1.08 ms, slice thickness = 8 mm, pixel bandwidth = 1085 Hz, flip angle = 35˚, TI = 100 – 180 ms). Following a preliminary analysis, we added an additional dose at 0.125 mg/kg in the latter four swine subjects to sample the low-dose range more densely. The typical total duration of the ferumoxytol multi-dose imaging study was approximately 55 minutes. For all FE T1 acquisitions following the initial native T1 acquisition, we used a MOLLI sequence with inversion times optimized for shorter post-contrast T1 relaxation time. After imaging, healthy normal swine subjects were transferred to an invasive protocol.

Image Processing

We used the Instantaneous Signal Loss simulation (InSiL) algorithm with an inversion factor of 96% for T1 fitting of MOLLI images in order to minimize T1 error at high heart rates (>80 bpm).[33] Using commercially available software (Osirix, Pixmeo, Bernex, Switzerland), we contoured and segmented each mid-ventricular MOLLI InSiL-fitted T1 map into six segments based on the AHA 17-segment model, and excluded segments with severe artifacts (CMC, 3 years cardiovascular MRI experience; contours confirmed by KLN, >9 years cardiovascular MRI experience).[99] We contoured a central region of the mid-LV blood pool with careful attention to exclusion of trabeculation and papillary muscles. In raw images with visible motion artifacts, we manually fitted myocardial segmental T1 using InSiL. We exported segmental myocardial ferumoxytol ($R1_{myo}$, $R1_i$) curves to MATLAB (MathWorks, Natick, MA) for fMBV modelling.

We estimated $R1_e$ as described above and fitted fMBV, k_i and λ for the whole myocardium and for each myocardial segment for all subjects.

We used the two-compartment water exchange model to generate pixel-wise fMBV maps of one healthy swine and one swine with artificially induced myocardial hypoperfusion. To capture the full extent of myocardial hypoperfusion downstream from the intracoronary stenosis implant, fMBV was measured in the left ventricular apex in the instrumented swine model. Prior to fMBV fitting, we co-registered the set of eight InSiL T1 maps generated at each cumulative ferumoxytol dose (0-4.0 mg/kg) using a groupwise image registration method designed for parametric mapping applications in Elastix (5.0.0).[58,98] Using the $R1_i$ and $R1_e$ derived from segmental data, we computed fMBV and intravascular water exchange for each pixel using a three-parameter fit. We segmented the pixel-wise fMBV maps into 6 segments (normal swine subject, mid slice) and 4 segments (instrumented swine subject, apical slice) respectively, based on the AHA 17-segment model.

Comparison of fMBV to Other Proxies of Blood Volume Estimation and Identification of an Optimized Ferumoxytol Dosing and Sampling Scheme

Due in part to the long exam time required for performance of a multi-dose T1 acquisition, several simplified surrogates of blood volume have been proposed. We evaluated fast-exchange fMBV (equation 1-2) in nine normal swine subjects to assess its agreement with our model-fitted fMBV. R1 subtraction maps have also been proposed as a substitute for model-fitted blood volume because change in tissue R1 is related to local blood volume fraction.[110] We evaluated the percent increase in myocardial R1, ($\frac{R1_{post\,ferumoxytol}-R1_{pre\,ferumoxytol}}{R1_{pre\,ferumoxytol}}$), following a cumulative ferumoxytol infusion of 4.0 mg/kg.

To optimize the number of ferumoxytol infusions necessary for accurate quantification of fMBV using the two-compartment model, we evaluated segmental fMBV in four swine subjects using various dose under-sampling schemes with three parameter fitting. Each under-sampled scheme used four doses out of the complete set of eight that were acquired. In order to capture the full range of the ($R1_{myo,}$ $R1_i$) curve, each four-dose scheme included the minimum and maximum ferumoxytol dose (0.0 and 4.0 mg/kg), with two additional doses in the intermediate range (0.125 to 3.0 mg/kg).

Statistical Analysis

We used the Kolmogorov-Smirnov test to assess data normality. Normally distributed data are represented as mean ± standard deviation (SD). Following contouring of myocardial T1 maps in accordance with the AHA 17-segment model and fitting of fMBV, we used one-way analysis of variance (ANOVA) to assess variation in fMBV between subjects and between myocardial segments. We generated Bland-Altman plots to assess agreement of image-derived and model-fitted $T1_e$. We assessed the agreement between 1) fast-exchange fMBV (equation 1-2) and our model-fitted fMBV estimates; and 2) fMBV fitted to under-sampled (4 doses) curves relative to our fully sampled (8 doses), model-fitted fMBV. We used Pearson R-correlation to determine the relationship between fMBV and percent-increase in myocardial R1. We performed statistical analyses in MATLAB and MedCalc (v19.0.5, MedCalc Software, Ostend, Belgium). A p value < 0.05 was considered statistically significant.

5.3 Results

Ferumoxytol Dose-Response of LV Blood Pool and Myocardial T1

Myocardial and LV blood pool T1 reached steady state within three to four minutes following ferumoxytol infusion in a preliminary study in two swine subjects. Ferumoxytol dose-response of myocardial and blood pool T1 is summarized in Figure 5.1. Prior to ferumoxytol infusion, the myocardium and LV blood pool at 3.0T showed a mean native T1 of 1389 ± 23 ms and 1846 ± 73 ms, respectively. Mean myocardial and LV blood pool T1 decreased monotonically with increasing ferumoxytol dose. The multi-dose T1 imaging study captured the inversion of contrast between the myocardium and LV blood pool between 0.125 mg/kg and 0.25 mg/kg of ferumoxytol. Following the cumulative infusion of 4.0 mg/kg, we found a steady state mean myocardial and blood pool T1 of 832 ± 26 ms and 115 ± 10 ms, respectively. No ferumoxytol-related adverse events occurred, and vital signs were stable throughout the course of the exams.

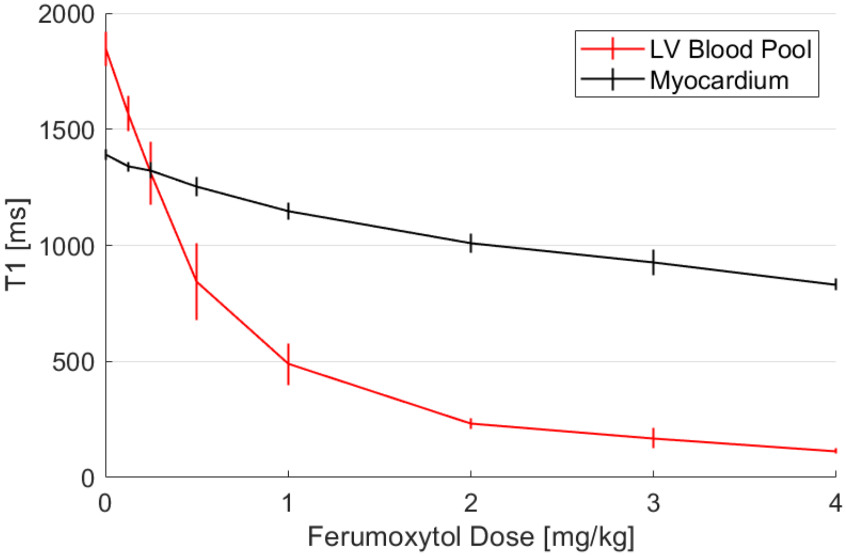

Figure 5.1. Ferumoxytol dose-response curves for left ventricular (LV) blood pool and myocardial T1. T1 (ms) is plotted as mean ± sd.

Image-Derived and Model-Fitted Extravascular T1

We found a mean image derived extravascular T1 of 1328 ± 35 ms and a mean model-fitted extravascular T1 of 1331 ± 27 ms. The mean percent-difference between the two extravascular T1 estimates across all subjects was 0.28 ± 0.95%. Bland-Altman analysis found no significant bias (p=0.409, n=9) and limits of agreement (LOA) of -20.9 ms [95% CI -38.0, -3.79 ms] to 28.2 [11.07, 45.30 ms].

Segmental fMBV and Water Exchange

We quantified segmental fMBV and water exchange in the mid-ventricular myocardium of all swine subjects using a two-compartment model with three-parameter curve fitting and image-derived extravascular T1. The constrained nonlinear multivariable optimization solver was able to converge to a solution for all segments in all subjects. Model-generated ($R1_{myo,}$ $R1_i$) curves fit the imaging data well, with a median R^2 of 0.997 (IQR 0.992 – 0.998; range 0.919 – 1.000). We found a mean mid-ventricular fMBV of 7.2 ± 1.4% and a mean intravascular water exchange rate of 11.3 ± 5.1 s^{-1}. These results are presented alongside the results of similar published methods in Table 5.1.

Table 5.1. Comparison of steady-state contrast-enhanced multi-compartmental models of myocardial blood volume and water exchange using iron-based contrast agents. fMBV and ki reproduced as reported or computed from reported model parameters and results. *Wacker et al. report fMBV, water exchange fitted to complete (N=6) dataset. fMBV, fractional myocardial blood volume; ki, intravascular water exchange rate.

Study	Subject	Contrast	T1 sequence	Field strength	Model	fMBV (%)	k_i (s^{-1})
Wacker et al. (2002)[111]	Human, CAD (6)	NC100150	Saturation-recovery turboFLASH	1.5 T	2-compartment, model-fitted	12.9*	3.72
Bjornerud et al. (2003)[49]	Swine, Healthy (8)	NC100150	Look-Locker	1.5 T	2-compartment, model-fitted	12.4± 2.3	9.35± 5.5
Bane et al. (2015)[47]	Canine, Healthy (1)	Ferumoxytol	5(3)3(3)3 MOLLI	1.5 T	2-compartment, slow exchange	5	14
Colbert et al.	Swine, Healthy (9)	Ferumoxytol	5(3)3(3)3 MOLLI	3.0 T	2-compartment, model-fitted	7.2 ± 1.4	11.3± 5.1

One-way ANOVA across nine healthy swine subjects showed significant variance in global fMBV between subjects (7.95 ± 2.00%, 7.25 ± 2.92%, 8.07 ± 1.38%, 9.59 ± 2.21%, 7.80 ± 1.44%, 5.93 ± 1.43%, 6.84 ± 0.65%, 5.78 ± 2.05%, 8.31 ± 1.94%; $p < 0.05$), indicating that individual normal swine subjects can present with slightly different baseline fMBV. We performed one-way ANOVA across the six mid-ventricular myocardial segments in this population of normal swine subjects to evaluate whether an underlying pattern of variation in fMBV existed among coronary territories. One-way ANOVA showed no significant variance in fMBV across the six mid-ventricular coronary territories (8.60 ± 2.95% [anterior], 7.61 ± 2.56% [anteroseptal], 6.91 ± 1.80% [inferoseptal], 7.74 ± 1.85% [inferior], 6.84 ± 1.49% [inferolateral], 7.30 ± 1.43% [anterolateral]; p=0.387). Figure 5.2 summarizes fMBV across the mid myocardial segments in the nine healthy swine subjects. There was no significant correlation between global fMBV and total body mass across all subjects (p=0.117).

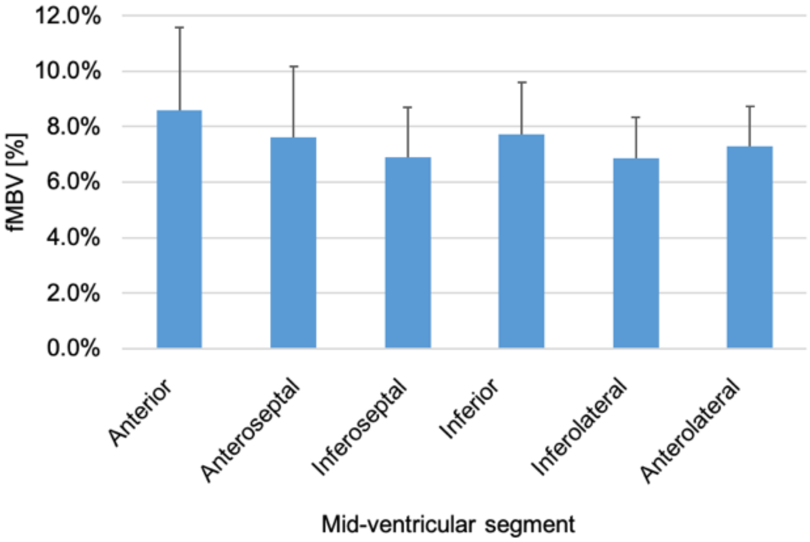

Figure 5.2. Segmental fMBV in nine healthy swine models (mean ± SD). One-way ANOVA shows significant variance in baseline fMBV between swine subjects (p=0.027), and no significant variance in fMBV between segments (p=0.387).

Comparison of Model-Fitted fMBV to Other Proxies of Blood Volume Estimation

Fast-exchange fMBV computed at 2.0 mg/kg ferumoxytol showed the best nominal agreement with model-fitted fMBV. Linear regression analysis showed a moderate correlation between fast-exchange fMBV at 2.0 mg/kg and model-fitted fMBV (r = 0.71, p <0.05). Bland-Altman analysis of the fast-exchange vs model fitted fMBV found LOA of -2.60% [-3.29, -1.92%] to 2.76% [2.08, 3.45%] without significant bias (mean difference=0.08, p=0.688, Figure 5.3). Linear regression also showed a significant, but poor correlation between percent-change in R1 following ferumoxytol infusion of 4.0 mg/kg and model-fitted fMBV (r=0.50, p <0.05).

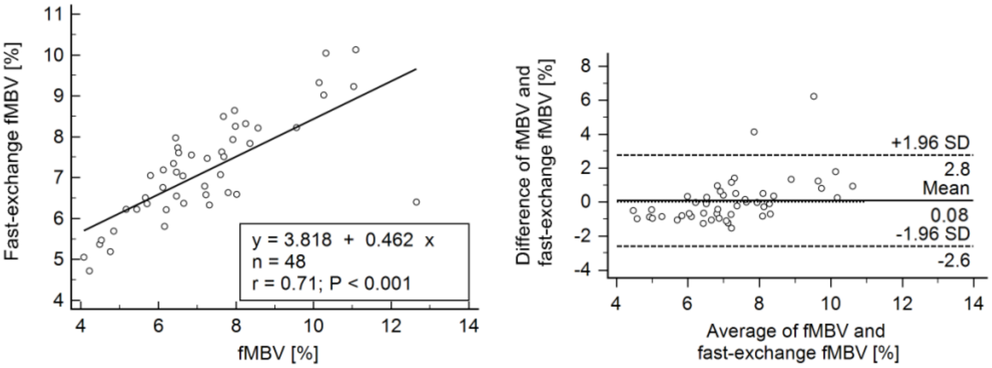

Figure 5.3. Bland-Altman analysis of model-fitted and simple fast-exchange fMBV at 2.0 mg/kg ferumoxytol. The mean difference is 0.08 (p=0.688). Wide limits of agreement may obscure subtle findings in the clinical setting if a simple fast-exchange approach is used.

Optimized Sampling Scheme and Ferumoxytol Dosing for fMBV Quantification

The optimal dosing scheme that maximized the agreement of fMBV derived from the under-sampled and the complete dataset was 0.0, 0.125, 2.0, and 4.0 mg/kg ferumoxytol. Linear regression analysis showed significant and strong positive correlation between fMBV estimates from the under-sampled and the complete dataset (r=0.95, p <0.05). Bland-Altman analysis of under-sampled relative to the complete dataset for fMBV showed LOA of -1.04% [-1.45, -0.62%] to 1.18% [0.77, 1.59%] without significant bias (mean difference=0.07, p=0.541, Figure

5.4). When extravascular T1 was fitted as a model parameter in both the complete and under-sampled datasets, the same dose under-sampling scheme showed a strong correlation (r=0.97, p <0.05), no significant bias (mean difference=0.19, p=0.08), and fMBV LOA of -0.80% [-1.16, -0.43%] to 1.17% [0.80, 1.53%].

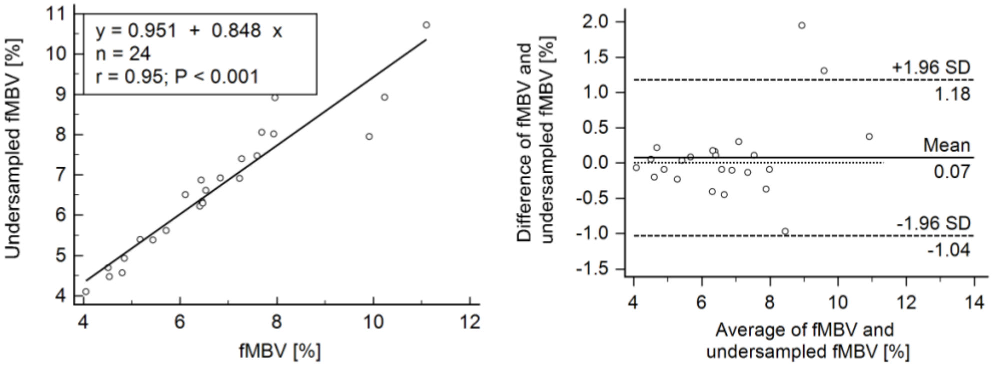

Figure 5.4. Bland-Altman analysis of fMBV in 4 swine subjects fitted using the complete dataset and an undersampled dataset of 4 ferumoxytol doses (0.0, 0.125, 2.0, 4.0 mg/kg). The mean difference is 0.07 (p=0.541).

Pixel-Wise Myocardial Blood Volume

We used our two-compartment water exchange model to generate pixel-wise fMBV maps for a swine subject with myocardial hypoperfusion in the mid to distal LAD coronary territory, as well as a single healthy, normal swine subject (Figure 5.5). Pixel-wise fMBV for each myocardial segment is reported in Table 5.2. In the swine with artificially-induced stenosis of the LAD, we found a mean pixelwise fMBV of 11.90 ± 4.00%, 16.10 ± 5.71%, 9.59 ± 3.35%, and 9.38 ± 2.35% in the anterior, septal, inferior and lateral segments respectively. Quantitative pixel-wise fMBV showed regional differences in hypoperfused relative to perfused segments. When fMBV is plotted on colorized maps as in Figure 5.5, this difference is readily visible in the segments that are hypoperfused by the stenotic LAD.

Table 5.2. Pixel-wise fMBV values in a swine model of myocardial hypoperfusion and a normal swine subject. *Segments perfused by the artificially induced left anterior descending artery coronary stenosis.

Swine subject with myocardial hypoperfusion

Myocardial Segment	fMBV (%)	Water exchange rate (1/s)
13 (apical anterior)*	11.90 ± 4.00	4.54 ± 1.89
14 (apical septum)*	16.10 ± 5.71	3.57 ± 2.11
15 (apical inferior)	9.59 ± 3.35	5.55 ± 3.68
16 (apical lateral)	8.38 ± 2.35	5.53 ± 2.90

Normal swine subject

Myocardial Segment	fMBV (%)	Water exchange rate (1/s)
7 (mid anterior)	7.74 ± 1.70	11.29 ± 4.18
8 (mid anteroseptal)	8.36 ± 2.86	9.75 ± 3.85
9 (mid inferoseptal	7.83 ± 1.17	10.16 ± 3.95
10 (mid inferior)	8.13 ± 2.51	10.17 ± 5.38
11 (mid inferolateral)	7.33 ± 2.06	18.30 ± 12.90
12 (mid anterolateral)	7.10 ± 1.16	11.78 ± 3.35

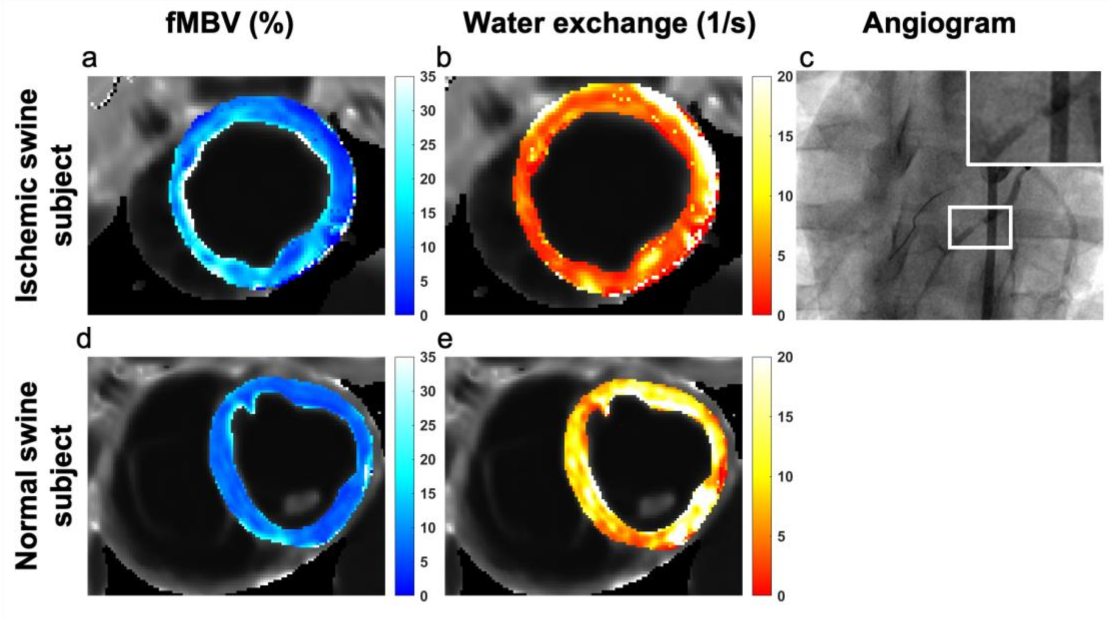

Figure 5.5. Illustrative examples of pixelwise fMBV and water exchange maps in a swine model of regional myocardial hypoperfusion (a, b) and a normal swine subject (d, e). Angiographic image (c) acquired following deployment of a 3D-printed coronary implant in the mid LAD shows severe coronary narrowing.

5.4 Discussion

Our study demonstrated the feasibility of fMBV quantification from FE-MRI using a two-compartment water exchange model with three-parameter curve fitting in nine healthy, normal swine subjects and a single swine with artificially-induced coronary stenosis. We showed that extravascular T1 can be derived directly from imaging data to simplify the model. Although simple linear interpolation of extravascular T1 from imaging data ignores the effect of water exchange on extravascular T1, an assumption that we avoided elsewhere in our fMBV model, we have shown empirically that extravascular T1 values extracted directly from imaging data match closely with values derived from four-parameter curve fitting. To further facilitate clinical translation of the proposed work, we also identified a sparser dose sampling scheme that maintained the accuracy of fMBV estimates. These findings have important clinical implications for the characterization of tissue perfusion.

Several other approaches have been proposed to estimate fMBV, including simple fast-exchange fMBV (equation 1-2) and percent change in R1 (pre and post contrast). Although our calculations showed good correlation between simple fast-exchange fMBV and model-fitted fMBV, Bland-Altman analysis showed wide limits of agreement which may obscure subtle changes in regional myocardial hypoperfusion. On the other hand, percent change in R1 following 4 mg/kg ferumoxytol showed a weaker correlation with model-fitted fMBV and is likely to be least useful clinically. In the clinical setting, where patients frequently present with multi-vessel disease, we expect to observe a wide degree of heterogeneity in ischemia severity across myocardial segments within individual patients. We also expect a greater incidence of respiratory motion artifacts. As a result, a relatively sensitive imaging biomarker is desired. While the fast-exchange fMBV approach and the percent change in R1 methods are simple, they are less promising as reliable surrogates for fMBV. Further comparisons should be made in the clinical setting, where disease is more nuanced, to confirm our hypothesis.

Little has been published about the minimum number of contrast doses needed to accurately model fMBV, and published studies employ a range of sampling schemes.[48,49,111] Among the under-sampling schemes tested, the (0.0, 0.125, 2.0, and 4.0 mg/kg ferumoxytol) scheme showed closest agreement with the fully-sampled scheme. When compared to the difference in fMBV between perfused and hypoperfused myocardial segments in a single instrumented swine model, the small limits of agreement with this scheme suggested that differentiation of regional myocardial hypoperfusion using model-fitted fMBV may be feasible with four T1 acquisitions rather than eight. This dose sampling scheme would reduce the total study time to approximately 35 minutes – comparable to the duration of a typical stress perfusion MRI study. These results are promising, as long exam times and complex acquisition protocols can deter clinical adoption of new imaging approaches.

Multi-compartmental modelling with intravascular contrast agents has been used to investigate fMBV in healthy volunteers, patients, and large animal models,[47,49,111] but data using clinically available intravascular contrast agents such as ferumoxytol are limited.[47] The published literature reflects a range of contrast agents, dosages, T1 imaging pulse sequences and fitting algorithms.[47,49,111] A comparison between our fMBV estimation and a selection of similar published methods[47,49,111] demonstrates a range of complexity for both compartmental models and acquisition protocols. Our two-compartment model is moderately complex relative to other published methods.[47,49,111] Pixel-wise mapping of fMBV using our method requires the extraction of blood and whole-myocardial R1 prior to fMBV fitting. While our imaging protocol required the acquisition of eight individual MOLLI images, our dose optimization study found that a four-dose protocol may perform comparably well.

Published fMBV values range from 5% to 12% and water exchange rates range from 8.5 to 14.2 s^{-1} in human, swine and canine studies using the iron-based intravascular contrast agents ferumoxytol and NC100150.[47,49] Our segmental fMBV and water exchange results in nine healthy swine models fall within the published ranges. McCommis et al. found an absolute MBV of 6.1 ± 0.5 mL/100g in healthy canine subjects using first pass perfusion MRI with a dendritic gadolinium-based contrast agent[112] that has intravascular properties, which correlated well with their reference MBV values derived from red blood cell radiolabeling. Differences between our fMBV values and those from McCommis et al may relate to differences in contrast agents, subject population, imaging pulse sequence, and model fitting. We employed a true intravascular indicator, ferumoxytol, which has an intravascular residence time of 10-15 hours in healthy vasculature. Most clinically available gadolinium-chelates are extracellular agents that leak into the extravascular space. Even when extravasation is taken into account during modeling,[47] the use of extracellular agents may be less desirable for steady-state fractional blood volume modelling.

Our fMBV values using a two-compartment water exchange model based on FE-MRI in a swine with a focal LAD stenosis are hypothesis-generating. We found that increased fMBV in the myocardial segment perfused by the stenosed LAD (septum) relative to remote segments. Elevated fMBV has been proposed as a compensatory response in the setting of regional myocardial hypoperfusion downstream from a significant coronary stenosis[22] and our interesting observation in a swine model with artificially-induced regional myocardial hypoperfusion complements work by McCommis et al. who measured MBV in dogs with first pass perfusion imaging.[112] Further work is underway to closely evaluate this finding.

Limitations

First, our model-fitted fMBV has been derived using data obtained with a specific intravascular contrast agent (ferumoxytol) in combination with a specific MOLLI derived T1 mapping sequence. Second, our model of fMBV was based on only nine healthy normal swine subjects and one swine with moderate to severe LAD coronary stenosis. While we obtained mean segmental fMBV within the range of published values for similar studies conducted in humans and large animals, the broad range of published contrast doses, imaging pulse sequences and fitting algorithms complicates one-to-one comparison of methodologies. Likewise, we chose to implement a two- , rather than three-compartment model, ignoring the effects of transcytolemmal water exchange. Third, while anesthesia enables high quality pixelwise fMBV mapping in this preclinical study, respiratory motion will pose a greater challenge in the clinical setting. Likewise, Baudelet et al. found that intraperitoneal ketamine (80 mg/kg) significantly reduced perfusion of skeletal muscle in a mouse liver tumor model.[113] While the ketamine dose used in our swine protocol (10 mg/kg, intramuscular) was much less, it is possible that intramuscular ketamine could result in a slight reduction in myocardial perfusion in this swine model, affecting measured fMBV. Fourth, we did not compare our model-fitted fMBV to other reference techniques. Nevertheless, our model-fitted fMBV values aligned with published values for fMBV in swine models using MRI. We evaluated our pixel-wise blood volume mapping technique in a single instrumented swine model, rather than in a clinical study, to eliminate artifacts due to respiratory motion and precisely control the degree and location of single-vessel coronary stenosis. This allowed us to directly compare fMBV in ischemic and remote myocardial regions, while ensuring the highest possible quality of T1 and fMBV maps in the proof-of-concept stage. Our preliminary observation of elevated fMBV in the myocardial territory perfused by the LAD is promising and provides very early evidence that tissue blood volume could potentially be used to discriminate between hypoperfused relative to perfused tissues.[22,47] However, these findings clearly require further study and validation. Last, while the safety profile for off-label, diagnostic use of ferumoxytol is favorable to date,[10,114,115] there remains a rare risk for severe hypersensitivity reactions associated with the use of intravenous iron agents.

5.5 Conclusion

Two-compartment modelling for estimation of fMBV is feasible using steady-state MOLLI T1 mapping over multiple doses of the clinically available iron-based intravascular agent ferumoxytol. fMBV derived from FE-MRI may have the potential to provide a unique means of assessing myocardial perfusion, particularly in settings where renal function may preclude the use of gadolinium-based agents. If confirmed in patients, model-fitted fMBV may serve as a potential direct marker of myocardial tissue perfusion.

Chapter 6 Implementation of an integrated nonrigid image registration and pixelwise fMBV mapping framework

6.1 Introduction

Elevated fMBV has been proposed as a potential biomarker for significant coronary stenosis.[24] Contrast-enhanced cardiac MRI can be combined with a tissue compartmental modelling approach to estimate myocardial transvascular water exchange in order to produce pixelwise myocardial blood volume maps.[24,57] This technique is complicated by the need for a robust and reliable image processing pipeline. The layered parametric mapping approach required to estimate fMBV compounds common technical challenges of parametric mapping. Following multiple repeated Modified Look-Locker Inversion recovery (MOLLI) acquisitions, image artifacts in any individual inversion-recovery image or T1 fitting errors in an individual MOLLI T1 map are carried forward into final fMBV map. Likewise, misregistration in either layer is carried forward into the final fMBV map. As a result, a reliable, high-quality image registration approach is essential. Prior studies have developed[58] and adapted[59] image registration models designed for physiologic parametric mapping applications with MRI. Additionally, unconstrained optimization of physiologic parameters over a three-parameter solution space results in a heavy computational burden and occasionally unstable solutions. Appropriate boundary conditions are necessary to ensure that a nonlinear optimizer can consistently converge on a solution when fitting for fMBV and other physiologic parameters. In this work, we aim to investigate potential image registration and nonlinear optimization approaches to improve the quality and reliability of fMBV maps in a cohort of healthy human volunteers and swine models with artificially induced coronary stenosis. We aim to optimize our integrated Nonrigid ImAGe Registration and pArametric (NIAGRA) mapping pipeline to minimize image noise and misregistration effects. In this study, we aim to (1) optimize a PCA-based image registration method for adaptation of blood volume mapping to a clinical study, (2) to investigate the boundary and initial conditions which minimize image noise in model-fitted fMBV maps.

6.2 Methods

Large animal studies

We induced an artificial focal coronary stenosis in the mid left anterior descending (LAD) artery of all swine using a 3D printed, heparin-coated coronary implant as previously described in five juvenile Yorkshire swine (3 female; 26 – 29 kg; Premier BioSource, Ramona, CA) .[17,18] The MRI exam was begun within 60 minutes of stenosis confirmation on x-ray fluoroscopic angiography. All swine were humanely euthanized while under general anesthesia. We transferred the swine subjects to a clinical 3.0 T magnet (Prisma®, Siemens Medical Solutions USA, Malvern, PA) with phased-array coils. Following localizers, we acquired short- and long-axis cine images using a gradient-echo sequence to assess myocardial contractility [FOV = 292 x 360 mm, matrix size = 102 x 126, TR = 5.2 ms, TE = 2.5 ms, slice thickness = 6 mm, pixel bandwidth = 450 Hz, flip angle = 12˚].

We performed a ferumoxytol multi-dose T1 mapping study in all swine (N=5). We acquired short-axis T1 maps (base, mid, apex) using the 5(3)3(3)3 MOLLI sequence[109] with a bSSFP readout [FOV = 240 x 300 mm, matrix size = 384 x 308, TR = 2.6 ms, TE = 1.08 ms, slice thickness = 8 mm, pixel bandwidth = 1085 Hz, flip angle = 35˚, TI = 100 – 180 ms]. After acquiring a set of native MOLLI T1 images, 4.0 mg/kg ferumoxytol was administered intravenously in six aliquots (cumulative dose 0.125, 0.25, 0.5, 1.0, 2.0, 3.0 and 4.0 mg/kg; infusion rate 0.33 mg/kg/min). We acquired the same set of T1 images at contrast steady state following each incremental ferumoxytol dose. The typical total duration of the ferumoxytol multi-dose imaging study was approximately 55 minutes.[57]

Human studies

We recruited five healthy human subjects (5 female, average age 33 years) for a cardiac MRI exam with feruomxytol. Subjects were imaged on a clinical 3.0 T magnet (Skyra®, Siemens Medical Solutions USA, Malvern, PA) with phased-array coils. We performed an abbreviated multi-dose T1 mapping study in all subjects (N=5). We acquired short-axis MOLLI T1 maps (base, mid, apex) at contrast steady state following a cumulative ferumoxytol dose of 0.0, 0.125, 2.0, and 4.0 mg/kg. The typical total duration of the multi-dose imaging study in human subjects was approximately 35 minutes.[57]

Image postprocessing

Figure 6.1 outlines the structure of the image postprocessing pipeline. Ferumoxytol-enhanced (FE) multi-dose images from all human and animal studies underwent T1 fitting with the InSiL algorithm, a novel T1 fitting method designed to account for the perturbation of the longitudinal magnetization due to each single-shot imaging readout in a MOLLI acquisition.[33] Prior to fMBV mapping, a binary mask was drawn to cover a conservative central region of the LV blood pool at each ferumoxytol dose. A second mask was drawn to generously cover the entire myocardium. Following groupwise image registration, the 3D transform generated by the registration algorithm was applied to the 3D volume defined by the stack of LV blood pool masks, preserving the blood pool masks' correspondence to only blood pool pixels. The transformed 3D blood pool mask was then applied to the co-registered T1 volume to extract blood pool R1 at each contrast dose. This vector $\overrightarrow{R1_v}$ serves as one of two primary inputs to the tissue compartmental model.

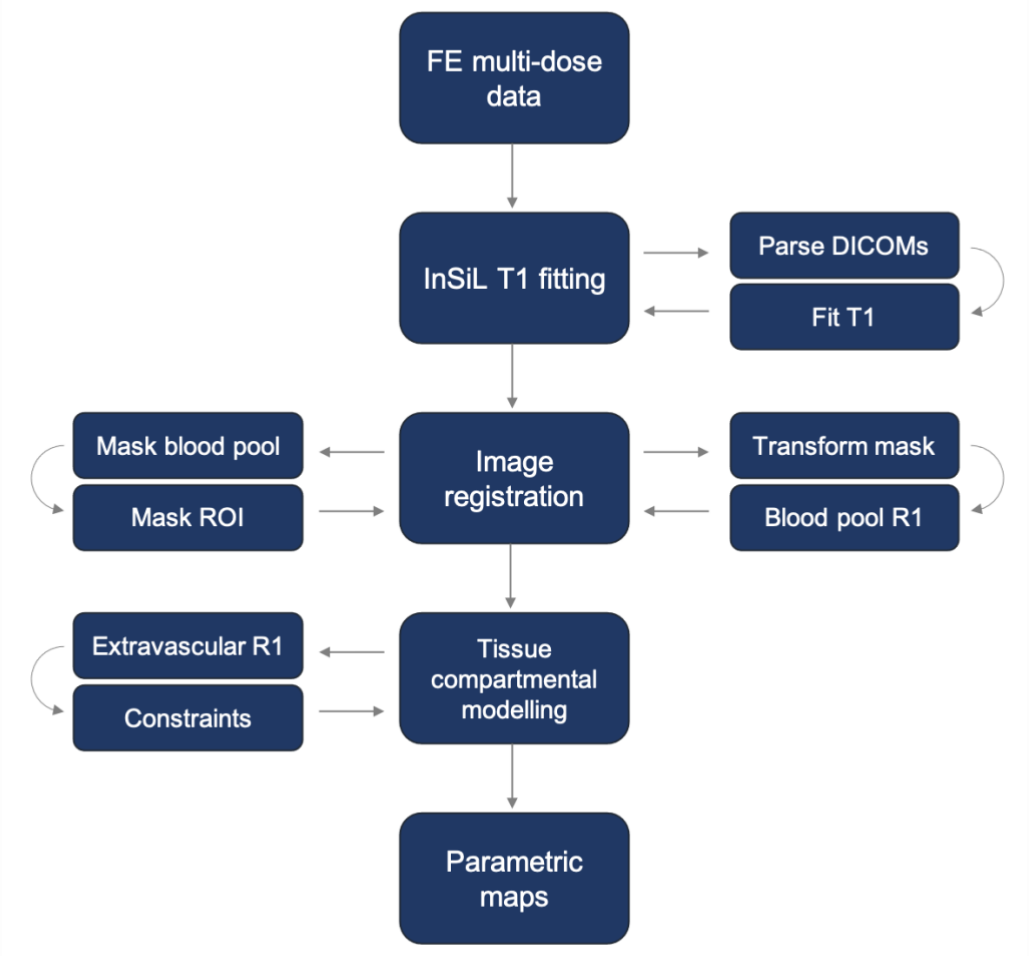

Figure 6.1. Conceptual flow of the image registration and fMBV mapping

Following T1 fitting, image registration and vascular R1 extraction, the tissue compartmental model was applied to each pixel in the imaged slice within the masked registration region. Subject to a set of pre-defined upper and lower bounds on the physiologic parameters fMBV, k_i, and λ, a nonlinear convex optimization function is used to identify the solution ($fMBV$, k_i, λ) which produces a predicted $R1_t'$ with a minimal sum-squared error relative to the measured $R1_t$. This optimization is repeated for each pixel over the masked registration region. The model-fitted matrices of estimated fMBV and water exchange rate are exported as DICOM maps for further data analysis.

Nonlinear optimizer boundary conditions

To compare the effects of optimizer boundary conditions on tissue compartmental modelling results, all human and swine datasets underwent postprocessing with two different parametric fitting schemes. We investigated the differences in fMBV produced using two sets of optimizer constraints: narrow upper and lower bounds on the water exchange rate, k_i, and partition coefficient, λ, based on published literature[24,49,111] as well as upper and lower bounds several orders of magnitude broader.

Following image registration using a principal component analysis (PCA)-based groupwise registration method designed for parametric mapping applications and implemented in Elastix, fMBV fitting was performed using a constrained nonlinear multivariable optimization solver[54] to fit for fMBV, k_i, and λ. We defined the upper and lower bounds of fMBV, k_i, and λ as [0, 100%], [2, 50 s^{-1}], and [0.5, 1] respectively. Then, we fit for fMBV again using a broader set of upper and lower bounds: [0, 100%], [1e-3, 500 s^{-1}], [1e-3, 1]. Pixelwise fMBV maps were segmented according to the AHA model.[116] We evaluated the inherent noise in the pixelwise fMBV maps by computing the percent-standard deviation: %-stdev = 100*stdev(pixelwise fMBV) / mean(pixelwise fMBV).

Registration quality analysis

Two image registration methods were used in this study. The first, a principal component analysis (PCA)-based groupwise image registration method designed for parametric mapping applications in Elastix (5.0.0),[98] co-registers quantitative MRI (qMRI) datasets by minimizing the contribution of all but the lowest-indexed eigenvalues to the signal input curve.[58] This results in a signal input curve with a variance that is primarily explained by a small number of large-value eigenvectors.[58,59] This PCA-based registration method exploits the reality that, in most cases, qMRI signal can be described by a low-dimensional model. The second, more simple linear groupwise registration method computes the sum of pair-wise correlation coefficients between the images acquired at each dose.[98]

Image registration quality was quantified using a registration quality metric designed to quantify the noise in the signal input curve represented by each pixel as follows:

$$\sum_{d=1}^{D-1} \frac{|T1_d - T1_{d+1}|}{|\overline{T1_d} - \overline{T1_{d+1}}|}$$

Where T1$_d$ represents the T1 in the pixel (*l*,*m*,*d*), and $\overline{T1_d}$ represents the mean T1 over the masked registration region at dose *d*. A greater registration quality metric represents greater noise in the signal input curve.

In addition to computing the pixel-wise registration quality metric, we measured the apparent septal myocardial width on fMBV maps fitted with and without registration. Poor co-registration of the myocardium results in an intermediate range of fMBV values along the endo- or epicardial border. One-dimensional ROIs (regions of interest) were drawn from the RV (right ventricular) blood pool to the LV (left ventricular) blood pool, crossing the epi- and endocardial borders of the myocardial septum orthogonally in the basal, mid-ventricular, and apical slices in all subjects (N=5 healthy humans; N=5 ischemic swine models). A thresholding function was used to measure the distance over which the fMBV values in each voxel along this transmural profile fell below 15% blood volume. The 15% blood volume threshold was chosen to include most myocardial pixels, while excluding blood pool pixels, as well as pixels demonstrating intermediate fMBV due to misregistration or partial volume effects. Apparent myocardial width was measured in the basal and mid-ventricular antero- and inferoseptum, and in the apical septum.

Image Analysis

Pixelwise fMBV maps were exported as DICOM images and segmented based on the AHA 17-segment model[99] using commercially available software (Osirix, Pixmeo, Bernex, Switzerland). We excluded segments with severe artifacts. One reader (CMC, 4 years cardiovascular MRI experience) assessed short axis cine images acquired in all swine models (N=5) for regional wall motion abnormalities (RWMAs) to evaluate myocardial contractile dysfunction using a 3-point Likert scale (1 = normal, 2 = hypokinetic, 3 = akinetic).[16] Myocardial segments within the LAD territory were categorized as ischemic when they showed RWMA scores of two or greater.

Statistical analysis

Data were tested for normality using the Kolmogorov-Smirnov test. Data are reported as mean ± standard deviation or median (inter-quartile range) according to normality. Bland-Altman analysis was used to test for bias and limits of agreement between the mean pixelwise fMBV in each myocardial segment following fitting with narrow and wide boundary conditions. In ischemic swine models, we used Student’s t-tests and nonparametric Mann-Whitney tests to compare fMBV between ischemic and remote myocardial regions in the same subject. Noise in pixelwise fMBV maps was compared between methods using Student’s t-tests and nonparametric Mann-Whitney tests. A repeated measures ANOVA was used to compare the mean computed image registration metric across datasets fitted with no registration, and following PCA or linear groupwise registration, and a nonparametric Friedman test was used to compare apparent myocardial septal width. A p-value <0.05 was considered statistically significant. Statistical analysis was performed using MedCalc 19.0.5 (MedCalc Software, Ostend, Belgium).

6.3 Results

No ferumoxytol-related adverse events occurred. Across N=5 healthy human subjects, one multi-dose dataset in a single slice was rejected due to significant bulk motion, and a single additional myocardial segment was rejected due to artifact. In N=5 ischemic swine models, a single myocardial segment was rejected due to artifact.

Compartmental modelling

Figure 6.2 shows an example of fMBV maps in the basal, mid-ventricular, and apical myocardium fitted with narrow (Figure 6.2 a) and wide (Figure 6.2 c) boundary conditions applied to the three model-fitted physiologic parameters. In the setting of wide boundary conditions, fMBV maps show greater noise and poorer conspicuity of the endocardial border. Following myocardial segmentation, fMBV polar maps (Figure 6.2 b, d) show the overall effect of blunted fMBV due to frequent failed optimization attempts, although with overall preservation of the distribution of fMBV within each myocardial slice.

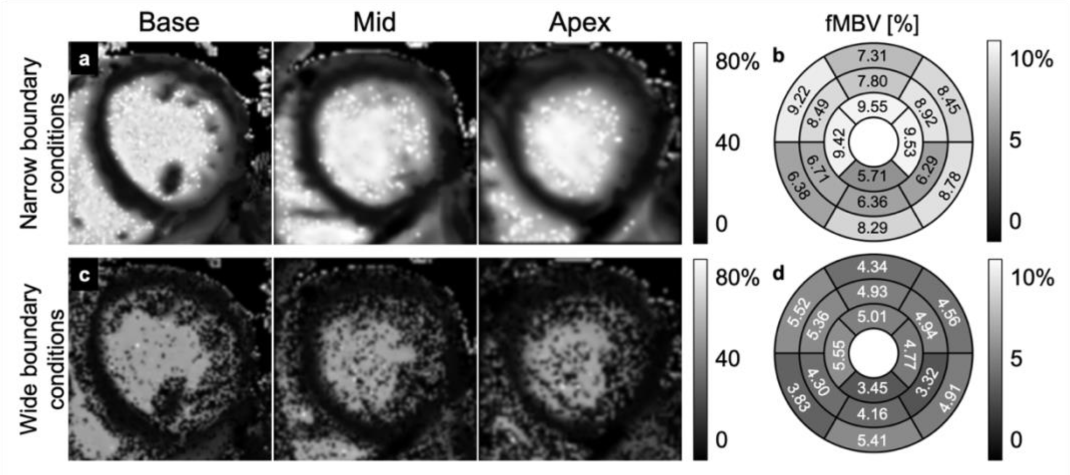

Figure 6.2. Pixelwise fMBV maps (base, mid, apex) in a single healthy human subject fitted with both narrow (a), and wide boundary conditions (b).

In N=5 healthy, normal volunteers, fMBV fitting with narrow boundary conditions produced a mean pixelwise fMBV of 8.70±1.89% across all 73 myocardial segments. Following fMBV fitting with wide boundary conditions, we found a median fMBV of 4.94% (IQR 4.18 – 5.59%). Bland-Altman analysis found a bias between the narrow and wide boundary condition methods (P<0.01). The two methods showed a mean percent-difference of 52.3% (95% CI 50.4 – 54.7%), and limits of agreement of 34.6% (95% CI 30.9 – 38.2%) to 70.6% (95% CI 66.9 – 74.3%).

Although fMBV fitting with narrow and wide bounds on physiologic parameters produces broadly different mean pixelwise fMBV in our maps, both methods show a significant difference in fMBV between remote and ischemic myocardial segments in N=5 ischemic swine models. Following fMBV fitting with narrow boundary conditions, we found a median fMBV of 10.52% (IQR 10.00 – 12.03%) in N=13 ischemic segments and a mean pixelwise fMBV of 6.17±1.33% in N=73 remote segments. A Mann-Whitney test found a significant difference in fMBV between these remote and ischemic segments (P<0.01). Likewise, we also found a significant difference between ischemic (8.34±2.10%) and remote (4.80±1.09%) fMBV fitted using wide boundary conditions on an independent samples t-test (P<0.01).

Noise inherent in pixelwise fMBV maps was computed as the percent-standard deviation of pixelwise fMBV in each segment. In the healthy human subjects, fMBV maps showed significantly lower noise when fitted with narrow boundary conditions (%-standard deviation 43.19±14.39%) than with wide boundary conditions (86.24%, IQR 85.19 – 101.17%) on a Wilcoxon rank sum test (P<0.01). Likewise in N=5 ischemic swine subjects a paired t-test found a significant difference in noise between the narrowly bounded (44.51±17.64%) and broadly bounded (73.01±24.24) fMBV maps.

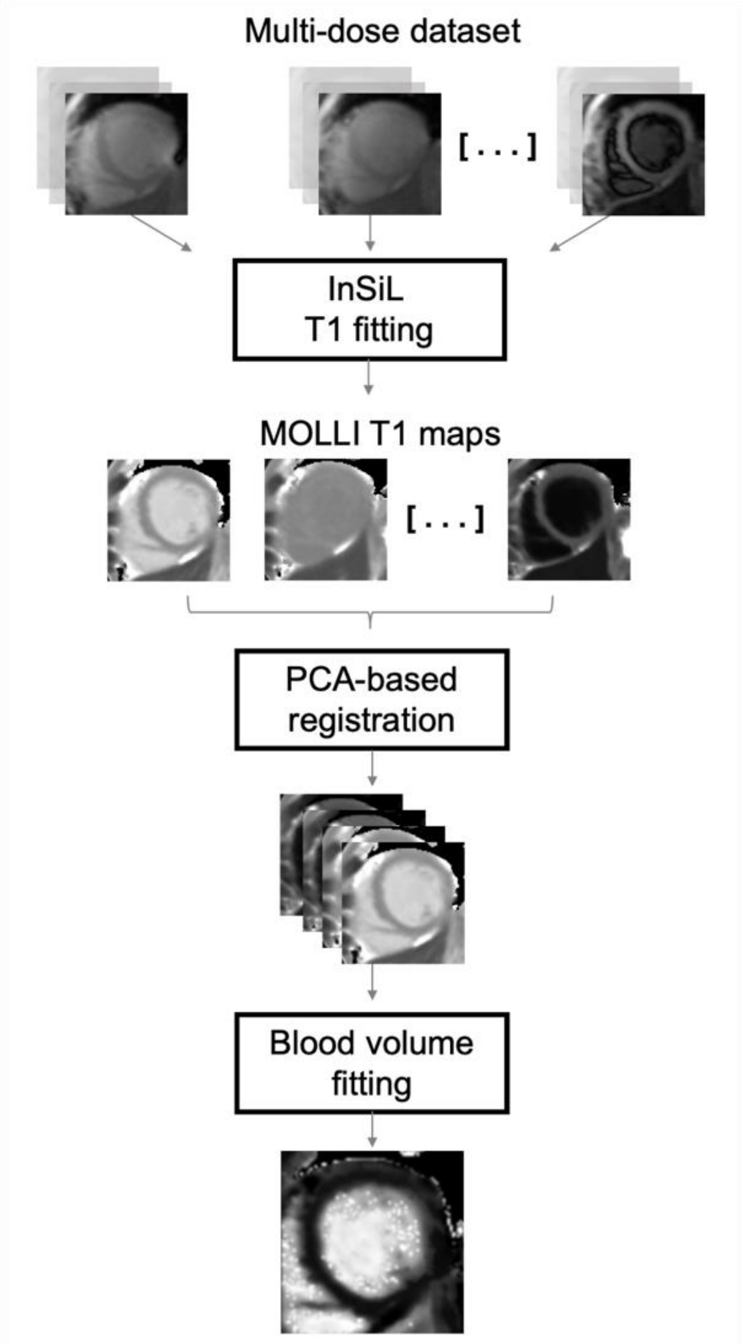

Figure 6.3. Computational flow of the image registration and fMBV mapping pipeline.

Image registration

Signal input curve noise was quantified as previously described in all multi-dose datasets and exported as a registration quality map. Figure 6.4 shows a representative example of registration quality maps in the mid-ventricular myocardium in a single healthy, normal volunteer alongside corresponding fMBV maps. Regions of high signal input noise in the myocardium (Figure 6.4 a – c) often correspond to regions of intermediate fMBV (Figure 6.4 d – f), indicating mixed myocardial and blood pool signal. PCA and LG registration methods shows conspicuous improvement in signal input curve noise in the anterior, inferior, and inferolateral segments.

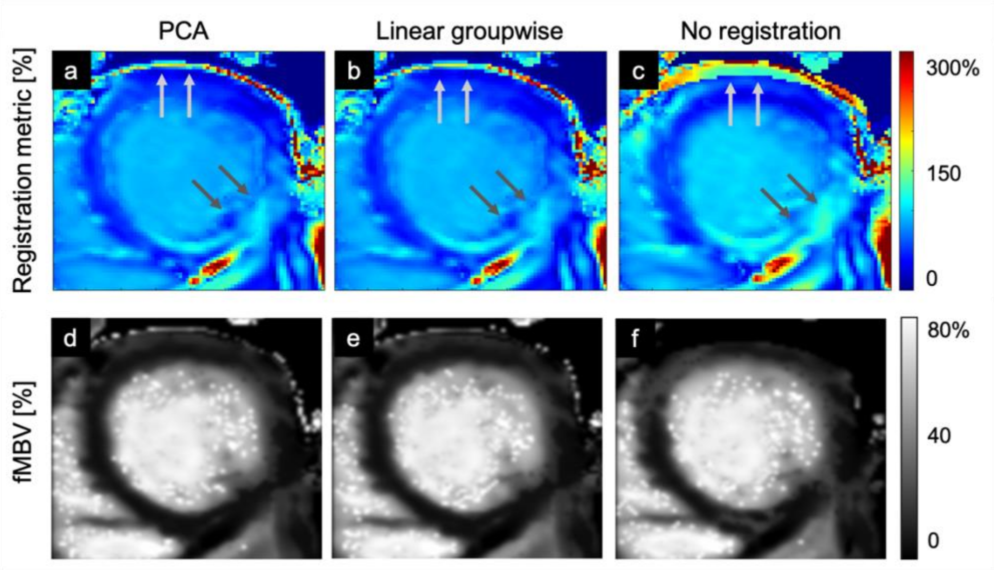

Figure 6.4. Pixel-wise maps of a registration metric derived from the total signal input curve noise (a, b, c) and model-fitted fMBV (d, e, f) in the mid-ventricular myocardium in a single subject. Registration metric maps show visible variation in registration quality in the inferolateral endocardial boundary (dark grey arrows) and anterior epicardial boundary (light grey arrows).

Signal input curve noise was averaged across the registration mask to compute an overall registration quality score. A lower numerical score indicates superior image quality, with typically lower noise in the signal input curve. With no registration applied, human multi-dose datasets showed a mean score of 84.34±36.69. Following PCA and LG registration, human datasets showed registration scores of 69.42±31.26 and 68.84±31.33 respectively. A repeated measures ANOVA found that multi-dose datasets showed a significantly higher registration score without registration than with either the PCA (P<0.01) or LG method (P<0.01), but no significant difference in registration score between the PCA and LG methods (P>0.05, Figure 6.5).

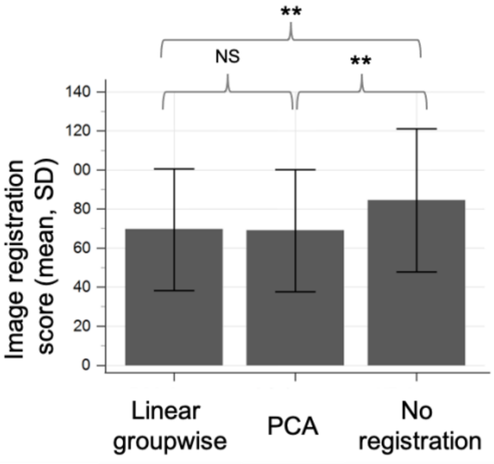

Figure 6.5. Registration score: mean, SD. A repeated measures ANOVA found that datasets registered with the groupwise PCA and linear groupwise methods show significantly lower mean overall registration scores relative to unregistered datasets in 5 healthy human subjects (p<0.01).

Apparent myocardial septal width was measured in all datasets (N=5 healthy humans; N=5 ischemic swine models) on fMBV maps fitted with either no registration or following image registration using the LG and PCA methods. We found a mean septal width of 4.05±1.49 mm at the 15% fMBV threshold in fMBV maps fitted with no image registration. Following LG and PCA registration, fMBV maps showed a myocardial septal width of 4.69 mm (IQR 3.75 – 5.47 mm) and 4.37±1.36 mm respectively. A nonparametric Friedman test found a significant difference in apparent myocardial septal width among the three registration methods (P=0.020). fMBV maps registered with the LG and PCA methods both showed significantly greater apparent myocardial width than fMBV maps fitted without registration. A further paired t-test found no significant difference in myocardial septal width between the LG and PCA methods (P>0.05).

6.4 Discussion

In this study, we evaluated the performance of a PCA-based groupwise image registration method pixelwise fMBV quantification and investigated the effect of optimizer boundary conditions on image noise in model-fitted fMBV maps. We find that pixelwise fMBV maps fitted with wide boundary conditions on all model-fitted physiologic parameters produce apparently blunted fMBV due to frequent failed optimization attempts, although with overall preservation of the distribution of fMBV within each myocardial slice. An investigation of the performance of PCA-based image registration compared to a simple linear groupwise method, as well as non-registered results, found no significant difference in apparent septal myocardial thickness or image registration quality score between the PCA and linear groupwise methods.

Much prior work has been done to develop and evaluate image registration methods for parametric mapping approaches. The PCA-based groupwise image registration method used in this study was developed by Huizinga et al. to improve contrast-based image registration for parametric mapping applications, exploiting the predictable change in image contrast observed in inversion- or saturation recovery experiments, as well as dynamic contrast-enhanced acquisitions.[58] Tao et al. expanded this technique for ECV mapping with pre- and post-gadolinium contrast MOLLI T1 maps.[59] In the present work, we apply a similar implementation of the PCA-based registration method for co-registration of ferumoxytol-enhanced multi-dose MOLLI T1 datasets for fMBV mapping. We find that although multi-contrast MOLLI T1 acquisitions fit the quantitative MRI paradigm described by Huizinga et al., a more traditional linear groupwise registration method performs comparably. This is likely a consequence of the monotonically decreasing blood pool and myocardial T1 throughout the multi-dose dataset. The steady change in image signal throughout the acquisition allows the sum of pairwise correlation coefficients metric to appropriately quantify image registration without the computation of eigenvalues of the signal input curve.

In this study, the spatial distribution of fMBV was visualized using both pixelwise maps and myocardial polar maps based on the AHA model. Polar maps that plot mean fMBV in each myocardial AHA segment can be combined with an fMBV threshold value derived from ROC analysis to identify coronary territories suspicious for obstructive CAD. While the projection of fMBV results onto a polar map helps to highlight the coronary territory or territories suspicious for ischemia, this method may obscure elevated blood volume present only in the subendocardium or in small focal regions. Pixelwise fMBV maps can be used to identify these patterns more precisely. Thresholding methods can also be applied to pixelwise fMBV maps to identify ischemic defects. If combined with a quantitative assessment of the transmural extent of the defect (i.e., the fraction of the myocardial wall thickness that shows a pixelwise blood volume above the ischemic threshold), these measures may provide a powerful tool for the prediction of clinically significant coronary stenosis.

Limitations

This work has several limitations which merit discussion. First, while we performed a comparison of motion correction methods in-plane motion between T1 maps in a ferumoxytol-enhanced multi-dose dataset, these motion correction methods are unable to correct for through-plane motion resulting from cardiac mis-triggering in the setting of single-slice imaging. While reliable, high-quality in-plane registration significantly improves the quality of fMBV maps, through-plane motion remains an unresolved challenge. Second, the investigation of tissue parameter boundary conditions is limited to the setting of a single constrained nonlinear optimization solver. While a wide range of optimization methods exist, this function is a popular choice for use in pixel-wise fitting applications in which long processing times are compounded across many pixels.

6.5 Conclusions

Tissue compartmental modeling utilizing novel iron-based intravascular contrast agents has the potential to provide additional insight into myocardial perfusion. We have demonstrated that reliable, high-quality image registration and sensible optimization boundary conditions are both necessary components of the image processing pipeline used to generate pixelwise maps of the intramyocardial vascular distribution volume. While a PCA-based image registration technique designed for parametric mapping applications produces high-quality image registration in both human and large animal studies, simpler image registration methods are also effective. Boundary conditions on compartmental model parameters, chosen with care based on an expected range within a given tissue, also improve fMBV mapping results.

Chapter 7 fMBV in ischemic swine models: an investigation of the diagnostic performance of a novel imaging biomarker

7.1 Introduction

Elevated fMBV has been proposed as a compensatory response to myocardial hypoperfusion downstream from a significant coronary stenosis.[24] MBV and myocardial blood flow (MBF) demonstrate a non-linear relationship in the setting of elevated myocardial oxygen consumption.[41,42] As a result, fMBV provides additional insight into myocardial perfusion beyond what is provided by MBF alone.[43] However, clinically relevant diagnostic methods available for estimation of fMBV are limited and thus remain an area of intense cardiovascular imaging research. To fill this gap, multi-compartmental modeling approaches can be combined with contrast-enhanced cardiac MRI to quantify fMBV and produce pixelwise myocardial blood volume maps.[24,57] A true intravascular contrast agent eliminates the need to account for contrast leakage into the extravascular space.[38] As the only true intravascular agent clinically available for off-label diagnostic MRI, ferumoxytol is well-suited for translational MRI studies of fMBV and perfusion.[10,12,13,15] The suitability of ferumoxytol for use in patients with impaired renal function is also a desirable characteristic.

Estimation of fMBV from contrast-enhanced MRI using a two-compartment tissue model requires the simultaneous estimation of myocardial transvascular water exchange. Recently, researchers have proposed a two-compartment water exchange model based on ferumoxytol-enhanced MRI for the estimation of fMBV in normal swine.[57] The present study aims to determine whether fMBV can be used to differentiate between perfused and hypoperfused myocardial regions in swine models of acute myocardial hypoperfusion, and to characterize its diagnostic performance in the setting of single vessel coronary stenosis. We aim to address the following questions: 1) Can pixel-wise fMBV maps quantitatively distinguish hypoperfused from normal and remote myocardium at rest, without requiring the use of a pharmacologic stress agent? 2) What are the sensitivity and specificity thresholds for fMBV as a predictor of resting tissue hypoperfusion? 3) To what extent do regions of rest ischemia and remote myocardial regions show differences in the myocardial transvascular water exchange rate?

7.2 Methods

Healthy and ischemic swine models

Twenty-three juvenile Yorkshire swine (11 female, 12 male; 20 – 33 kg; Premier BioSource, Ramona, CA) were included in the study. Our healthy, control cohort consisted of four swine (4 female, 22 – 26 kg) and our ischemic swine cohort consisted of 19 swine (7 female, 12 male; 20 – 33 kg). To create our ischemic swine models, we induced an artificial stenosis in the mid-LAD artery previously described.[17,18] Following implant deployment, we measured the resting full-cycle ratio (RFR) across the artificial coronary stenosis at rest, as well as fractional flow reserve (FFR) at peak pharmacologic stress (adenosine, 300 µg/kg/min, 4 min infusion) using a coronary pressure wire (PressureWire X, Abbott Laboratories, Abbott Park, IL, USA; CoroFlow Cardiovascular System, Coroventis, Uppsala, Sweden).[117,118] In all swine receiving invasive intervention, we maintained an activated clotting time above 300 seconds with intravenous heparin throughout the procedure to prevent thrombus formation.

Magnetic resonance image acquisition

After anesthesia alone (N=4) or anesthesia with subsequent coronary implant deployment (N=19), we transferred the swine subjects to a whole body clinical 3.0 T magnet (Prisma®, Siemens Medical Solutions USA, Malvern, PA) equipped with phased-array coils. Following localizers, we acquired short- and long-axis cine images using a gradient-echo sequence to assess myocardial contractility [FOV = 292 x 360 mm, matrix size = 102 x 126, TR = 5.2 ms, TE = 2.5 ms, slice thickness = 6 mm, pixel bandwidth = 450 Hz, flip angle = 12˚].

We performed a ferumoxytol multi-dose T1 mapping study in all swine (N=23). We acquired basal, mid-ventricular, and apical short-axis T1 maps using the 5(3)3(3)3 MOLLI sequence[109] with a bSSFP readout [FOV = 240 x 300 mm, matrix size = 384 x 308, TR = 2.6 ms, TE = 1.08 ms, slice thickness = 8 mm, pixel bandwidth = 1085 Hz, flip angle = 35˚, TI = 100 – 180 ms]. We acquired a set of native MOLLI T1 images. A total intravenous dose of 4.0 mg/kg ferumoxytol (20-fold dilution) was administered in six aliquots via slow infusion (cumulative dose 0.25, 0.5, 1.0, 2.0, 3.0 and 4.0 mg/kg; infusion rate 0.33 mg/kg/min). We acquired the same set of T1 images at steady state following each incremental ferumoxytol dose. The typical total duration of the ferumoxytol multi-dose imaging study was approximately 55 minutes.[57]

Ex vivo Tc-99m radiolabeled red blood cell fMBV assay

To evaluate the performance of ferumoxytol-enhanced MRI-fMBV relative to an existing nuclear medicine MBV technique for prediction of regional wall motion abnormalities (RWMA) as markers of hypoperfusion, we performed Tc-99m radiolabeled red blood cells (RBCs) assays in four normal swine subjects and one ischemic swine. We acquired multi-dose ferumoxytol-enhanced MRI T1 maps in left ventricular (LV) short axis slices covering the entire LV myocardium as described. Following MRI, we radiolabeled and intravenously administered RBCs (3.0 mCi/kg, UltraTag, Curium Pharma, Saint Louis, MO), and drew a 5 mL reference whole blood sample. After euthanasia with an intravenous injection of a concentrated solution of potassium chloride (100 mg/kg), we excised the heart and sectioned the LV into 8mm short axis slices, which were segmented and weighed (Figure 7.1). We measured the activity of all myocardial tissue segments and reference blood samples using a Packard Cobra II gamma counter (PerkinElmer Inc, Shelton, CT) calibrated for Tc-99m. Tissue blood volume was computed as the ratio of tissue specific activity to blood specific activity.[119]

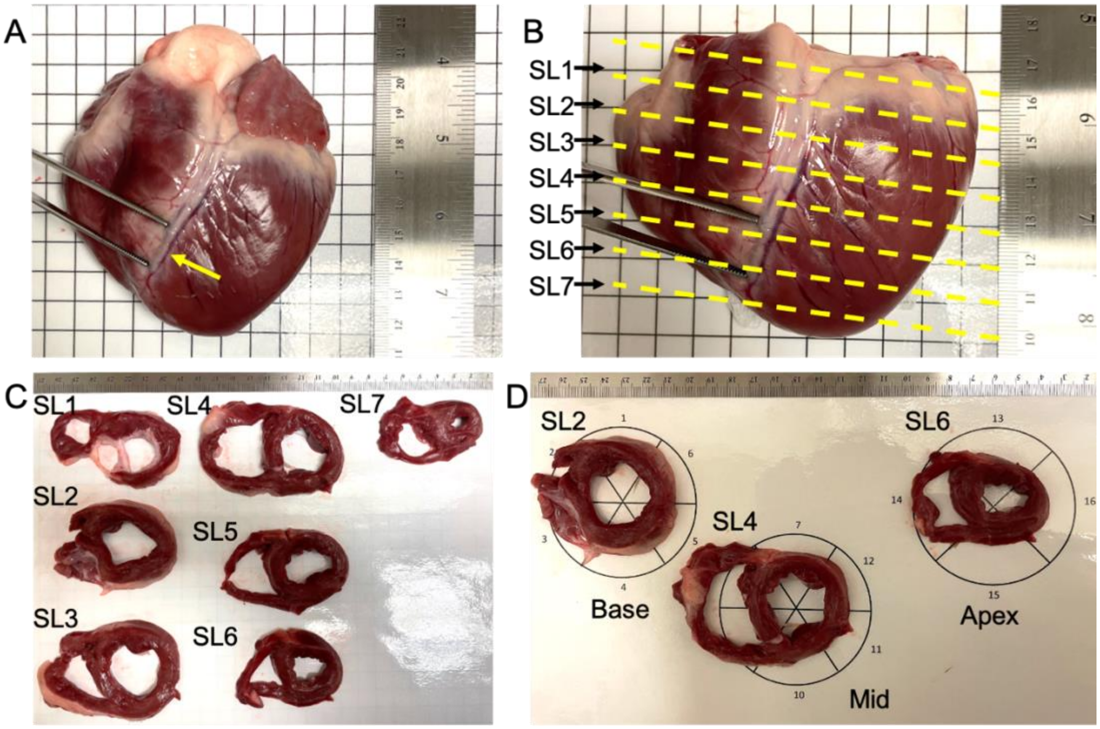

Figure 7.1. Segmentation of heart tissues for radiolabeled red blood cell study in an ischemic swine. Yellow arrow indicates location of the intracoronary stenosis implant (A). Dashed lines indicate boundaries of short-axis slices (B). Short-axis slices are arranged from most basal (SL1) to most apical (SL7, C) and three representative short axis slices were prepared for radioactivity measurements (D).

Image Processing and Analysis

We used the Instantaneous Signal Loss simulation (InSiL) algorithm for T1 fitting of MOLLI images.[33] Following T1 fitting, we co-registered each set of multi-dose InSiL T1 maps (0.0 – 4.0 mg/kg ferumoxytol) using Elastix 5.0.0.[57,98] Taking care to exclude trabeculations and papillary muscles, we contoured a central region of the mid-LV blood pool to extract blood R1 at each ferumoxytol dose. We used a two-compartment water exchange model with three-parameter fitting implemented in MATLAB (MathWorks, Natick, MA) to fit for pixelwise fMBV and water exchange rate in all slices.[57]

After pixelwise computation, both fMBV and water exchange maps were exported as DICOM images. Using commercially available software (Osirix, Pixmeo, Bernex, Switzerland), we contoured and segmented each pixelwise fMBV map and its corresponding water exchange map based on the AHA 17-segment model, excluding segments with severe artifacts (CMC, 4 years cardiovascular MRI experience).[99]

Because myocardial contractile dysfunction ranging in severity from hypokinesis to akinesis is indicative of hypoperfusion and the onset of myocardial stunning, one reader also assessed short axis cine images for RWMAs using a 3-point Likert scale (1 = normal, 2 = hypokinetic, 3 = akinetic).[16] We categorized myocardial segments within the LAD territory with RWMA scores of two or greater as ischemic. Segments perfused by the right coronary artery (RCA) and left circumflex (LCX) artery that showed normal wall motion were characterized as remote.

Statistical Analysis

Data were tested for normality using the Kolmogorov-Smirnov test. Data are reported as mean ± standard deviation or median (inter-quartile range) according to normality. To determine whether model-fitted fMBV and water exchange can distinguish between ischemic and remote myocardial regions in the same subject, we used paired, two-sided Student's t-tests and paired Wilcoxon signed rank tests for group comparisons. We used a Kruskal-Wallis test to compare ischemic, remote, and normal fMBV. To examine sex-specific differences between ischemic and remote fMBV in male and female swine subjects, we used a Kruskal-Wallis test with a post-hoc Conover test[120] for pairwise comparison of subgroups. To further evaluate the diagnostic performance of fMBV as a marker for myocardial hypoperfusion, we computed its receiver operating characteristic (ROC) curve with binary variable responses (0 = remote, 1 = ischemic) based on RWMA grading. To compare the diagnostic performance of MRI-fMBV relative to ^{99m}Tc-fMBV to predict RWMA as markers of tissue hypoperfusion, we performed pairwise comparison of the area under the ROC curves (AUC) for both techniques. A p-value <0.05 was considered statistically significant. Statistical analysis was performed using MedCalc 19.0.5 (MedCalc Software, Ostend, Belgium).

7.3 Results

Across all 23 swine included in the study, no ferumoxytol-related hypotension or allergic reactions occurred. In swine with coronary stenosis implant insertion, no intervention-related ventricular fibrillation, ventricular tachycardia, or deaths occurred.

All 19 swine models that underwent percutaneous coronary stenosis implant placement had single vessel LAD coronary stenosis of at least moderate severity on x-ray angiograms by visual assessment. Stenosis implant length averaged 7.3 ± 3.1 mm (range = 4.0 to 15.0 mm). The mean corresponding FFR measurements at peak adenosine stress in 11 swine was 0.90 ± 0.05 while mean RFR measurements acquired at rest was 0.92 ± 0.07. The threshold value for clinically significant ischemia in humans has been proposed as 0.86 using iFR (instantaneous wave-free ratio),[121] a method that has shown string agreement with measures of RFR.[117] Of 210 myocardial MRI segments acquired in ischemic swine models, one was rejected due to a severe artifact. Of the remaining 209 segments, we identified 169 segments as remote, and 40 as ischemic (hypoperfused, ischemic, or stunned myocardium). Thirty-eight of the 40 myocardial segments identified as hypokinetic or akinetic corresponded to the LAD perfusion territory. Two swine had hypokinesis of the apical inferior LV segment due to the course of the LAD.

fMBV and water exchange rate in ischemic, remote, and normal myocardium

Both fMBV and transvascular water exchange rate differed significantly between remote and ischemic myocardial segments. In 19 swine models of acute myocardial hypoperfusion, mean ischemic fMBV was greater than mean remote fMBV by a factor of 1.42. Ischemic segments showed significantly higher mean fMBV relative to remote segments (11.72 ± 3.00% vs 8.23 ± 2.12%, $p < 0.0001$, N = 40 ischemic ROIs). No significant difference in fMBV was observed between remote and normal myocardial segments (8.23 ± 2.12% vs 8.38 ± 2.23%, $p>0.05$) (Figure 7.2). Prior work indicates that fMBV estimation based on the fast-exchange approximation[45] would be insufficiently precise to discriminate ischemic from remote fMBV in this range.[57] A full summary of the fMBV and transvascular water exchange rate by coronary territory in all swine subjects is provided in Appendix 1.2.

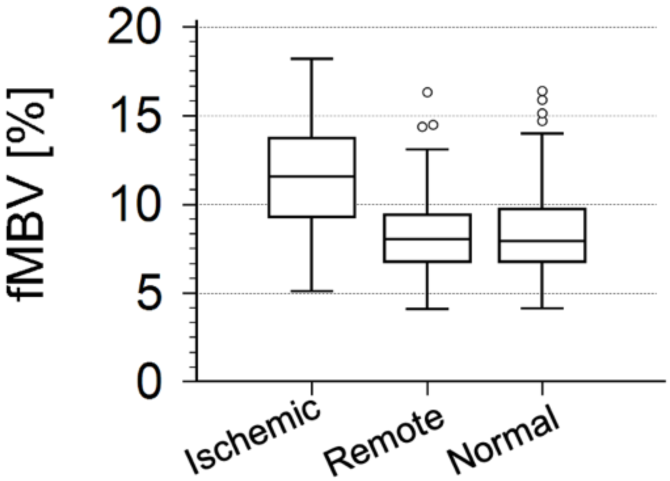

Figure 7.2. Pixel-wise fractional myocardial blood volume (fMBV) of ischemic (N=40), remote (N=169), and normal (N=136) left ventricular myocardial segments at 3.0T.

Though less severe, we found a similar difference in the median transvascular water exchange rate k_i (s^{-1})[48] between ischemic and remote segments. Ischemic segments showed a mean k_i of 15.32 ± 8.69 s^{-1}, while we found a median k_i of 17.78 (11.60, 26.36) s^{-1} in remote segments and 19.13 (12.82, 26.69) s^{-1} in normal segments. Using a non-parametric Wilcoxon signed rank test, we found a significant difference in k_i between contralateral ischemic and remote segments (*P*=0.0006, N = 40 ischemic ROIs).

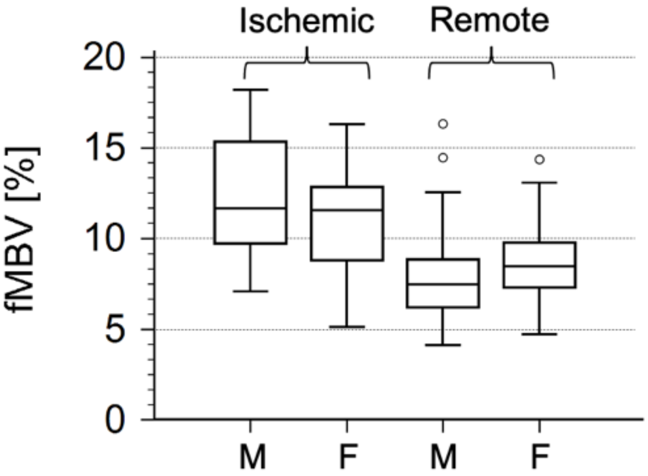

Figure 7.3. Sex-specific fractional myocardial blood volume (fMBV) at 3.0T. N=7 female [18 ischemic, 97 remote segments]; N=12 male [22 ischemic, 71 remote segments]. A Kruskal-Wallis test found significant difference in remote fMBV between male and female swine (P<0.05), but no significant difference in ischemic fMBV (P>0.05).

Sex-specific differences for fMBV in ischemic and remote myocardial tissues are shown in Figure 7.3. We found no statistically significant difference in ischemic fMBV between male and female swine. In seven female swine, the mean fMBV was 11.20 ± 2.74% in ischemic (N=18) and 8.57 ± 1.89% in remote (N=97) segments, respectively. In 12 male swine, the mean fMBV was 12.15 ± 3.20 in ischemic (N=22) segments and 7.76 ± 2.35 in remote (N=71) segments, respectively. Relative to male swine, female swine had higher fMBV in remote segments at rest. The mean fMBV ratio of ischemic to remote segments was higher for male

(1.7) relative to female (1.3) swine. The Kruskal-Wallis test found a significant difference between the male-ischemic, male-remote, female-ischemic, and female-remote subgroups (*P*<0.001). The post-hoc pairwise Conover test found a significant difference between the male-remote and female-remote subgroups (all *P* values <0.05), but no significant difference between the male-ischemic and female-ischemic subgroups (all *P* values >0.05).

Pixel-wise fMBV and transvascular water exchange maps in normal and ischemic swine models

Representative polar maps and pixelwise fMBV maps from three swine subjects are shown as illustrative examples in Figures 7.3-7.4: a healthy normal 26 kg female swine, a moderately ischemic 26 kg male swine model, and a severely ischemic 28 kg female swine model. These swine subjects were selected for their superior image quality and comprehensive range of ischemic severity. Both polar maps based on AHA classification (Figure 7.4) and pixelwise color-rendered maps (Figure 7.5) depict the phenomenon of elevated fMBV and restricted water exchange in myocardial tissues downstream from an artificially induced focal coronary stenosis. In the healthy swine, mean pixelwise fMBV and transvascular water exchange polar maps (Figure 7.4A) show a gradient of increasing fMBV and shortening water exchange rate from the basal to apical regions of the LV. In the two ischemic swine subjects shown (Figure 7.4, B-C), we expect all myocardial segments in the territory downstream from the stenotic proximal LAD to be hypoperfused, and to present with elevated fMBV in response. Elevated fMBV, appearing yellow to white, can be seen in the basal, mid-ventricular, and apical slices of the hypoperfused LAD territory in both ischemic swine models, while restricted water exchange (appearing white to cerulean) corresponds to the same myocardial segments showing elevated fMBV (Figure 7.4 B-C).

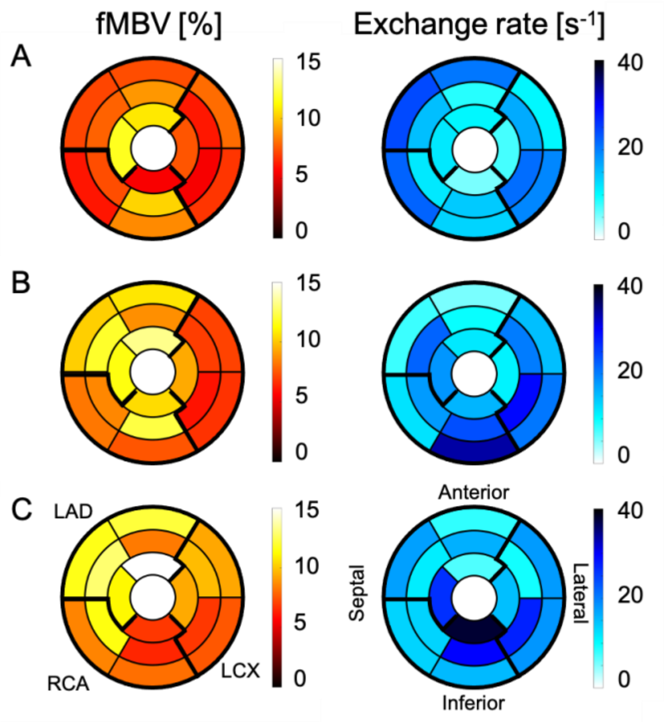

Figure 7.4. Polar maps of mean segmental fMBV [%] and water exchange rate [s-1] in three swine models. (A) healthy normal 26 kg female swine, (B) moderately ischemic 26 kg male swine model, (C) severely ischemic 28 kg female swine model.

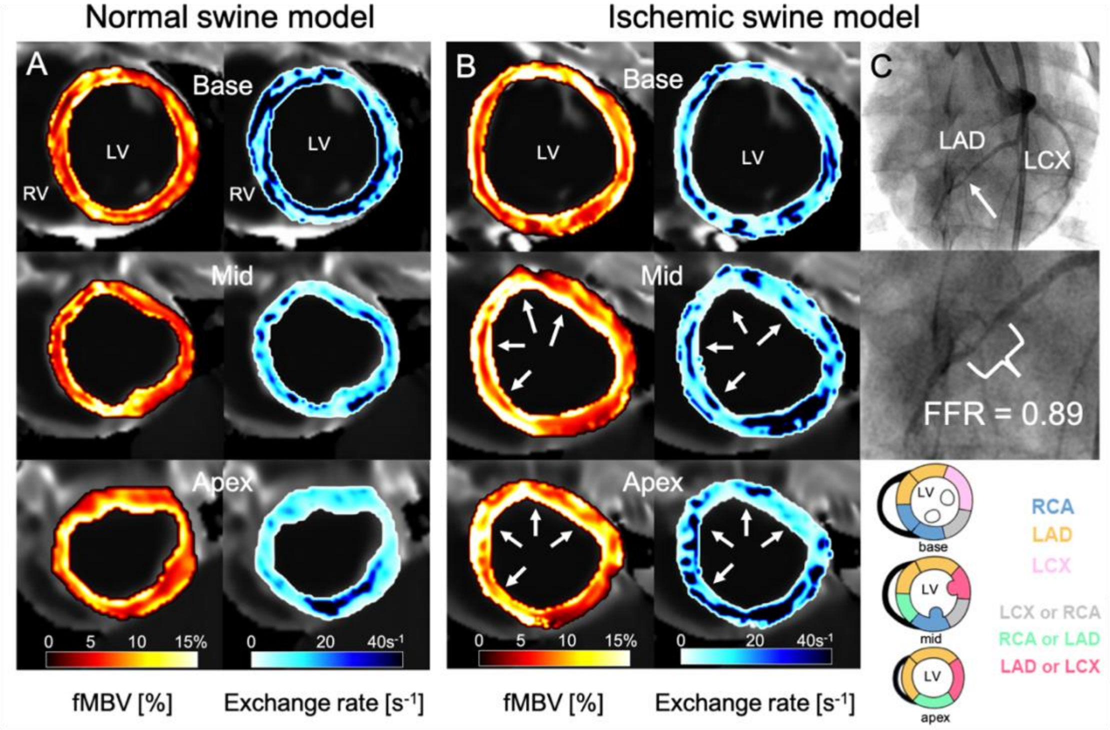

Figure 7.5. Illustrative examples of fMBV maps of the left ventricle in a normal 26 kg female swine and a severely ischemic 28 kg female swine mode. fMBV and water exchange maps in a healthy, normal swine (A) show normal blood volume distribution. Maps in a severely ischemic swine model (B) show elevated fMBV in the left anterior descending (LAD) territory (white arrows) and restricted water exchange (white arrows), respectively. X-ray fluoroscopic images (C) show severe coronary narrowing (white arrow) and a corresponding fractional flow reserve (FFR) value of 0.89.

Regional differences in elevated blood volume can also be depicted on a pixel level using colorized pixelwise fMBV maps. Figure 7.5 shows pixelwise maps of fMBV and water exchange in the same healthy, normal 26 kg female swine and severely ischemic 28 kg female swine. X-ray fluoroscopic images in the severely ischemic swine (Figure 7.5C) show angiographic coronary narrowing caused by the stenosis implant in the LAD. Following deployment of the implant, the artificially stenosed LAD showed an FFR of 0.89, RFR of 0.97. Figure 7.5 C depicts the LAD, RCA, and LCX territories in the basal, mid-ventricular and apical myocardial short-axis slices. The apical inferior segment may be perfused primarily by the LAD or RCA, dependent on individual coronary anatomy. These pixelwise maps (Figure 7.5 A-B) show qualitative and quantitative heterogeneity in fMBV and water exchange across ischemic, remote, and normal myocardial tissue.

Diagnostic performance of pixelwise MRI-fMBV relative to ^{99m}Tc-fMBV as a biomarker of myocardial ischemia

Using pairwise comparison of the AUCs, MRI-fMBV has higher diagnostic performance for the prediction of RWMAs as a proxy for tissue hypoperfusion relative to ^{99m}Tc-fMBV (P=0.013, 95% CI 0.04, 0.38). The MRI-fMBV ROC curve is shown in Figure 7.6. We found an AUC for pixelwise MRI-fMBV of 0.89 (P < 0.001, 95% CI 0.80, 0.95). The fMBV criterion of 9.60% is associated with a specificity of 90.0% (95% CI 76.3,97.2) and a sensitivity of 72.5% (95% CI 56.1, 83.4). ^{99m}Tc-fMBV has an AUC of 0.59 (P <0.001, 95% CI 0.52, 0.67). In the ischemic swine cohort that underwent both MRI and ex vivo measurement of ^{99m}Tc RBC activity, MRI-fMBV is able to distinguish between ischemic and remote segments (P<0.001, [95% CI 1.72, 5.90]) while ^{99m}Tc-fMBV was not statistically significant between ischemic and remote segments (P=0.19, [95% CI -0.16, 0.79]).

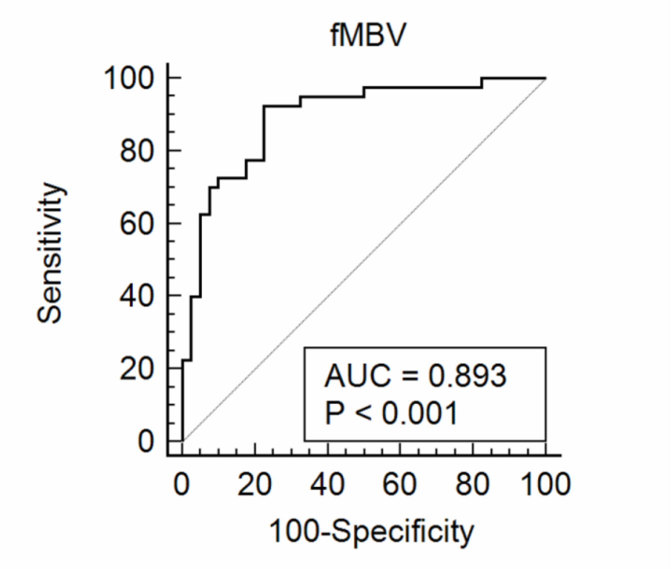

Figure 7.6. Receiver operating characteristic (ROC) curve of segmental pixelwise fractional myocardial blood volume (fMBV).

7.4 Discussion

Our results provide early support for ferumoxytol-enhanced MRI-derived pixel-wise fMBV maps to depict a resting perfusion deficit in swine with artificially-induced coronary stenosis. In these swine models, we found an fMBV threshold of 9.60% has a specificity of 90.0% and a sensitivity of 73% to detect tissue hypoperfusion. Similarly, ischemic and remote myocardial regions show differences in the myocardial transvascular water exchange rate. While there is higher baseline MRI-fMBV in the remote segments of our female swine models, no statistically significant sex-specific differences in fMBV for ischemic and remote myocardial tissue was noted. Our preliminary findings lay the groundwork for using fMBV derived from ferumoxytol-enhanced MRI to distinguish ischemic from remote myocardium at rest, obviating the need for pharmacologic stress agents.

In our two-compartment model of myocardial tissue for estimation of fMBV, the exchange rate of water molecules from the intracapillary blood pool to the extravascular space,

k_i, corresponds to the inverse of the mean intracapillary water residence time τi.[49,57] Two-compartment, single-exchange models such as ours are simpler to formulate than higher order models that account for more tissue compartments and multiple water exchange patterns. Two-compartment models assume the exchange rate of water between the intracellular and extracellular spaces to be sufficiently fast as to produce a negligible effect on MRI signal. This assumption is supported by studies in ex-vivo animal tissues.[50,52] As intravascular contrast agents remain entirely within the intracapillary blood pool within our specified sampling time frame, intramyocardial water is exposed to two separate spin relaxation environments as it diffuses between compartments. As a result, the rate of water exchange between these compartments significantly impacts the MRI signal of a given voxel of perfused myocardial tissue. Measuring myocardial and blood pool T1 over a range of intravascular contrast agent doses allows us to fit for the fMBV and exchange rate that best describes the MR signal in each voxel.

Although previous works have investigated the use of intravascular contrast agents combined with a compartmental modelling approach to estimate fMBV, studies conducted in the setting of myocardial ischemia using iron-based agents are sparse. A 2002 study investigated fMBV in six patients presenting with evidence of CAD on x-ray angiography using the contrast agent NC100150, a saturation recovery turbo Fast Low-Angle Single sHot (FLASH) sequence, and a two-compartment water exchange model. The study reported a mean fMBV of 12.9% and an intracapillary water residence time τ_i ($1/k_i$) of 269 ms across the whole short-axis myocardial view, fitted to the complete dataset, and did not individually analyze fMBV in ischemic and remote regions.[111] We found a mean fMBV and water exchange rate of 11.72 ± 3.00% and 15.32 ± 8.69 s^{-1} in ischemic segments, compared to values of 8.23 ± 2.12% and 17.78 (11.60, 26.36) s^{-1} in remote segments.

fMBV holds promise both as a means of discriminating between ischemic and remote myocardial territories and quantifying the severity of myocardial hypoperfusion where it exists. Using pairwise comparison of AUCs, we showed that ferumoxytol-enhanced MRI-fMBV may be more sensitive for discrimination between ischemic and remote myocardial tissues segments relative to 99mTc-fMBV. Tc-99m RBC activity did not significantly differ in the hypoperfused LAD territory relative to other coronary territories.

The clinical availability of fMBV as a noninvasive imaging biomarker with high specificity in the detection of physiologically significant coronary stenosis would carry important implications for therapeutic decisions. Multiple techniques exist to qualitatively and quantitatively image ischemia and perfusion using CMR, and most of these rely on pharmacologic stress agents which complicate imaging workflow and carry additional risk of side effects.[122] While exercise CMR ameliorates this risk, high-quality exercise stress CMR images are challenging to acquire, and MR-compatible exercise equipment is typically costly. Stress perfusion CMR techniques, which use gadolinium contrast to image perfusion defects in the first-pass phase, have notable limitations in addition to their reliance on pharmacologic stress. Semiquantitative perfusion imaging is not sensitive to diffuse disease, while quantitative approaches require consistent implementation of complex acquisition protocols.[122] GBCAs also carry safety concerns associated with long term tissue deposition even in the setting of normal kidney function.[123]

The unique value proposition of our ferumoxytol-enhanced fMBV mapping technique is that it does not require either pharmacologic or exercise stress to capture the effects of inducible ischemia. Rather, our technique directly captures the increase in myocardial intracapillary blood volume at rest that results in observably blunted perfusion reserve with stress testing techniques.

While our full multi-dose steady-state CMR technique entails longer exam times than a typical perfusion imaging study, early evidence supports use of an abbreviated imaging protocol requiring only three ferumoxytol-enhanced acquisitions.[57] By reducing total scan time to 35 minutes, this abbreviated protocol may facilitate translation of the technique to clinical imaging studies.

Several limitations of this study warrant further discussion. First, we demonstrated our technique in swine models to isolate the effects of focal single vessel coronary stenosis on model-fitted fMBV in a preclinical study, free of confounding factors. However, in patients who undergo stress perfusion imaging, diffuse luminal coronary disease and multi-vessel disease are common, and both epicardial coronary as well as underlying microvascular ischemic disease may be at play. To tune our fMBV model for a wide spectrum of pathology in chronic ischemic heart disease, further validation in patients will be necessary. Second, while prior work has demonstrated evidence of significant myocardial ischemia in swine models with intracoronary stenosis implants in the size range used in this study,[18,84] we measured a mean FFR of 0.90 ± 0.05 in the setting of fluoroscopically defined moderate to severe coronary stenosis. Although well established in human patients to define clinically significant coronary stenosis,[124] the human-centered FFR < 0.8 threshold may not be equally applicable to our juvenile swine models because orthogonal coronary views during fluoroscopy confirmed the moderate to severe stenosis and flow-limiting lesion created by our coronary stenosis implant. Third, while ferumoxytol contrast is ideal for steady-state blood volume mapping applications, it is only marketed in the United States, and its use for MRI remains off-label. Finally, the use of intravenous iron agents carries the risk of rare, severe hypersensitivity reactions; however, the safety profile of ferumoxytol for off-label diagnostic use is highly favorable.[10]

7.5 Conclusion

Pixel-wise fMBV maps derived from ferumoxytol multi-dose T1 MRI can be used to distinguish ischemic from remote myocardial tissues in swine models of myocardial hypoperfusion. For patients with renal impairment, the availability of a suitable method for estimating myocardial perfusion is particularly valuable. Validation of our model-fitted fMBV derived from ferumoxytol-enhanced MRI in patients with chronic ischemic heart disease will be needed to fully characterize the distribution of fMBV in ischemic and remote myocardial regions. If confirmed in a broader translational study of patients, fMBV may serve as a potential direct marker of myocardial tissue perfusion at rest.

Chapter 8 In vitro and in vivo MRI properties of three ultrasmall superparamagnetic iron oxide nanoparticles

8.1 Introduction

The search for new and alternative MRI contrast agents is motivated by the goal of improved diagnostic performance while ensuring patient safety. In recent years, ferumoxytol has garnered attention as a blood pool MRI contrast agent with powerful imaging attributes. However, ferumoxytol lacks an approved imaging label, is only marketed in the U.S., and commands a high price point, impeding widespread adoption. Ferumoxytol has shown strong biosafety and biocompatibility in-vitro and in-vivo.[125] It has been employed successfully for magnetic resonance angiography (MRA), particularly blood pool imaging and tissue compartmental modelling.[12,24,57,126] Similar in characteristics to Feraheme, two alternative USPIOs have recently gained attention: Molday ION (BioPal, Worcester, MA) and generic ferumoxytol (Sandoz, Princeton, NJ). Currently used as a research agent for cell labeling[127] and pre-clinical imaging,[128–130] Molday ION shares many chemical and biological properties with Feraheme. Molday ION was developed to achieve a comparable r1 and r2 relaxivity, biological half-life, and similar safety profile to Feraheme. Generic ferumoxytol has U.S. FDA approval for the same therapeutic indication as Feraheme.

In this study, we compared the relaxivities of Feraheme, generic ferumoxytol, and Molday ION, and we evaluated their contrast effects in a combined in-vitro and in-vivo MRI study. We hypothesize that at 3.0T, Feraheme, generic ferumoxytol, and Molday ION (1) demonstrate similar r1 and r2 relaxivities in saline, human plasma, and whole blood; (2) perform similarly in vivo across several pulse sequences for bright-blood and dark-blood cardiovascular and abdominal applications; and for quantitative applications such as the estimation of fractional intravascular contrast distribution volume as surrogates for tissue blood volume, (3) computed values derived from each agent will be similar across a cohort of normal swine.

8.2 Methods

In-vitro phantom experiments

Three units of fresh healthy human whole blood were combined to form a homogeneous blood sample. Five additional units of whole blood underwent centrifugation and separation. Separated plasma was combined to yield a homogeneous plasma sample. We prepared MRI phantoms composed of normal saline, human whole blood, and plasma, doped with Feraheme, generic ferumoxytol, or Molday ION at concentrations of 1/2048 [0.26 mM] (least concentrated), 1/1024 [0.52 mM], 1/512 [1.05 mM], 1/256 [2.10 mM], and 1/128 [4.20 mM] (most concentrated). A contrast concentration of 1.0 mM corresponds to an in-vivo dose of approximately 4.0 mg/kg in a 75 kg patient with a total circulating blood volume of 5 liters. Relaxation measurements were performed in a single session using a 3.0T clinical MRI scanner (Skyra®, Siemens Medical Solutions, Malvern, PA) at ambient temperature (22° C). Phantoms were allowed one hour to calibrate to the same temperature as the MRI scanning room. The temperature of the non-contrast normal saline tube was measured with a digital thermometer immediately prior to and following completion of the experiment. Inversion-recovery spin echo sequences with 10 different inversion times (TIs) were used to measure the longitudinal spin relaxation rate R1 (s^{-1}) in three coronal slices (upper, middle, lower) without parallel imaging. The transverse relaxation rate R2 (s^{-1}) was measured using a multi-echo spin echo sequence with 9 echo times (TEs). We chose the range of TE times to minimize the effects of stimulated echoes at short TE times, as well as the effect of the noise floor at long TEs. Scan parameters are provided in Appendix 1.1. R1 and R2 acquisitions were performed twice for repeatability. We performed a simple linear regression of R1 and R2 against contrast concentration to estimate the r1 and r2 relaxivities ($mM^{-1}s^{-1}$) of Feraheme, generic ferumoxytol, and Molday ION in saline, plasma, and whole blood; TI and TE values at which image signal registered below the noise floor were excluded. A second-order polynomial regression was used to describe r1 relaxivity in blood for all three agents. Due to high noise (low signal) in the sample with the highest contrast concentration (4.20 mM), R2 fitting was performed only for the concentration range 0.26 – 2.10 mM. R1 and R2 maps were fitted in MATLAB (MathWorks, Natick, MA) using a nonlinear least-squares fitting algorithm.

In-vivo imaging

Sixteen swine underwent MRI on a whole body clinical 3.0T magnet (Prisma®, Siemens Medical Solutions USA, Malvern, PA) using T1w and T2w pulse sequences (Appendix 1.2). Seven swine received Molday ION, eight received Feraheme, and one received generic ferumoxytol. In N=9 swine (N = 7 with Molday ION, N=1 with Feraheme, N=1 with generic ferumoxytol), we acquired 1) pre- and post-contrast 3D bright-blood T1w gradient echo images using the VIBE (volumetric interpolated breath-hold examination) sequence,[131] 2) pre- and post-contrast multiplanar 2D dark-blood T2w images using HASTE (half-Fourier acquisition single-shot turbo spin echo),[132] and 3) post-contrast high resolution 4D cardiac phase-resolved images using the MUSIC (Multiphase, Steady-state Imaging with Contrast) pulse sequence,[11] which is specifically designed for contrast-enhanced imaging using intravascular MR contrast agents (Appendix 1.3). Post-contrast HASTE and VIBE imaging was performed 15 minutes after completion of the contrast infusion protocol. Thoracic and abdominal VIBE images (100 – 200 mm overlap) were processed inline to produce a composed, extended field-of-view (eFOV) image series.

To demonstrate the feasibility of quantitative MRI using Molday ION, Feraheme, and generic ferumoxytol for estimation of fractional intravascular contrast distribution volume in myocardium, liver, and spleen, we also performed contrast-enhanced multi-dose T1 mapping studies[57] in all swine (N=16) . Briefly, we acquired native (non-contrast) T1 maps of the left ventricular (LV) basal, mid, and apical short-axis using the 5(3)3(3)3 MOLLI sequence[109] without contrast. Then, MOLLI T1 imaging was repeated following sequential cumulative doses of 0.25, 0.5, 1.0, 2.0, 3.0 and 4.0 mg/kg (20-fold dilution, infusion rate 0.33 mg/kg/min). The maximum cumulative dose of 4.0 mg/kg corresponds to a contrast concentration of approximately 1 mM. Swine were humanely euthanized with sodium pentobarbital (100 mg/kg) while under general anesthesia following completion of experiments.

Image processing and analysis of in-vivo experimental data

Across our VIBE and HASTE images, we analyzed the signal-to-noise ratio (SNR) and contrast-to-noise ratio (CNR) across the blood pool (abdominal aorta and inferior vena cava), longissimus muscle, liver, and spleen. The ROI area was typically 1 cm^2, and when necessary, smaller ROIs within vessels were used. The standard deviation (SD) of SI was recorded in the air outside the body to quantify image noise: $SNR=mean(SI_{tissue}/SD(SI_{air})$. The CNR values of muscle, liver, and spleen were computed relative to blood signal: $CNR=(SI_{tissue} - SI_{blood})/SD(SI_{air})$.

To compute the intravascular contrast distribution volume as a surrogate for fractional tissue blood volume, we used the Instantaneous Signal Loss simulation (InSiL) algorithm[33] to fit MOLLI T1 images for functional quantitative estimation of fractional myocardial blood volume (fMBV) and abdominal organ blood volume. To analyze left ventricular (LV) blood pool and myocardial T1, we contoured ROIs (Osirix, Pixmeo, Bernex, Switzerland) within the anterolateral – lateral myocardial wall (base, mid, apex), and in the mid-LV blood pool (excluding trabeculations and papillary muscles). We co-registered each set of multi-dose InSiL T1 maps (Elastix 5.0.0[98], MATLAB 2020a) and applied a two-compartment water exchange model to fit for fMBV.[57] We segmented each fMBV map based on the AHA 17-segment model, excluding segments with severe artifacts (CMC, 4 years cardiovascular MRI experience).[99] To compare the performance of the contrast agents as abdominal organ blood volume imaging agents, we fit for fractional blood volume (FBV) using MOLLI images that captured liver and splenic tissues.

Statistical analysis

Data were tested for normality using the Kolmogorov-Smirnov test. Data are reported as mean ± SD or median and interquartile range (IQR) according to normality. We used analysis of covariance (ANCOVA)[133] to compare r1 and r2 relaxivity constants among Molday ION, Feraheme, and generic ferumoxytol. We used a two-way analysis of variance (ANOVA) to compare the change in LV blood pool and myocardial T1 dependence on contrast agents. We used a nonparametric Mann-Whitney test to compare estimates of fMBV in normal swine.

8.3 Results

In vitro MRI relaxometry of Feraheme, Molday ION, and generic ferumoxytol

Feraheme, Molday ION, and generic ferumoxytol show similar r1 and r2 relaxivity constants (Table 8.1) and relaxivity curves (Figure 8.1) within each medium (normal saline, plasma, and whole blood). The r1/r2 ratio for Feraheme, Molday ION, and generic ferumoxytol in saline at 3.0T are 0.11, 0.09, and 0.09, respectively. Relative to Feraheme and generic ferumoxytol, Molday ION has higher r1. Computed pixel-wise grayscale R1 and R2 maps of the contrast phantoms (Figure 8.2) illustrate increasing R1 and R2 with increasing contrast concentration. We observed a highly linear correlation ($R^2 > 0.99$) between R1 and contrast concentration for all three contrast agents in saline and in plasma (Figure 8.1). In blood, we observe a nonlinear R1 relaxation curve and achieved a superior fit by using a second-order polynomial regression (all $R^2 \geq 0.99$). A two-way ANCOVA found no significant difference in the variance of R1 with contrast concentration among the three contrast agents (p=0.76). R2 was largely linear ($R^2 \geq 0.99$) for contrast concentration between 0.26 and 2.10 mM in all media (Figure 8.1). Moreover, a two-way ANCOVA found no significant difference in R2 among contrast agents (p=0.10). We found a coefficient of variation of 2.6% (95% CI 2.1 – 3.2%) for R1 and 2.2% (95% CI 1.7 – 2.7%) for R2 between the two repeated acquisitions.

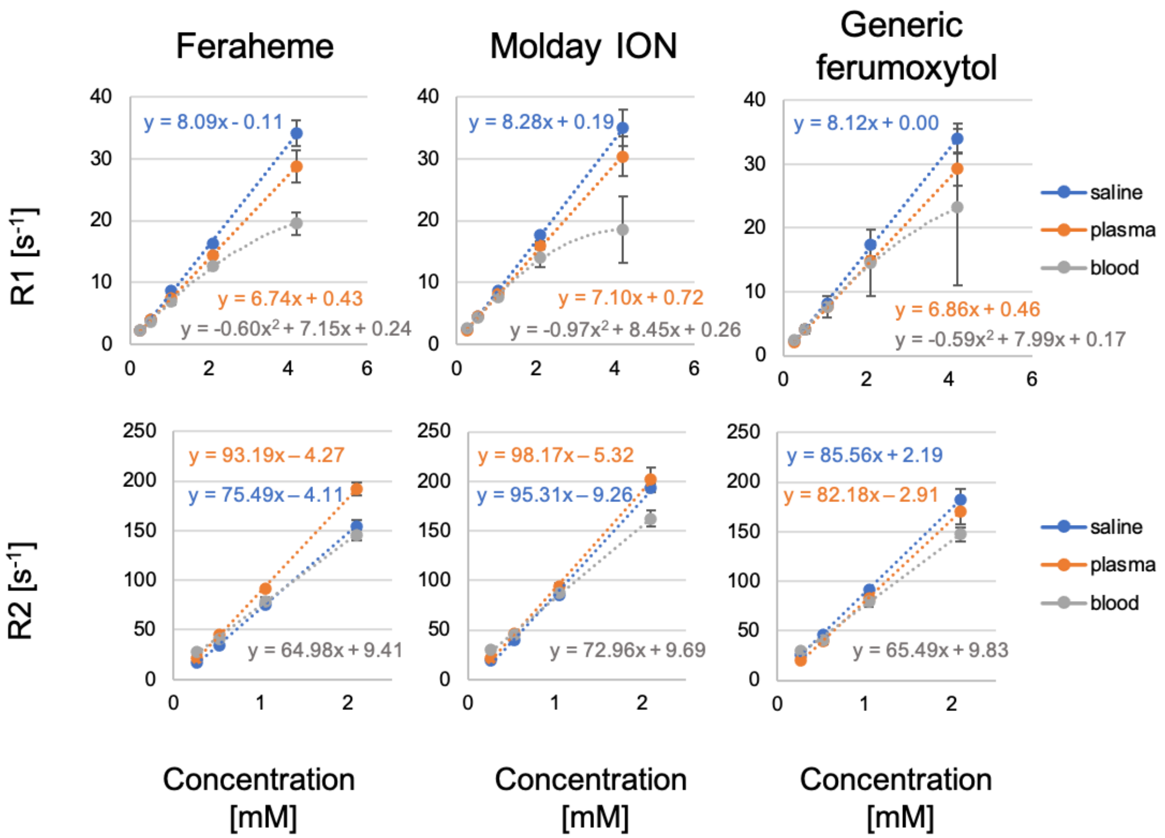

Figure 8.1. In-vitro magnetic resonance relaxivity of Feraheme, Molday ION and generic ferumoxytol were measured in saline, plasma, and whole blood (3.0T, 22° C).

Table 8.1. Relaxivity constants for Feraheme, Molday ION, and generic ferumoxytol in normal saline, human plasma, and human whole blood at 3.0T (22° C).

Contrast	Medium	r_1 relaxivity ($mM^{-1}s^{-1}$)	SE	R^2	r_2 relaxivity ($mM^{-1}s^{-1}$)	SE	R^2
Feraheme (AMAG)	Saline	8.09	0.13	1.00	75.49**	1.08	1.00
	Plasma	6.74	0.02	1.00	93.19	1.24	1.00
	Blood	7.15*	0.37	1.00	64.98	1.77	1.00
Molday ION (BioPal)	Saline	8.28	0.04	1.00	95.31	3.81	1.00
	Plasma	7.10	0.09	1.00	98.17	1.96	1.00
	Blood	8.45*	0.60	1.00	72.96	1.43	1.00
Generic Ferumoxytol (Sandoz)	Saline	8.12	0.09	1.00	85.56	0.92	1.00
	Plasma	6.86	0.02	1.00	82.18	0.75	1.00
	Blood	7.99*	0.37	1.00	65.49	2.25	1.00

Note: $\Delta R1 = r_1 * C$ and $\Delta R2 = r_2 * C$, where r_1 and r_2 are the relaxivity constants ($mM^{-1}s^{-1}$) and C is the iron concentration (mM). The r1 fitting in blood was performed for contrast concentrations between 0.26 – 4.20 mM using a second-order polynomial; r2 fitting was performed only for concentrations of 0.26 – 2.10 mM to minimize inclusion of noise at high concentrations. One-way analysis of covariance (ANCOVA) found no significant difference in the variance of R1 (p=0.76) or R2 (p=0.15) among the three contrast agents. *Values derived from first-order coefficient of a second-order polynomial fit. **The lower r_2 for Feraheme in saline may be related to the phantom being at the edge of the coil and experienced greater B1 inhomogeneity. SE, standard error.

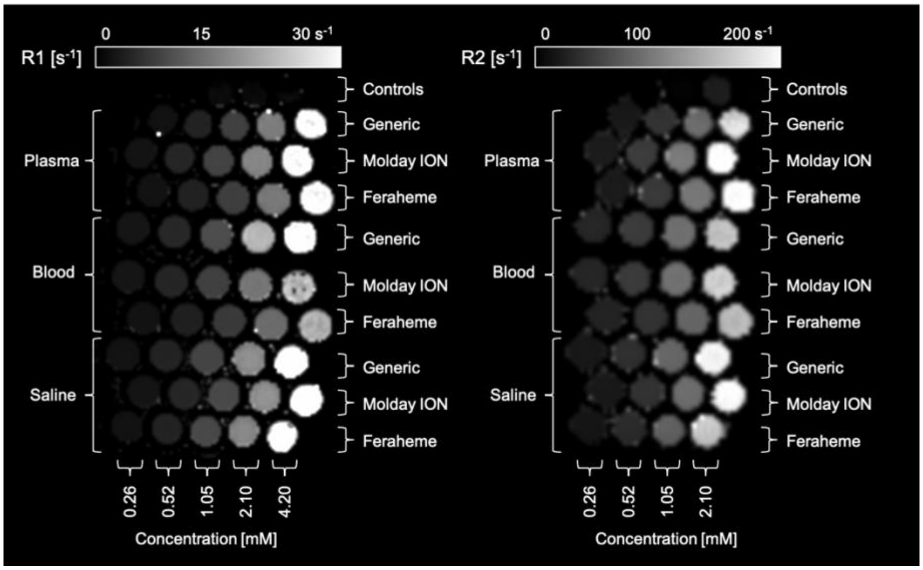

Figure 8.2. Grayscale pixelwise R1 and R2 maps of phantoms consisting of Feraheme, Molday ION and generic ferumoxytol in saline, whole blood, and plasma (3.0T, coronal view) across contrast concentration range of 0.26-4.20 mM.

In vivo MRI performance of Molday ION, Feraheme, and generic ferumoxytol

No contrast-related hypotension (defined as a decrease in systolic blood pressure of >20mmHg) occurred within 6-8 hours post contrast administration. We observed a mean heart rate (HR) of 91±13 bpm, systolic blood pressure (SBP) of 98±5 mmHg, and diastolic blood pressure (DBP) of 58±5 mmHg in the Molday ION group and a mean HR of 83±6 bpm, SBP of 92±11 mmHg, and DBP of 59±11 mmHg in the Feraheme group.

Based on LV blood pool T1 measurements sampled at 1-minute intervals for 10 minutes after contrast injection, Molday ION and Feraheme reached intravascular imaging steady-state between 5-6 minutes. We found the imaging performance of Molday ION, Feraheme, and generic ferumoxytol at 3.0T using T1w (MUSIC, VIBE) and T2w (HASTE) imaging pulse sequences to be similar. MUSIC images acquired with all three USPIOs show similar positive contrast enhancement (Figure 8.3). On T1w 3D-VIBE, Molday ION, Feraheme, and generic ferumoxytol all show the expected positive contrast enhancement of liver, spleen, cardiac chambers and blood vessels (Figure 8.4). Figure 8.5 shows representative pre- and post-contrast coronal HASTE images with Molday ION, Feraheme, and generic ferumoxytol. Post-Molday ION HASTE images of the liver showed the expected negative contrast enhancement and low signal from the vascular liver parenchyma (SNR 8.8±5.8) with low liver-blood pool contrast (CNR 0.1±5.6). On VIBE and HASTE images, the SNR (liver, spleen, skeletal muscle, and blood pool), and CNR (liver, spleen, and skeletal muscle relative to blood) are similar across all three agents (Table 8.2).

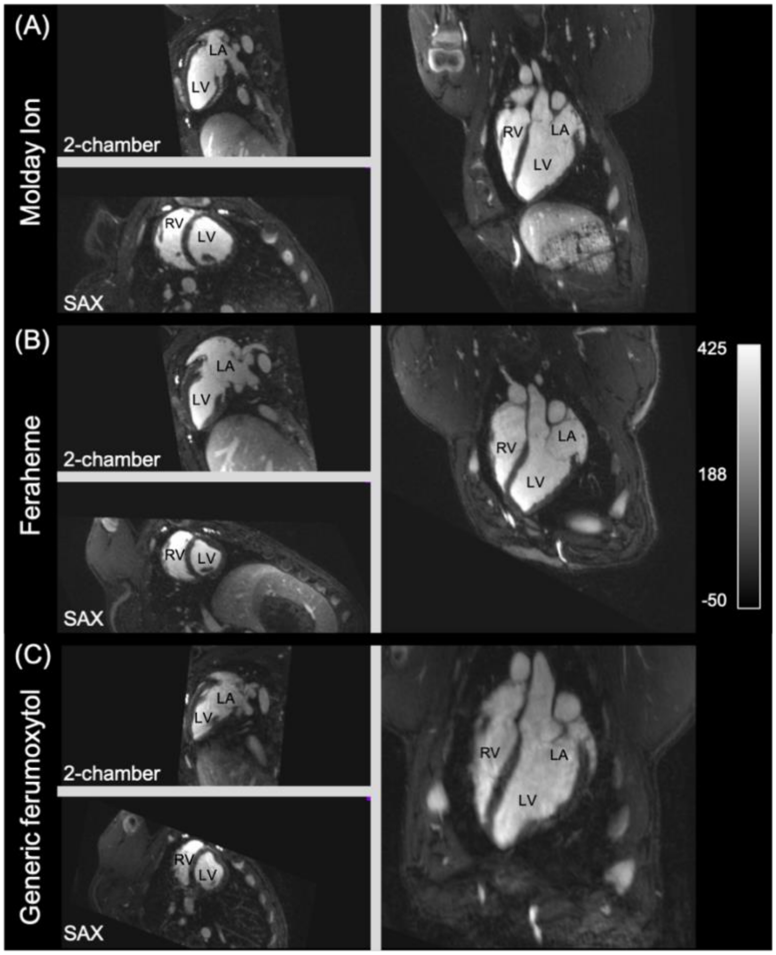

Figure 8.3. Contrast-enhanced multiplanar reformatted images belonging to two swine acquired using the multiphase, steady-state imaging with contrast (MUSIC) pulse sequence at 3.0T, after administration of (A) Molday ION 4.0 mg/kg, (B) Feraheme 4.0mg/kg, (C) generic ferumoxytol 4.0mg/kg.

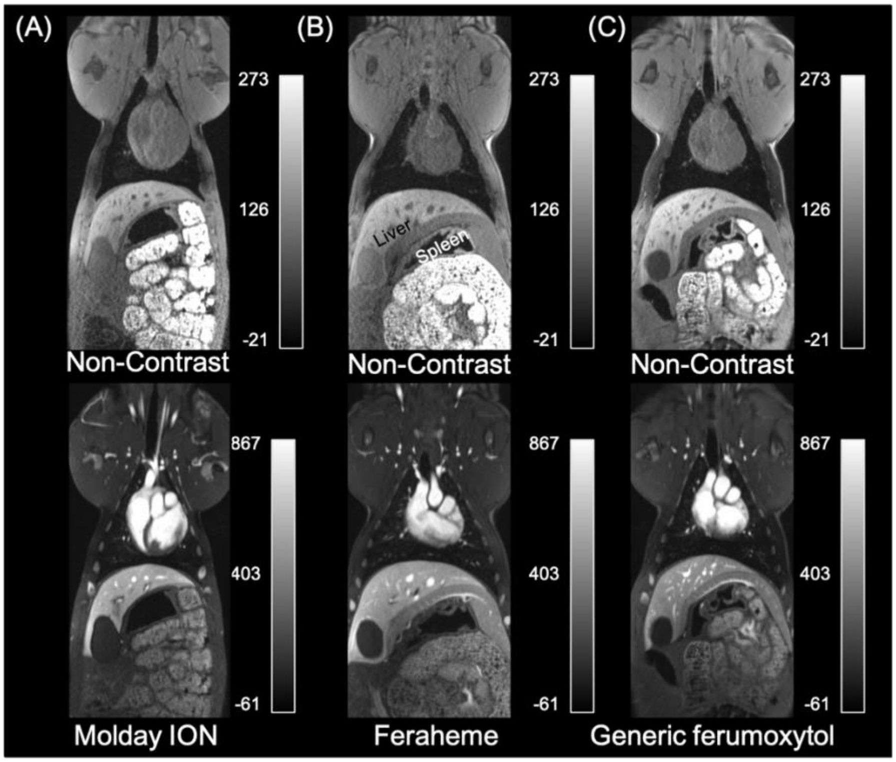

Figure 8.4. Non-contrast and contrast-enhanced coronal multiplanar reformatted images belonging to two swine and acquired using the Volumetric Interpolated Breath-hold Exam (VIBE) pulse sequence at 3.0T.

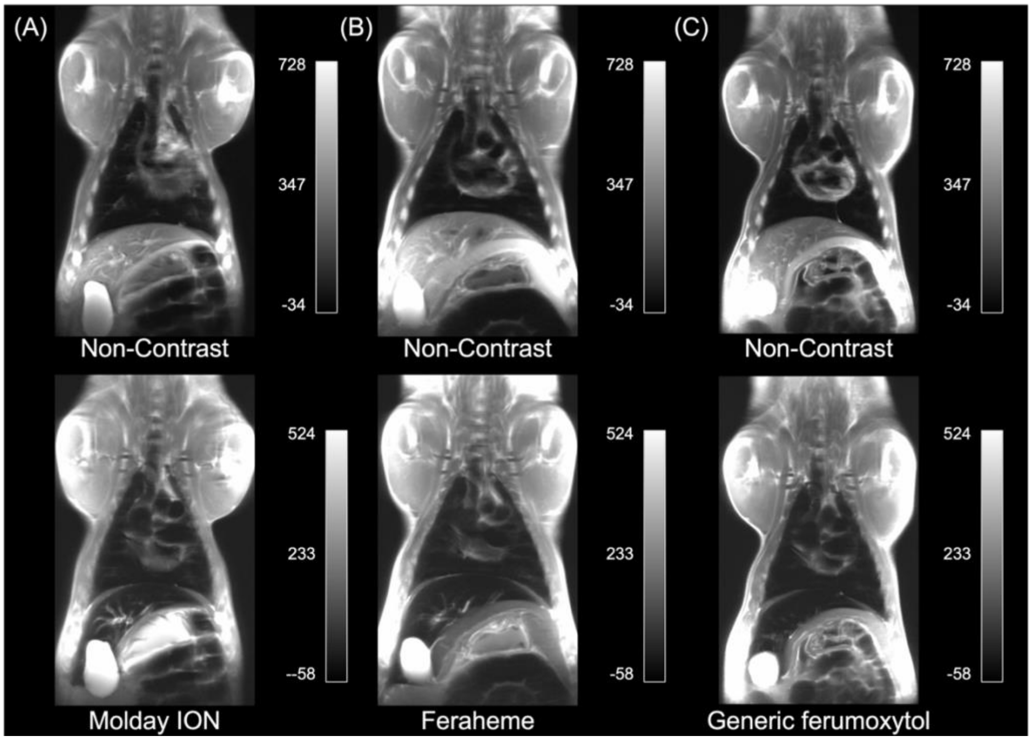

Figure 8.5. Non-contrast and contrast-enhanced coronal images belonging to two swine and acquired using Half-Fourier-Acquired Single-shot Turbo spin Echo (HASTE) at 3.0T.

Table 8.2. SNR and CNR of HASTE and VIBE images with Molday ION contrast.

	T2w HASTE*			**T1w VIBE***		
Tissue	Feraheme	Molday ION	Generic Ferumoxytol	Feraheme	Molday ION	Generic Ferumoxytol
Signal-to-noise ratio (SNR)						
Blood	8.3	8.6±4	9.6	482.8	459.1±171.8	723.9
Muscle	69.9	57.5±33.9	72.9	147.4	123.9±41.2	127.2
Liver	6.3	8.8±5.8	7.3	310.3	317.5±149.6	365.1
Spleen	34.8	49.6±45.7	83.4	261.8	285.9±128.9	279.2
Contrast-to-noise ratio (CNR)						
Muscle	61.6	48.9±32.7	66.4	-335.3	-335.2±133.8	-596.8
Liver	-2.0	0.1±5.6	0.8	-172.5	-141.6±29.9	-358.9
Spleen	26.5	41±45.5	76.8	-221.0	-173.2±52.5	-444.8

*SNR of blood pool (descending aorta), longissimus (skeletal) muscle, liver, and spleen from regions of interest drawn on coronal HASTE and axial VIBE images. The Feraheme, Molday ION, and generic ferumoxytol contrast dose was 4.0 mg/kg. CNR of longissimus muscle, liver, and spleen relative to blood pool were calculated based on signal intensity measurements from regions of interest on post-contrast HASTE and VIBE images. HASTE, Half-Fourier-Acquired Single-shot Turbo spin Echo; VIBE, Volumetric Interpolated Breath-hold Exam

For functional, quantitative MRI using MOLLI T1 mapping, all three USPIOs showed closely comparable post-contrast T1 shortening. Across all swine subjects, we found a mean Molday ION-enhanced T1 of 103±16 ms in the LV blood pool and 832±107 ms in the myocardium. We observed similar T1 values with Feraheme (LV blood pool: 112 ms [109, 119 ms]; myocardium: 860±47 ms) and generic ferumoxytol (LV blood pool: 94±2.5 ms; myocardium: 764±16 ms). Overall, Molday ION induced a mean ΔT1 shortening ($\Delta T1(\%) = (T1_{post} - T1_{pre})*100$) of -94.7±0.7% and -40.8±6.3% in the LV blood pool and myocardium.

Feraheme induced a median ΔT1 shortening of -94.2% (-94.4, -93.7) and -38.3±3.2%, respectively. Generic ferumoxytol caused a mean ΔT1 of -95±0.0% and -43±1.4% in the LV blood pool and myocardium. Two-way ANOVA found no significant difference in myocardial T1 (p=0.08) or blood pool T1 (p=0.933) between Molday ION and Feraheme.

As a method to map the fractional intravascular distribution volume in solid tissues, T1 mapping with the three USPIOs produced similar fMBV (Figure 8.6) in normal swine models. We found a median fMBV of 8.7% (7.4, 10.6%) in normal swine imaged with Molday ION (N=4 swine, 64 segments), a mean fMBV of 8.6±2.2% when imaged with Feraheme (N=5 swine, 80 segments), and a mean fMBV of 6.7±1.5% (N=1 swine, 16 segments) with generic ferumoxytol. No significant difference in fMBV between the Molday ION and Feraheme groups (p=0.13) was observed. In the Molday ION group, we found a mean FBV of 44.1±7.5% in the liver and 23.9±5.5% in the spleen. With Feraheme, we observed a mean FBV of 58.8% in the liver and 17.1% in the spleen. With generic ferumoxytol, we computed a mean FBV of 58.8% in the liver and 15.9% in the spleen.

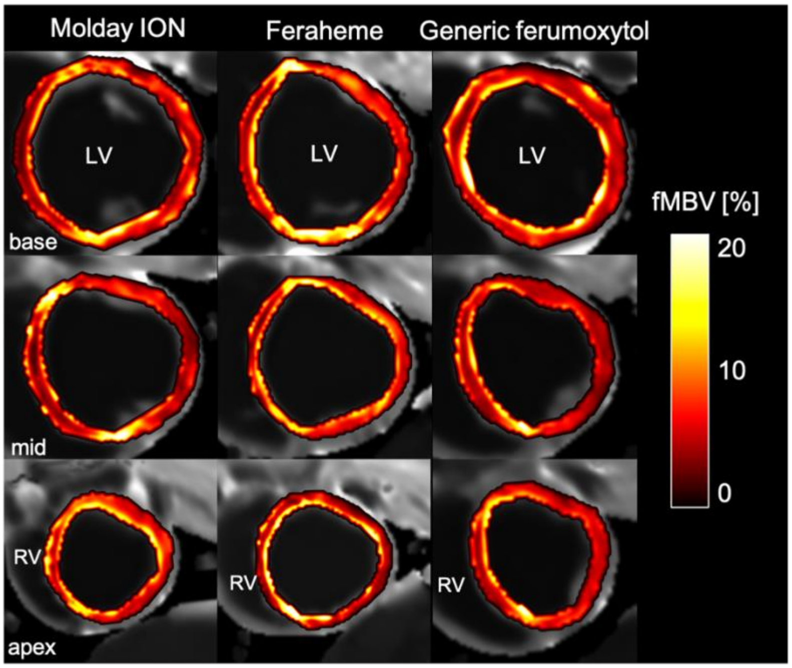

Figure 8.6. Representative pixel-wise fractional myocardial blood volume (fMBV) maps of the left ventricular (LV) short-axis in normal swine. The fBMV maps are computed from MOLLI T1 images acquired at steady-state contrast administration of Molday ION (left panel, 4mg/kg), Feraheme (center panel), 4mg/kg), or generic ferumoxytol (right panel, 4 mg/kg).

8.4 Discussion

Although Feraheme has proven advantages for off-label diagnostic MRI, its widespread use is limited by availability and cost. The recent availability of generic ferumoxytol and pre-clinical development of Molday ION offer additional potential alternatives for USPIO-enhanced MRI. We compared the in vitro and in vivo MRI performance of these three agents. Feraheme, generic ferumoxytol, and Molday ION have nearly identical r1 and similar r2 relaxivities in saline, human plasma, and human blood at 3.0T ($p>0.05$). SNR and CNR values of post-contrast images acquired using VIBE and HASTE pulse sequences are indistinguishable. Relative to both ferumoxytol formulations, Molday ION produced the expected positive T1 contrast on T1w pulse sequences (4D MUSIC and VIBE), and the expected negative T2 contrast on T2w HASTE images in healthy swine. All three agents also produced comparable blood T1 shortening and similar fractional intravascular contrast distribution volume in myocardium, liver, and spleen of normal swine using MOLLI T1 mapping (all $p>0.05$).

The core diameter of a USPIO agent is closely coupled with its magnetic susceptibility, and consequently its relaxivity.[134] The iron oxide crystallite core is complexed with a low molecular weight semi-synthetic carbohydrate shell. These are attractive features for applications that enable theranostic use. Relative to both ferumoxytol formulations, Molday ION has a slightly lower particle size range (17-32 nm) with a shorter expected intravascular half-life due to its lower zeta potential (-4.8 mV) (Molday ION package insert, BioPAL). Our study however, did not directly address the relative blood half-lives of the respective agents, other than to confirm that all agents produced enhancement that did not change distinguishably over the time interval encompassed by the imaging studies. Feraheme has a mean hydrodynamic diameter of 30 nm,[6] and a stated intravascular half-life of 10-14 hours.[7] While not identical to those of Knobloch et al., our in vitro relaxometry results for Feraheme demonstrate similar r1 and r2 relaxivity in saline and plasma at 3.0T. We observed an r1 relaxivity of 8.09 ± 0.13 $mM^{-1}s^{-1}$ in saline and 6.74 ± 0.02 $mM^{-1}s^{-1}$ in plasma at 22° C, while Knobloch et al report values of 10.0 ± 0.3 $mM^{-1}s^{-1}$ and 9.5 ± 0.2 $mM^{-1}s^{-1}$ at 37° C.[8] Both studies show a nonlinear relationship between contrast concentration and blood R1 at contrast concentrations above 2.1mM. Our methods differed from those used by Knobloch et al in several ways. Although the magnet strengths were both 3.0T, the manufacturers were different. We also imaged our sample tubes in air at ambient temperature (22° C), while Knobloch et al. maintained their samples at 37° C.[8] Finally, our MRI parameters were optimized to improve SNR in inversion-recovery spin echo images based on a preliminary study. We used a longer TR (3000 ms) and shorter TE (5 ms) in our inversion-recovery spin echo acquisition, and a longer minimum TE and broader echo spacing in our multi-contrast spin echo acquisition. Importantly, our results indicate closely comparable relaxivity of our three chosen USPIOs within the diagnostic imaging dose range for the pulse sequence parameters listed, which suggests that the agents can likely be used interchangeably in vivo.

Linearity of MRI contrast agent relaxation rates (R1 and R2), corresponding to constant r1 and r2 relaxivities over the diagnostic dose range, is an important assumption made by many pharmacologic models.[135,136] For a theoretical 75 kg patient with a total circulating blood volume of 5 liters, a ferumoxytol dose of 4.0 mg/kg maps to a blood concentration of approximately 1 milli mole per liter (mmol/L) or 1mM. The concentrations used in our in-vitro imaging study range from 0.26 – 4.20 mM, or a corresponding in vivo dose range of approximately 1 mg/kg to 16 mg/kg. Our relaxometry study and previous work[8] indicate largely linear R1 and R2 with contrast concentration up to 8 mg/kg, twice the maximum dose used in our in-vivo swine study and for typical off-label diagnostic purposes in patients.[137] Our observation of nonlinear R1 and R2 at high contrast concentrations (well above the typical diagnostic dose) aligns with previously published results.[8] This effect has been proposed to be related to two factors.[8] Iron contrast is compartmentalized within the extracellular space in the blood samples, whereas in the saline and plasma samples, it is distributed homogeneously throughout the medium. The compartmentalization of contrast results in two populations of water molecules which occupy distinct relaxation environments, which contribute to increasingly heterogeneous magnetization within a given voxel. Water is also compartmentalized in the blood samples, though it diffuses across the cell membrane. At increased contrast concentrations, water is increasingly compartmentalized within the extracellular and intracellular spaces; thereby decreasing the apparent R1 and R2 of the voxel.[8]

T1w 3D-VIBE or 4D-MUSIC bright-blood imaging pulse sequences may be combined with T2w 2D-HASTE dark-blood imaging to show complementary features on MRI exams. The signal from native blood pool on HASTE images is highly variable, due to the complex interplay between radiofrequency pulses and pulsatile blood flow through and within the slice.[138] Although many technically sophisticated methods exist to suppress blood signal on MR images, the results can be unreliable and technique dependent. Feraheme has been shown to suppress intraluminal blood signal reliably on HASTE images without any magnetization preparation or flow dephasing maneuvers, based purely on T2 effects.[12] Our results from the current in vivo studies indicate that Molday ION performs comparably to both formulations of ferumoxytol and shows promise as a viable candidate for further exploration.

While gadolinium-based contrast agents (GBCAs) are powerful and have proven value over a wide range of diagnostic applications, there are persistent concerns about long term tissue deposition even in the setting of normal kidney function.[123] Despite diminished concerns about nephrogenic systemic fibrosis in patients with impaired renal function, rare occurrence could be fatal and the mechanisms remain ill-defined.[4] Additionally, in the context of pharmacokinetic models, using true intravascular contrast agents can eliminate the need to account for contrast leakage into the extravascular space.[38] Intravascular USPIOs and extravasating GBCAs also have the potential to be used in concert for complementary applications and is a topic of ongoing work in our lab.

This work has several limitations. Our measurements were made at 3.0T and extrapolation to other field strengths can only be inferred. R2 estimation was performed following a multi-echo spin echo acquisition. A notable limitation of this technique is its sensitivity to signal perturbation due to stimulated echoes. We fit for R2 over 9 TE times chosen to minimize R2 error due to stimulated echoes at short TEs and the signal noise floor at long TEs. While a classical spin echo acquisition provides superior accuracy of T2 and R2 estimation, for the purpose of comparing relative apparent r2 relaxivity constants among the three USPIO agents in order to determine the interchangeability for in-vivo imaging, the multi-echo spin echo method and the respective fitting strategy are sufficient. While Molday ION shows promise as an intravascular imaging agent in an in-vivo study of normal swine models, no human data are yet available. In the meantime, significant further work will be required to characterize the biodistribution and metabolism of Molday ION, its biological half-life, the optimal dose for various applications, and its overall safety profile before it may be considered for use in human subjects. Intravenous iron agents carry a risk of minor infusion reactions including chest or lumbar discomfort and flushing.[10] Although Feraheme has been associated with serious adverse events including fatalities at therapeutic doses (510 mg Fe) administered as a bolus infusion over 17 seconds,[139] its safety profile for off-label diagnostic MRI in multicenter settings has been favorable to date.[10]

8.5 Conclusion

Relative to clinically approved ferumoxytol formulations, Molday ION demonstrates similar in-vitro magnetic properties and comparable in-vivo MRI characteristics in swine at 3.0T. Molday ION shows promise as a candidate for further testing, development, and possible use in humans as a more widely available alternative to ferumoxytol.

Chapter 9 **Conclusions**

Emerging quantitative imaging biomarkers of ischemic heart disease have the potential to reshape clinical cardiovascular care. However, significant knowledge gaps and practical hurdles exist within cardiovascular translational imaging research. The novel preclinical animal model using percutaneously delivered intracoronary implants described in this work offers a success rate comparable to that of open-chest delivery of ameroid constrictors, allowing for more rapid and cost-effective studies of novel diagnostic MR imaging methods for IHD. It enabled a subsequent investigation of quantitative MRI stress testing, indicating that ferumoxytol contrast improves the diagnostic performance of T1 reactivity as a measure of myocardial ischemia. This work has shown that a two-compartment model is feasible for estimation of fMBV using steady-state MOLLI T1 mapping over multiple ferumoxytol doses, and has the potential to image ischemia at rest, minimizing the patient discomfort and occasional serious side effects that result from stress testing. The technical developments in the areas of image registration and parametric mapping within our image processing pipeline have shifted the current state of pixelwise fMBV mapping toward a more integrated in-line approach. Finally, our investigation of the in-vitro and in-vivo MRI performance of Molday ION and a ferumoxytol generic demonstrates that these alternatives have strong potential as Feraheme alternatives and may help to relieve the limited availability and high cost of intravascular MRI contrast agents which continues to limit the adoption of USPIO-based techniques. The technical developments and investigations detailed in this work all contribute to improving the availability of high-quality noninvasive cardiac MRI for ischemic heart disease.

In addition to investigating novel imaging biomarkers of heart disease, this work helps to highlight existing knowledge gaps and future research directions. A novel swine model of acute myocardial hypoperfusion can be used in future studies to evaluate other diagnostic MR imaging methods for IHD. Outside the realm of translational imaging research, this swine model could be used for physiology studies investigating the effect of multiple sequential stenoses, or stenoses in multiple arterial branches. Further investigation of implant materials, dimensions, and surface coatings could improve the adaptability of our 3D printed intracoronary implants for a range of applications within IHD research. Fractional myocardial blood volume estimation with intravascular agents remains a nascent field of CMR research. Following further validation in a large-scale clinical study, model-fitted fMBV may serve as a potential direct marker of myocardial tissue perfusion. This validation in patients with chronic ischemic heart disease will be needed to fully characterize the distribution of fMBV in ischemic and remote myocardial regions. Finally, significant further testing and development of Molday ION for possible use in humans will be necessary if it is to become a more widely available alternative to ferumoxytol.

APPENDIX 1

Appendix 1.1. MRI acquisition parameters for in vitro r1 and r2 relaxometry at 3.0T

Parameters	Inversion-recovery turbo spin echo	Multi-echo spin echo
TI [ms]	50, 57, 65, 75, 119, 188, 300, 488, 669, 1000	N/A
TE [ms]	7.1	14.2, 21.3, 28.4, 35.5, 42.6, 49.7, 56.8, 63.9, 71
TR [ms]	3000	2000
Number of echoes	1	14
Flip angle [degrees]	180, 90	90,180
Bandwidth [Hz/pixel]	1532	1953
Resolution [mm]	2.14 x 2.14 x 10	3.20 x 3.20 x 10

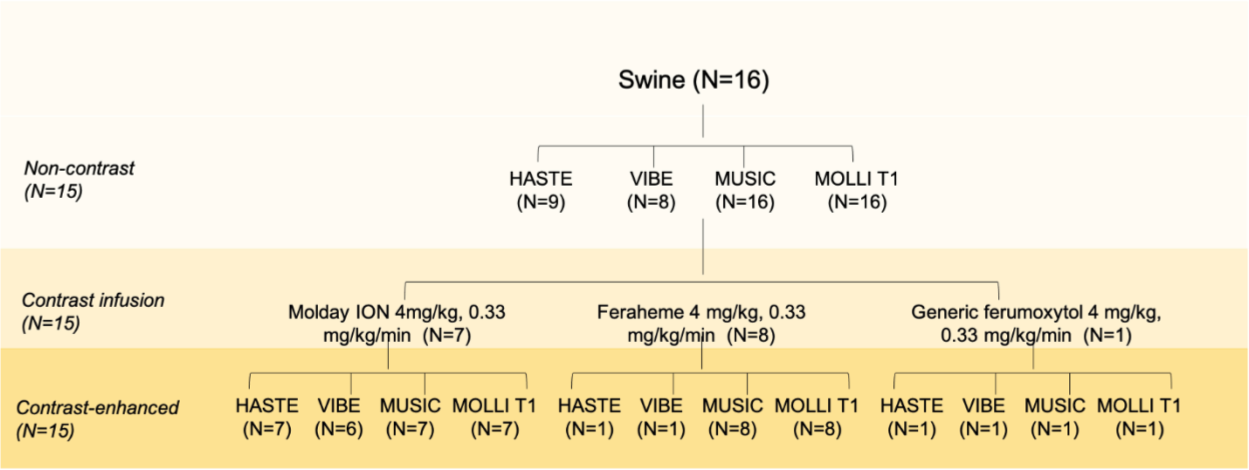

Appendix 1.2. Flow chart for in-vivo MRI of swine. Molday ION (BioPal), Feraheme (AMAG), or generic ferumoxytol (Sandoz) 4mg/kg were administered to swine. Pre- and post-contrast imaging at 3.0T were performed using T1-weighted and T2-weighted pulse sequences. T1-weighted pulse sequences include 4D MUSIC (Multiphase Steady-state Imaging with Contrast), 3D VIBE (Volumetric Interpolated Breath-hold Exam), and MOLLI (Modified Look-Locker Inversion) T1 mapping. T2-weighted pulse sequence included HASTE (Half-Fourier-Acquired Single-shot Turbo-spin Echo).

Appendix 1.3. MRI acquisition parameters for HASTE, VIBE, MUSIC, and MOLLI T1 at 3.0T

Parameters	HASTE	VIBE	MUSIC	MOLLI T1
TI [ms]	----	----	----	100 - 180
TE [ms]	72	0.92	1.19	1.08
TR [ms]	4000	2.91	18.2	2.6
Flip angle [degrees]	150	15	12	35
Cardiac phases	----	----	15-16	----
Bandwidth [Hz/pixel]	515	620	----	1085
Resolution [mm^3]	0.98 x 0.98 x 8	1.0 x 1.0 x1.8	1.0 x 1.0 x 1.0	0.6 x 0.9 x 8
Acceleration factor	iPAT 2	iPAT 4	3 6/8 Fourier in phase- and slice-encoding directions	iPAT 2

REFERENCES

1. Cardiovascular Diseases | Division of Global Health Protection | Global Health | CDC.https://www.cdc.gov/globalhealth/healthprotection/ncd/cardiovascular-diseases.html.
2. Wu Z hong, Sun L ping, Liu Y long, et al. Fully Automatic Scar Segmentation for Late Gadolinium Enhancement MRI Images in Left Ventricle with Myocardial Infarction. *Curr Med Sci*. 2021;41(2):398-404.
3. McDonald RJ, Levine D, Weinreb J, et al. Gadolinium retention: A research roadmap from the 2018 NIH/ACR/RSNA workshop on gadolinium chelates. *Radiology*. 2018;289(2):517-534.
4. Fraum TJ, Ludwig DR, Bashir MR, Fowler KJ. Gadolinium-based contrast agents: A comprehensive risk assessment. *J Magn Reson Imaging*. 2017;46(2):338-353.
5. Gulani V, Calamante F, Shellock FG, Kanal E, Reeder SB. Gadolinium deposition in the brain: summary of evidence and recommendations. *Lancet Neurol*. 2017;16(7):564-570.
6. Bullivant JP, Zhao S, Willenberg BJ, Kozissnik B, Batich CD, Dobson J. Materials characterization of feraheme/ferumoxytol and preliminary evaluation of its potential for magnetic fluid hyperthermia. *Int J Mol Sci*. 2013;14(9):17501-17510.
7. Li W, Tutton S, Vu AT, et al. First-pass contrast-enhanced magnetic resonance angiography in humans using ferumoxytol, a novel ultrasmall superparamagnetic iron oxide (USPIO)-based blood pool agent. *J Magn Reson Imaging*. 2005;21(1):46-52.
8. Knobloch G, Colgan T, Wiens CN, et al. Relaxivity of Ferumoxytol at 1.5 T and 3.0 T. *Invest Radiol*. 2018;53(5):257-263.
9. Chen C, Ge J, Gao Y, et al. Ultrasmall superparamagnetic iron oxide nanoparticles: A next

generation contrast agent for magnetic resonance imaging. *Wiley Interdiscip Rev Nanomedicine Nanobiotechnology*. 2022;14(1):1-22.

10. Nguyen KL, Yoshida T, Kathuria-Prakash N, et al. Multicenter Safety and Practice for Off-Label Diagnostic Use of Ferumoxytol in MRI. *Radiology*. 2019;293(3):554-564.
11. Han F, Rapacchi S, Khan S, et al. Four-dimensional, multiphase, steady-state imaging with contrast enhancement (MUSIC) in the heart: A feasibility study in children. *Magn Reson Med*. 2015;74(4):1042-1049.
12. Nguyen KL, Park EA, Yoshida T, Hu P, Finn JP. Ferumoxytol enhanced black-blood cardiovascular magnetic resonance imaging. *J Cardiovasc Magn Reson*. 2017;19(106).
13. Stirrat CG, Alam SR, MacGillivray TJ, et al. Ferumoxytol-enhanced magnetic resonance imaging assessing inflammation after myocardial infarction. *Heart*. 2017;103(19):1528-1535.
14. Ramasawmy R, Rogers T, Alcantar MA, et al. Blood volume measurement using cardiovascular magnetic resonance and ferumoxytol: preclinical validation. *J Cardiovasc Magn Reson*. 2018;20(1).
15. Knobloch G, Colgan T, Schiebler ML, et al. Comparison of gadolinium-enhanced and ferumoxytol-enhanced conventional and UTE-MRA for the depiction of the pulmonary vasculature. *Magn Reson Med*. 2019;82(5):1660-1670.
16. Colbert CM, Le AH, Shao J, et al. Ferumoxytol-enhanced magnetic resonance T1 reactivity for depiction of myocardial hypoperfusion. *NMR Biomed*. 2021;34(7).
17. Hollowed JJ, Colbert CM, Currier JW, Nguyen KL. Novel Percutaneous Approach for Deployment of 3D Printed Coronary Stenosis Implants in Swine Models of Ischemic Heart Disease. *J Vis Exp*. Published online 2020:e60729.

18. Colbert CM, Shao J, Hollowed JJ, et al. 3D-Printed Coronary Implants Are Effective for Percutaneous Creation of Swine Models with Focal Coronary Stenosis. *J Cardiovasc Transl Res*. 2020;13(6):1033-1043.
19. Nguyen KL, Shao J, Ghodrati VK, et al. Ferumoxytol-Enhanced CMR for Vasodilator Stress Testing: A Feasibility Study. *JACC Cardiovasc Imaging*. 2019;12(8):1582-1584.
20. Elkholy KO, Hegazy O, Okunade A, Aktas S, Ajibawo T. Regadenoson Stress Testing: A Comprehensive Review With a Focused Update. *Cureus*. 2021;13(1).
21. McCommis KS, Zhang H, Goldstein TA, et al. Myocardial blood volume is associated with myocardial oxygen consumption: an experimental study with cardiac magnetic resonance in a canine model. *JACC Cardiovasc Imaging*. 2009;2(11):1313-1320.
22. Lindner JR, Skyba DM, Goodman NC, Jayaweera AR, Kaul S. Changes in myocardial blood volume with graded coronary stenosis. *Am J Physiol*. 1997;272(1):H567-575.
23. Wu CC, Feldman MD, Mills JD, et al. Myocardial contrast echocardiography can be used to quantify intramyocardial blood volume: New insights into structural mechanisms of coronary autoregulation. *Circulation*. 1997;96(3):1004-1011.
24. Bane O, Lee DC, Benefield BC, et al. Leakage and water exchange characterization of gadofosveset in the myocardium. *Magn Reson Imaging*. 2014;32(3):224-235.
25. Feher A, Sinusas AJ. Quantitative Assessment of Coronary Microvascular Function: Dynamic Single-Photon Emission Computed Tomography, Positron Emission Tomography, Ultrasound, Computed Tomography, and Magnetic Resonance Imaging. *Circ Cardiovasc Imaging*. 2017;10(8).
26. Higgins DM, Ridgway JP, Sivananthan MU, Radjenovic A, Messroghli DR, Kozerke S. Modified Look-Locker inversion recovery (MOLLI) for high-resolution T1 mapping of

the heart. *Magn Reson Med*. 2004;52(1):141-146.

27. Chow K, Flewitt JA, Green JD, Pagano JJ, Friedrich MG, Thompson RB. Saturation recovery single-shot acquisition (SASHA) for myocardial T1 mapping. *Magn Reson Med*. 2014;71(6):2082-2095.

28. Piechnik SK, Ferreira VM, Dall'Armellina E, et al. Shortened Modified Look-Locker Inversion recovery (ShMOLLI) for clinical myocardial T1-mapping at 1.5 and 3 T within a 9 heartbeat breathhold. *J Cardiovasc Magn Reson*. 2010;12(1):69.

29. Weingärtner S, Akçakaya M, Basha T, et al. Combined saturation/inversion recovery sequences for improved evaluation of scar and diffuse fibrosis in patients with arrhythmia or heart rate variability. *Magn Reson Med*. 2014;71(3):1024-1034.

30. Shao J, Liu D, Sung K, Nguyen KL, Hu P. Accuracy, precision, and reproducibility of myocardial T1 mapping: A comparison of four T1 estimation algorithms for modified look-locker inversion recovery (MOLLI). *Magn Reson Med*. 2017;78(5):1746-1756.

31. Kellman P, Hansen MS. T1-mapping in the heart: Accuracy and precision. *J Cardiovasc Magn Reson*. 2014;16(1):1-20.

32. Kellman P, Arai AE, Xue H. T1 and extracellular volume mapping in the heart: Estimation of error maps and the influence of noise on precision. *J Cardiovasc Magn Reson*. 2013;15(1):1-12.

33. Shao J, Nguyen KL, Natsuaki Y, Spottiswoode B, Hu P. Instantaneous signal loss simulation (InSiL): An improved algorithm for myocardial T1 mapping using the MOLLI sequence. *J Magn Reson Imaging*. 2015;41(3):721-729.

34. Shao J, Rapacchi S, Nguyen KL, Hu P. Myocardial T1 mapping at 3.0 tesla using an inversion recovery spoiled gradient echo readout and bloch equation simulation with slice

profile correction (BLESSPC) T1 estimation algorithm. *J Magn Reson Imaging*. 2016;43(2):414-425.

35. Weingärtner S, Meßner NM, Budjan J, et al. Myocardial T1-mapping at 3T using saturation-recovery: reference values, precision and comparison with MOLLI. *J Cardiovasc Magn Reson*. 2016;18(1):84.

36. van Assen M, van Dijk R, Kuijpers D, Vliegenthart R, Oudkerk M. T1 reactivity as an imaging biomarker in myocardial tissue characterization discriminating normal, ischemic and infarcted myocardium. *Int J Cardiovasc Imaging*. 2019;35(7):1319-1325.

37. Piechnik SK, Neubauer S, Ferreira VM. State-of-the-art review: stress T1 mapping—technical considerations, pitfalls and emerging clinical applications. *Magn Reson Mater Physics, Biol Med*. 2018;31(1):131-141.

38. Peters AM. Fundamentals of tracer kinetics for radiologists. *Br J Radiol*. 1998;71(851):1116-1129.

39. Koh TS, Bisdas S, Koh DM, Thng CH. Fundamentals of tracer kinetics for dynamic contrast-enhanced MRI. *J Magn Reson Imaging*. 2011;34(6):1262-1276.

40. Ewing JR, Bagher-Ebadian H. Model selection in measures of vascular parameters using dynamic contrast-enhanced MRI: Experimental and clinical applications. *NMR Biomed*. 2013;26(8):1028-1041.

41. Le DE, Bin JP, Coggins MP, Wei K, Lindner JR, Kaul S. Relation between myocardial oxygen consumption and myocardial blood volume: A study using myocardial contrast echocardiography. *J Am Soc Echocardiogr*. 2002;15(9):857-863.

42. Möhlenkamp S, Behrenbeck TR, Lerman A, et al. Coronary microvascular functional reserve: Quantification of long-term changes with electron-beam CT - Preliminary results

in a porcine model. *Radiology*. 2001;221(1):229-236.

43. McCommis KS, Goldstein TA, Abendschein DR, et al. Roles of myocardial blood volume and flow in coronary artery disease: an experimental MRI study at rest and during hyperemia. *Eur Radiol*. 2010;20(8):2005-2012.

44. Hazlewood CF, Chang DC, Nichols BL, Woessner DE. Nuclear Magnetic Resonance Transverse Relaxation Times of Water Protons in Skeletal Muscle. *Biophys J*. 1974;14(3):583-606.

45. Donahue KM, Weisskoff RM, Chesler DA, et al. Improving MR quantification of regional blood volume with intravascular T1 contrast agents: Accuracy, precision, and water exchange. *Magn Reson Med*. 1996;36(6):858-867.

46. Bashir MR, Bhatti L, Marin D, Nelson RC. Emerging applications for ferumoxytol as a contrast agent in MRI. *J Magn Reson Imaging*. 2015;41(4):884-898.

47. Bane O, Lee DC, Benefield BC, et al. Leakage and water exchange characterization of gadofosveset in the myocardium. *Magn Reson Imaging*. 2014;32(3):224-235.

48. Schwarzbauer C, Morrissey SP, Deichmann R, et al. Quantitative magnetic resonance imaging of capillary water permeability and regional blood volume with an intravascular MR contrast agent. *Magn Reson Med*. 1997;37(5):769-777.

49. Bjørnerud A, Bjerner T, Johansson LO, Ahlström HK. Assessment of myocardial blood volume and water exchange: Theoretical considerations and in vivo results. *Magn Reson Med*. 2003;49(5):828-837.

50. Sobol WT, Jackels SC, Cothran RL, Hinson WH. NMR spin-lattice relaxation in tissues with high concentration of paramagnetic contrast media: Evaluation of water exchange rates in intact rat muscle. *Med Phys*. 1991;18(2):243-250.

51. Wedeking P, Sotak CH, Telser J, Kumar K, Chang CA, Tweedle MF. Quantitative dependence of MR signal intensity on tissue concentration of Gd(HP-DO3A) in the nephrectomized rat. *Magn Reson Imaging*. 1992;10(1):97-108.

52. Donahue KM, Burstein D, Manning WJ, Gray ML. Studies of Gd-DTPA relaxivity and proton exchange rates in tissue. *Magn Reson Med*. 1994;32(1):66-76.

53. Byrd RH, Gilbert JC, Nocedal J. A trust region method based on interior point techniques for nonlinear programming. *Math Program Ser B*. 2000;89(1):149-185.

54. Waltz RA, Morales JL, Nocedal J, Orban D. An interior algorithm for nonlinear optimization that combines line search and trust region steps. *Math Program*. 2006;107(3):391-408.

55. Ugray Z, Lasdon L, Plummer J, Glover F, Kelly J, Marti R. Scatter search and local NLP solvers: A multistart framework for global optimization. *INFORMS J Comput*. 2007;19(3):328-340.

56. Ratkowsky DA. Principles of nonlinear regression modeling. *J Ind Microbiol*. 1993;12(3-5):195-199.

57. Colbert CM, Thomas MA, Yan R, et al. Estimation of fractional myocardial blood volume and water exchange using ferumoxytol-enhanced magnetic resonance imaging. *J Magn Reson Imaging*. 2021;53(6):1699-1709.

58. Huizinga W, Poot DHJ, Guyader JM, et al. PCA-based groupwise image registration for quantitative MRI. *Med Image Anal*. 2016;29:65-78.

59. Tao Q, van der Tol P, Berendsen FF, Paiman EHM, Lamb HJ, van der Geest RJ. Robust motion correction for myocardial T 1 and extracellular volume mapping by principle component analysis-based groupwise image registration. *J Magn Reson Imaging*.

2018;47(5):1397-1405.

60. Keeran KJ, Jeffries KR, Zetts AD, Taylor J, Kozlov S, Hunt TJ. A Chronic Cardiac Ischemia Model in Swine Using an Ameroid Constrictor. *J Vis Exp*. 2017;(128).

61. Litvak J, Siderides LE, Vineberg AM. The experimental production of coronary artery insufficiency and occlusion. *Am Heart J*. 1957;53(4):505-518.

62. Hughes GC, Post MJ, Simons M, Annex BH. Translational Physiology: Porcine models of human coronary artery disease: implications for preclinical trials of therapeutic angiogenesis. *J Appl Physiol*. 2015;94(5):1689-1701.

63. Robich MP, Chu LM, Burgess TA, et al. Resveratrol preserves myocardial function and perfusion in remote nonischemic myocardium in a swine model of metabolic syndrome. *J Am Coll Surg*. 2012;215(5):681-689.

64. Robich MP, Osipov RM, Nezafat R, et al. Resveratrol improves myocardial perfusion in a swine model of hypercholesterolemia and chronic myocardial ischemia. *Circulation*. 2010;122(11 SUPPL. 1):S142-S149.

65. Sabe AA, Elmadhun NY, Robich MP, Dalal RS, Sellke FW. Does resveratrol improve insulin signaling in chronically ischemic myocardium? *J Surg Res*. 2013;183(2):531-536.

66. Giannopoulos AA, Mitsouras D, Yoo SJ, Liu PP, Chatzizisis YS, Rybicki FJ. Applications of 3D printing in cardiovascular diseases. *Nat Rev Cardiol*. 2016;13(12):701-718.

67. Oliveira-Santos M de, Oliveira-Santos E, Gonçalves L, Silva Marques J. Cardiovascular Three-Dimensional Printing in Non-Congenital Percutaneous Interventions. *Hear Lung Circ*. 2019;28(10):1525-1534.

68. Forte MNV, Hussain T, Roest A, et al. Living the heart in three dimensions: Applications

of 3D printing in CHD. *Cardiol Young*. 2019;29(6):733-743.

69. Alonzo M, AnilKumar S, Roman B, Tasnim N, Joddar B. 3D Bioprinting of cardiac tissue and cardiac stem cell therapy. *Transl Res*. 2019;211:64-83.

70. Lee W, Hong Y, Dai G. 3D bioprinting of vascular conduits for pediatric congenital heart repairs. *Transl Res*. 2019;211:35-45.

71. Shaw LJ, Berman DS, Maron DJ, et al. Optimal medical therapy with or without percutaneous coronary intervention to reduce ischemic burden: results from the Clinical Outcomes Utilizing Revascularization and Aggressive Drug Evaluation (COURAGE) trial nuclear substudy. *Circulation*. 2008;117(10):1283-1291.

72. Liu A, Wijesurendra RS, Liu JM, et al. Gadolinium-Free Cardiac MR Stress T1-Mapping to Distinguish Epicardial From Microvascular Coronary Disease. *J Am Coll Cardiol*. 2018;71(9):957-968.

73. Husso M, Nissi MJ, Kuivanen A, et al. Quantification of porcine myocardial perfusion with modified dual bolus MRI-A prospective study with a PET reference. *BMC Med Imaging*. 2019;19(1):1-11.

74. Fishbein MC, Meerbaum S, Rit J, et al. Early phase acute myocardial infarct size quantification: Validation of the triphenyl tetrazolium chloride tissue enzyme staining technique. *Am Heart J*. 1981;101(5):593-600.

75. Fieno DS, Kim RJ, Chen EL, Lomasney JW, Klocke FJ, Judd RM. Contrast-enhanced magnetic resonance imaging of myocardium at risk: Distinction between reversible and irreversible injury throughout infarct healing. *J Am Coll Cardiol*. 2000;36(6):1985-1991.

76. Foin N, Sen S, Petraco R, et al. Method for Percutaneously Introducing, and Removing, Anatomical Stenosis of Predetermined Severity In Vivo: The “Stenotic Stent.” *J*

Cardiovasc Transl Res. 2013;6(4):640-648.

77. Lindsey ML, Bolli R, Canty JM, et al. Guidelines for experimental models of myocardial ischemia and infarction. *Am J Physiol Heart Circ Physiol*. 2018;314(4):H812-H838.

78. Mahrholdt H, Wagner A, Judd RM, Sechtem U, Kim RJ. Delayed enhancement cardiovascular magnetic resonance assessment of non-ischaemic cardiomyopathies. *Eur Heart J*. 2005;26(15):1461-1474.

79. Liao J, Huang W, Liu G. Animal models of coronary heart disease. *J Biomed Res*. 2016;30(1):3-10.

80. Tanimoto A, Kawaguchi H, Yoshida H, et al. Microminipig, a Non-rodent Experimental Animal Optimized for Life Science Research: Novel Atherosclerosis Model Induced by High Fat and Cholesterol Diet. *J Pharmacol Sci*. 2011;115(2):115-121.

81. Krombach GA, Kinzel S, Mahnken AH, Günther RW, Buecker A. Minimally invasive close-chest method for creating reperfused or occlusive myocardial infarction in swine. *Invest Radiol*. 2005;40(1):14-18.

82. Wu M, Bogaert J, D'Hooge J, et al. Closed-chest animal model of chronic coronary artery stenosis. Assessment with magnetic resonance imaging. *Int J Cardiovasc Imaging*. 2010;26(3):299-308.

83. Rissanen TT, Nurro J, Halonen PJ, et al. The bottleneck stent model for chronic myocardial ischemia and heart failure in pigs. *Am J Physiol - Hear Circ Physiol*. 2013;305(9):1297-1308.

84. Kraitchman D, Bluemke D, Chin B, Heldman A. A minimally invasive method for creating coronary stenosis in a swine model for MRI and SPECT imaging. *Invest Radiol*. 2000;35(7):445-451.

85. Adams GJ, Baltazar U, Karmonik C, et al. Comparison of 15 different stents in superficial femoral arteries by high resolution MRI ex vivo and in vivo. *J Magn Reson Imaging*. 2005;22(1):125-135.

86. Gerber BL, Boston RC, Kraitchman DL, et al. Single-Vessel Coronary Artery Stenosis: Myocardial Perfusion Imaging with Gadomer-17 First-Pass MR Imaging in a Swine Model of Comparison with Gadopentetate Dimeglumine. *Radiology*. 2007;225(1):104-112.

87. Schuster A, Sinclair M, Zarinabad N, et al. A quantitative high resolution voxel-wise assessment of myocardial blood flow from contrast-enhanced first-pass magnetic resonance perfusion imaging: microsphere validation in a magnetic resonance compatible free beating explanted pig heart model. *Eur Heart J Cardiovasc Imaging*. 2015;16(10):1082-1092.

88. Elzinga WE. Ameroid constrictor: uniform closure rates and a calibration procedure. *J Appl Physiol*. 1969;27(3):419-421.

89. Inou T, Tomoike T, Watanabe K, et al. A newly developed X-ray transparent ameroid constrictor for study on progression of gradual coronary stenosis. *Basic Res Cardiol*. 1980;75(4):537-543.

90. Guo M, Liu J, Guo F, et al. Panax Quinquefolium Saponins Attenuate Myocardial Dysfunction Induced by Chronic Ischemia. *Cell Physiol Biochem*. 2018;49(4):1277-1288.

91. Biran R, Pond D. Heparin coatings for improving blood compatibility of medical devices. *Adv Drug Deliv Rev*. 2017;112:12-23.

92. Mangiacapra F, Bressi E, Sticchi A, Morisco C, Barbato E. Fractional flow reserve (FFR) as a guide to treat coronary artery disease. *Expert Rev Cardiovasc Ther*. 2018;16(7):465-

477.

93. Hecht HS, Narula J, Fearon WF. Fractional Flow Reserve and Coronary Computed Tomographic Angiography: A Review and Critical Analysis. *Circ Res*. 2016;119(2):300-316.

94. Pontone G, Guaricci AI, Palmer SC, et al. Diagnostic performance of non-invasive imaging for stable coronary artery disease: A meta-analysis. *Int J Cardiol*. 2020;300:276-281.

95. Chesebro JH, Knatterud G, Roberts R, et al. Thrombolysis in myocardial infarction (TIMI) trial, phase I: A comparison between intravenous tissue plasminogen activator and intravenous streptokinase. Clinical findings through hospital discharge. *Circulation*. 1987;76(1):142-154.

96. Van Houten M, Yang Y, Hauser A, et al. Adenosine stress CMR perfusion imaging of the temporal evolution of perfusion defects in a porcine model of progressive obstructive coronary artery occlusion. *NMR Biomed*. 2019;32(11).

97. Kellman P, Xue H, Chow K, Spottiswoode BS, Arai AE, Thompson RB. Optimized saturation recovery protocols for T1-mapping in the heart: influence of sampling strategies on precision. *J Cardiovasc Magn Reson*. 2014;16(1):1-15.

98. Klein S, Staring M, Murphy K, Viergever MA, Pluim JPW. Elastix: A toolbox for intensity-based medical image registration. *IEEE Trans Med Imaging*. 2010;29(1):196-205.

99. Cerqueira MD, Weissman NJ, Dilsizian V, et al. Standardized myocardial segmentation and nomenclature for tomographic imaging of the heart: A Statement for Healthcare Professionals from the Cardiac Imaging Committee of the Council on Clinical Cardiology

of the American Heart Association. *Circulation*. 2002;105(4):539-542.

100. Pellikka PA, Nagueh SF, Elhendy AA, Kuehl CA, Sawada SG. American Society of Echocardiography Recommendations for Performance, Interpretation, and Application of Stress Echocardiography. *J Am Soc Echocardiogr*. 2007;20(9):1021-1041.

101. Rueckert D, Sonoda LI, Hayes C, Hill DLG, Leach MO, Hawkes DJ. Nonrigid registration using free-form deformations: application to breast MR images. *IEEE Trans Med Imaging*. 1999;18(8):712-721.

102. Klein S, Pluim JPW, Staring M, Viergever MA. Adaptive stochastic gradient descent optimisation for image registration. *Int J Comput Vis*. 2009;81(3):227-239.

103. Kavale KA, Glass G V. Meta-analysis and the integration of research in special education. *J Learn Disabil*. 1981;14(9):531-538.

104. Ugander M, Oki AJ, Hsu LY, et al. Extracellular volume imaging by magnetic resonance imaging provides insights into overt and sub-clinical myocardial pathology. *Eur Heart J*. 2012;33(10):1268-1278.

105. Kuijpers D, Prakken NH, Vliegenthart R, van Dijkman PRM, van der Harst P, Oudkerk M. Caffeine intake inverts the effect of adenosine on myocardial perfusion during stress as measured by T1 mapping. *Int J Cardiovasc Imaging*. 2016;32(10):1545-1553.

106. Liu A, Wijesurendra RS, Francis JM, et al. Adenosine Stress and Rest T1 Mapping Can Differentiate between Ischemic, Infarcted, Remote, and Normal Myocardium Without the Need for Gadolinium Contrast Agents. *JACC Cardiovasc Imaging*. 2016;9(1):27-36.

107. Bohnen S, Prüßner L, Vettorazzi E, et al. Stress T1-mapping cardiovascular magnetic resonance imaging and inducible myocardial ischemia. *Clin Res Cardiol*. 2019;108(8):909-920.

108. Poli FE, Gulsin GS, March DS, et al. The reliability and feasibility of non-contrast adenosine stress cardiovascular magnetic resonance T1 mapping in patients on haemodialysis. *J Cardiovasc Magn Reson*. 2020;22(1):1-13.

109. Messroghli DR, Greiser A, Fröhlich M, Dietz R, Schulz-Menger J. Optimization and validation of a fully-integrated pulse sequence for modified look-locker inversion-recovery (MOLLI) T1 mapping of the heart. *J Magn Reson Imaging*. 2007;26(4):1081-1086.

110. Niendorf T, Seeliger E, Cantow K, Flemming B, Waiczies S, Pohlmann A. Probing renal blood volume with magnetic resonance imaging. *Acta Physiol*. 2019;(December 2019):1-14.

111. Wacker CM, Wiesmann F, Bock M, et al. Determination of regional blood volume and intra-extracapillary water exchange in human myocardium using Feruglose: First clinical results in patients with coronary artery disease. *Magn Reson Med*. 2002;47(5):1013-1016.

112. McCommis KS, Goldstein TA, Zhang H, Misselwitz B, Gropler RJ, Zheng J. Quantification of myocardial blood volume during dipyridamole and doubtamine stress: a perfusion CMR study. *J Cardiovasc Magn Reson*. 2007;9(5):785-792.

113. Baudelet C, Gallez B. Effect of anesthesia on the signal intensity in tumors using BOLD-MRI: Comparison with flow measurements by Laser Doppler flowmetry and oxygen measurements by luminescence-based probes. *Magn Reson Imaging*. 2004;22(7):905-912.

114. Toth GB, Varallyay CG, Horvath A, et al. Current and potential imaging applications of ferumoxytol for magnetic resonance imaging. *Kidney Int*. 2017;92(1):47-66.

115. Vasanawala SS, Nguyen KL, Hope MD, et al. Safety and technique of ferumoxytol administration for MRI. *Magn Reson Med*. 2016;75(5):2107-2111.

116. Cerqueira MD, Weissman NJ, Dilsizian V, et al. Standardized myocardial segmentation and nomenclature for tomographic imaging of the heart. *J Cardiovasc Magn Reson*. 2002;4(2):203-210.

117. Lee JM, Choi KH, Park J, et al. Physiological and Clinical Assessment of Resting Physiological Indexes: Resting Full-Cycle Ratio, Diastolic Pressure Ratio, and Instantaneous Wave-Free Ratio. *Circulation*. 2019;139(7):889-900.

118. Achenbach S, Rudolph T, Rieber J, et al. Performing and interpreting fractional flow reserve measurements in clinical practice: An expert consensus document. *Interv Cardiol Rev*. 2017;12(2):97-109.

119. Dauber IM, VanBenthuysen KM, McMurtry IF, et al. Functional coronary microvascular injury evident as increased permeability due to brief ischemia and reperfusion. *Circ Res*. 1990;66(4):986-998.

120. Conover WJ. *Practical Nonparametric Statistics*. 3rd ed. John Wiley & Sons; 1999.

121. Modi BN, Rahman H, Kaier T, et al. Revisiting the optimal fractional flow reserve and instantaneous wave-free ratio thresholds for predicting the physiological significance of coronary artery disease. *Circ Cardiovasc Interv*. 2018;11(12).

122. Emrich T, Halfmann M, Schoepf UJ, Kreitner KF. CMR for myocardial characterization in ischemic heart disease: state-of-the-art and future developments. *Eur Radiol Exp*. 2021;5(1).

123. Guo BJ, Yang ZL, Zhang LJ. Gadolinium Deposition in Brain: Current Scientific Evidence and Future Perspectives. *Front Mol Neurosci*. 2018;11:335.

124. Montalescot G, Sechtem U, Achenbach S, et al. 2013 ESC guidelines on the management of stable coronary artery disease. *Eur Heart J*. 2013;34(38):2949-3003.

125. Ledda M, Fioretti D, Lolli MG, et al. Biocompatibility assessment of sub-5 nm silica-coated superparamagnetic iron oxide nanoparticles in human stem cells and in mice for potential application in nanomedicine. *Nanoscale*. 2020;12(3):1759-1778.

126. Finn JP, Nguyen KL, Han F, et al. Cardiovascular MRI with ferumoxytol. *Clin Radiol*. 2016;71(8):796-806.

127. Mcfadden C, Mallett CL, Foster PJ. Labeling of multiple cell lines using a new iron oxide agent for cell tracking by MRI. *Contrast Media Mol Imaging*. 2011;6(6):514-522.

128. Krishna. Estimation of tumor microvessel density by MRI using a blood pool contrast agent. *Int J Oncol*. 2009;35(4).

129. Sharma S, Mantini D, Vanduffel W, Nelissen K. Functional specialization of macaque premotor F5 subfields with respect to hand and mouth movements: A comparison of task and resting-state fMRI. *Neuroimage*. 2019;191:441-456.

130. Wang F, Jiang RT, Tantawy MN, et al. Repeatability and sensitivity of high resolution blood volume mapping in mouse kidney disease. *J Magn Reson Imaging*. 2014;39(4):866-871.

131. Rofsky NM, Lee VS, Laub G, et al. Abdominal MR imaging with a volumetric interpolated breath-hold examination. *Radiology*. 1999;212(3):876-884.

132. Semelka RC, Kelekis NL, Thomasson D, Brown MA, Laub GA. HASTE MR imaging: Description of technique and preliminary results in the abdomen. *J Magn Reson Imaging*. 1996;6(4):698-699.

133. Wildt A, Ahtola O. *Analysis of Covariance*. SAGE Publications, Inc.; 1978.

134. Khandhar AP, Wilson GJ, Kaul MG, Salamon J, Jung C, Krishnan KM. Evaluating size-dependent relaxivity of PEGylated-USPIOs to develop gadolinium-free T1 contrast agents

for vascular imaging. *J Biomed Mater Res Part A*. 2018;106(9):2440-2447.

135. Sourbron S. Technical aspects of MR perfusion. *Eur J Radiol*. 2010;76(3):304-313.

136. Rivera-Rivera LA, Schubert T, Knobloch G, et al. Comparison of ferumoxytol-based cerebral blood volume estimates using quantitative R1 and R2* relaxometry. *Magn Reson Med*. 2018;79(6):3072-3081.

137. Nguyen KL, Yoshida T, Han F, et al. MRI with ferumoxytol: A single center experience of safety across the age spectrum. *J Magn Reson Imaging*. 2017;45(3):804-812.

138. Bradley WG. Flow phenomena in MR imaging. *Am J Roentgenol*. 1988;150(5):983-994.

139. FDA Drug Safety Communication: FDA strengthens warnings and changes prescribing instructions to decrease the risk of serious allergic reactions with anemia drug Feraheme (ferumoxytol) | FDA.https://www.fda.gov/drugs/drug-safety-and-availability/fda-drug-safety-communication-fda-strengthens-warnings-and-changes-prescribing-instructions-decrease.